The role of CH25H in adipose tissue – a new potential target in anti-obesity therapy?

Doctoral thesis

to obtain a doctorate

from the Faculty of Medicine

of the University of Bonn

Inna Schleis

from Lahnstein

2024

Written with authorization of

the Faculty of Medicine of the University of Bonn

First reviewer: Prof. Dr. med. Alexander Pfeifer

Second reviewer: Prof. Dr. med. Philipp Sasse

Day of oral examination: 14.06.2024

From the Clinic of Pharmacology and Toxicology

Director: Prof. Dr. med. Alexander Pfeifer

Table of contents

List of Abbreviations

°C	degree Celsius
7α,25-OHC	7α,25-dihydroxycholesterol
AC	adenylate cyclase
ANCOVA	analysis of covariance
ANOVA	analysis of variance
APS	ammonium persulfate
AT	adipose tissue
ATM	adipose tissue macrophages
ATP	adenosine triphosphate
AUC	Area under the curve
BA	brown adipocytes
BAT	brown adipose tissue
bp	base pairs
BMDM	bone marrow-derived macrophages
BSA	bovine serum albumin
CAC	citric acid cycle
cAMP	cyclic adenosine monophosphate
cDNA	complementary deoxyribonucleic acid
cf	confer
CH25H	cholesterol-25-hydroxylase
CO_2	carbon dioxide
Ct	cycle threshold
CYP7B1	Cytochrome P450 family 7 subtype b member 1
Da/kDa	Dalton/Kilodalton
DAB	3,3´-Diaminobenzidine
DEPC	diethyl pyrocarbonate
dH_2O	deionized water
DM	differentiation medium
DMEM	Dulbecco's Modified Eagle Medium
DMSO	dimethyl sulfoxide

DNA	deoxyribonucleic acid
EBI2	Epstein-Barr virus-induced G-protein coupled receptor 2
EDTA	ethylenediaminetetraacetic acid
EE	energy expenditure
e.g.	exempli gratia, for example
ELISA	enzyme-linked immunosorbent assay
EtOH	ethanol
FBS	fetal bovine serum
FFA	free fatty acids
GM	growth medium
GPCR	G-protein coupled receptor
GTT	glucose tolerance test
HE	hematoxylin eosin (staining)
HEPES	4-(2-hydroxyethyl)-1-piperazineethanesulfonic acid
HFD	high fat diet
HPLC-MS	high-performance liquid chromatography coupled with mass spectrometry
HPRT	Hypoxanthine Phosphoribosyltransferase
HSD3B7	3 beta-hydroxysteroid dehydrogenase type 7
HSL	hormone-sensitive lipase
IBMX	3-isobutyl-1-methylxanthine
IM	induction medium
i.e.	id est, that is to say
KO	knock out
l/ml/µl	liter/milliliter/mikroliter
LPS	lipopolysaccharide
M_0	unpolarised macrophages
MCSF	macrophage colony stimulating factor
MetS	metabolic syndrome
M_{LPS}	LPS stimulated macrophages
mRNA	messenger ribonucleic acid
MS	multiple sclerosis

ND	normal diet
NE	norepinephrine
NEAA	nonessential amino acids
NMR	nuclear magnetic resonance
NP-40	nonyl phenoxypolyethoxylethanol
NST	non-shivering thermogenesis
O_2	oxygen
OHC	hydroxycholesterol/dihydroxycholesterol
PAGE	polyacrylamide gel electrophoresis
PCR	polymerase chain reaction
PKA	protein kinase A
PFA	paraformaldehyde
PBS	Phosphate-buffered saline
pH	pondus hydrogenii
PPARγ	peroxisome proliferator-activated receptor γ
P/S	Penicillin/Streptomycin
rcf	relative centrifugal force
RER	respiratory exchange ratio
RIPA	radio immunoprecipitation assay
RNA	ribonucleic acid
ROS	reactive oxygen species
rpm	rounds per minute
RT	room temperature
RT-qPCR	real time quantitative polymerase chain reaction
SDS	sodium dodecyl sulfate
s.e.m.	standard error of the mean
SVF	stromal vascular fraction
T2DM	type 2 diabetes mellitus
T3	triiodothyronine
TAE	Tris-acetate-EDTA
TBS	Tris-buffered saline
TBST	Tris-buffered saline with Tween 20

TEMED	tetramethylethylenediamine
TG	triglycerides
UCP1	Uncoupling protein 1
UV	ultraviolet
V/mV	Volt/millivolt
WA	white adipocytes
WAT	white adipose tissue
WATg	gonadal white adipose tissue
WATi	inguinal white adipose tissue
WT	wild type

1. Introduction

1.1 Adipose tissue

Unlike the general notion that the sole function of adipose tissue (AT) is the storage of excess energy, it is already known for a long time that there is a colour-coded variety of white, brown and beige AT with diverse functions (Pfeifer et al., 2015) (Fig. 1).

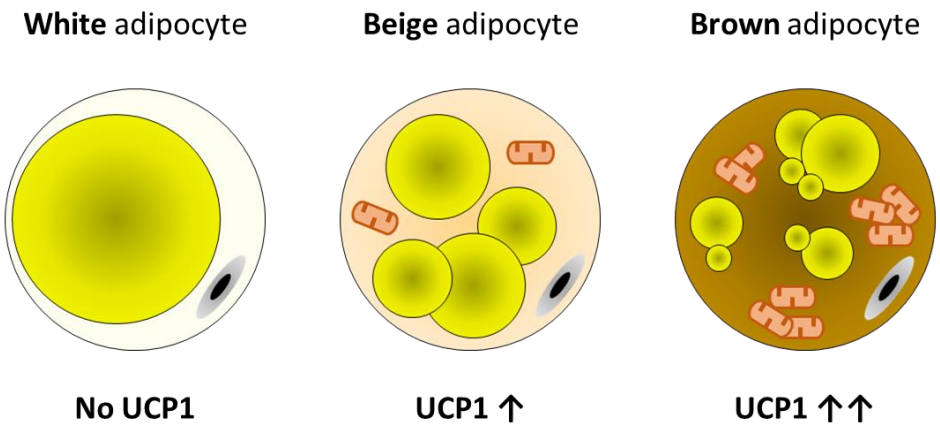

Fig. 1: Different types of adipocytes and adipose tissues. From left to right: white, beige and brown adipocytes with varying amounts of mitochondria, lipid droplets and Uncoupling protein 1 (UCP1) determining the capacity to dissipate energy in form of heat.

1.1.1 White adipose tissue

White adipose tissue (WAT) plays a major role in metabolic homeostasis. Firstly, it has a high capacity to store excess energy in form of triglycerides (TG) in the cytoplasm of adipocytes. White adipocytes (WA) are histologically characterised by a central unilocular lipid droplet (Cinti, 2012). Secondly, WAT is crucial for buffering fatty acid flux in the postprandial period (Frayn, 2002). Therefore, a high flexibility in alternating between the processes of lipid uptake and free fatty acid (FFA) release is mandatory. Biochemically, these opposing metabolic pathways are termed lipogenesis and lipolysis (Saponaro et al., 2015).

In general, WAT can be divided into different depots regarding their location. In rodents, the most important WAT depot consists of gonadal WAT (WATg) which corresponds to visceral fat depots in humans. The second large murine fat depot comprises inguinal WAT (WATi) which corresponds to the gluteofemoral subcutaneous fat depots in humans

(Chusyd et al., 2016). Anatomically, WAT consists of a variety of different cell types ranging from progenitor cells, endothelial cells, pericytes, macrophages and lymphocytes to adipocytes (Han et al., 2015).

In need of energy, for example during fasting or physical exercise, the organism can mobilise its energy stores via hydrolysis of TG into FFA and glycerol. Many factors have been described to modulate lipolysis, such as natriuretic peptides, glucocorticoids and Tumor necrosis factor α (Nielsen et al., 2014). However, the main physiological activator of lipolysis is norepinephrine (NE) released by the sympathetic nervous system (Zeng et al., 2015). WAT is directly innervated by sympathetic nerve endings which release NE (Bartness et al., 1998) and therefore activate β-adrenergic receptors (β_1-β_3). Although all three β-adrenergic receptors are expressed in human WA, lipolysis is mainly mediated via β_1- and β_2-receptors (Barbe et al., 1996; Tavernier et al., 1996). All β-adrenergic receptors belong to the group of G_s-coupled G-protein coupled receptors (GPCR) and NE binding activates an intracellular signalling cascade beginning with the activation of the adenylate cyclase (AC). The AC induces increased intracellular levels of cyclic adenosine monophosphate (cAMP) by conversion of adenosine triphosphate (ATP) to cAMP. Subsequently, cAMP activates protein kinase A (PKA) which in turn directly phosphorylates and activates hormone-sensitive lipase (HSL), and indirectly activates adipose triglyceride lipase by phosphorylation of perilipin. These two enzymes, together with the lipolytic activity of monoglyceride lipase, lead to the hydrolysis of TG in FFA and glycerol after being translocated to the lipid droplet. Finally, FFA are released into blood circulation (Duncan et al., 2007; Nielsen et al., 2014).

Recent research has been particularly concerned with the endocrine function of WAT. Starting with the discovery of leptin, whose main function is the regulation of energy homeostasis by inhibiting further food intake after eating (Saladin et al., 1995; Zhang et al., 1994), more so called adipokines were discovered including adiponectin and resistin (Steppan et al., 2001). Moreover, other classical cytokines as Tumor necrosis factor α and interleukin 6 secreted by WA were identified to play a crucial role in the regulation of energy homeostasis, immunity and insulin sensitivity. Altered adipokine secretion is now known to play an important role in the pathophysiology of obesity (Ahima, 2006; Ronti et al., 2006).

1.1.2 Brown adipose tissue

For a long time, human brown adipose tissue (BAT) has only been considered to be important for new-borns. In a process termed non-shivering thermogenesis (NST), infants can prevent hypothermia by generating heat (Aherne et al., 1966; Dawkins et al., 1965). In adulthood, BAT mass and activity diminish, leading to the conception that BAT was entirely absent in adult humans. It was only 15 years ago that independent studies rediscovered the existence and activity of BAT in healthy adults (Cypess et al., 2009; Nedergaard et al., 2007; van Marken Lichtenbelt et al., 2009; Virtanen et al., 2009). The anatomical location of BAT shifts from the predominantly interscapular distribution in newborns (Aherne et al., 1966) to the rather cervical-supraclavicular and paravertebral distribution in adolescents and adults (Drubach et al., 2011). Histologically, BAT is characterised by multilocular fat droplets and a high number of mitochondria (Cinti, 2012).

The main activator for NST is cold, which leads to the stimulation of sympathetic nerve endings and the ensuing release of NE (Cypess et al., 2012). A tight regulation of BAT activity is guaranteed by a five to six-fold higher sympathetic innervation and vascularisation of BAT in comparison to WAT (Néchad, 1986). Whereas lipolysis is mainly mediated by β_3-adrenergic receptors in rodent BAT, it is less clear in human BAT. β_2-adrenergic receptors are more abundant in human BAT compared to β_3-adrenergic receptors (Taverner et al., 1996) and stimulation of β_2-adrenergic receptors with e.g. salbutamol significantly increases energy expenditure (EE) (Blondin et al., 2020; Straat et al., 2023). On the other hand, activation of β_3-adrenergic receptors with the selective agonist mirabegron also increases EE, but only in supratherapeutical doses (Cero et al., 2021; Cypess et al., 2015).

The molecular mechanism underlying the capacity of BAT to dissipate energy in form of heat is the mitochondrial Uncoupling Protein 1 (UCP1) (Nicholls et al., 1984). UCP1 is a FFA activated proton translocator in the inner mitochondrial membrane. Fedorenko et al. (2012) achieved to unravel the precise transport mechanism by which long chain fatty acids and a proton are symported across the membrane. Due to strong hydrophobic interactions, long chain fatty acids are permanently associated with UCP1, so that, effectively, UCP1 acts as a proton translocator. As a result, UCP1 is capable of short-circuiting the proton gradient generated by the complexes of the respiratory chain (Fedorenko et

al., 2012). Therefore, the proton efflux is uncoupled from proton-dependent ATP-synthesis resulting in the lack of negative feedback of ATP on key enzymes in the mitochondrial citric acid cycle (CAC). Consequently, fatty acid oxidation and oxidation in CAC continue and lead to the direct generation of heat (Fig. 2). Lately, also succinate was shown to increase thermogenesis in BAT in a UCP1-dependent manner (Mills et al., 2018).

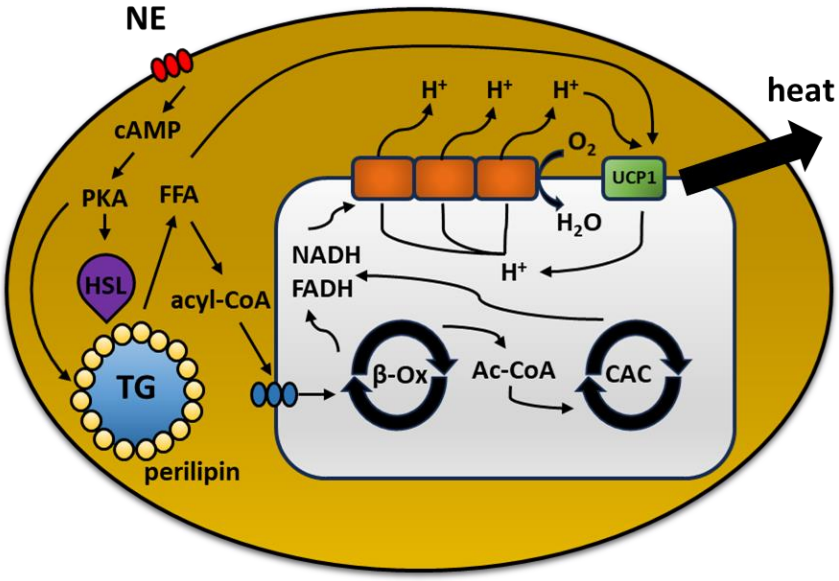

Fig. 2: NE induced thermogenesis in BAT. Norepinephrine (NE)-stimulated β_3-receptors induce cyclic adenosine monophosphate (cAMP) mediated lipolysis of triglycerides (TG) into free fatty acids (FFA). FFA can either be degraded in mitochondrial β-oxidation (β-Ox) and citric acid cycle (CAC) or can bind to Uncoupling protein 1 (UCP1). UCP1 uncouples proton dependent ATP-synthesis and dissipates energy in form of heat. FADH = flavin adenine dinucleotide, HSL = hormon-sensitive lipase, NADH = nicotinamide adenine dinucleotide, PKA = protein kinase A.

Furthermore, UCP1-independent ways of BAT-activation were recently described, e.g., a cycle of re-esterification of FFA and glycerol (Schweizer et al., 2018), the regulation of intracellular Calcium-level via *Serca2b* (Ukropec et al., 2006) and proton leak by the mitochondrial ADP/ATP-carrier (Bertholet et al., 2019). A Creatine-dependent way of activating thermogenesis was specifically described to occur in beige fat (Kazak et al, 2015). Moreover, UCP1 can be regulated on the transcriptional level: *Ucp1* gene expression can be induced by cAMP and peroxisome proliferator-activated receptor gamma (PPARγ) resulting in higher thermogenic capacities (Chen et al., 2013).

1.1.3 Beige or brite adipocytes

The terms beige or brite (brown-in-white) adipocytes were coined due to the observation that these adipocytes share functional and phylogenetical similarities with both white and brown adipocytes (BA) (Pfeifer et al., 2015). Morphologically and functionally beige adipocytes resemble classical BA as they also contain multilocular lipid droplets and a high number of mitochondria expressing UCP1 (Lo et al., 2013). Although UCP1 expression in beige adipocytes amounts only to 10 % of UCP1 expression in BA (Nedergaard et al., 2013), thermogenesis of beige adipocytes still exerts an anti-obesity and antidiabetic effect (Wu J et al., 2013). Beige adipocytes mainly reside in subcutaneous WAT depots (Sidossis et al., 2015).

Currently, two different theories of beige adipocyte biogenesis are being discussed in the scientific community. The transdifferentiation theory hypothesises that certain WA undergo a transdifferentiation to beige adipocytes upon e.g. chronic cold exposure, endocrine stimuli, β-adrenergic stimulation, application of PPARγ agonists and adenosine, a process also called “browning” (Barbatelli et al., 2010; Lo et al., 2013). This is why beige adipocyte depots are often described as inducible or recruitable BAT (Pfeifer et al., 2015). Another theory proposes a *de novo* beige adipocyte differentiation from resident progenitor cells (McDonald et al., 2015; Wang et al., 2014). It is hypothesised, that the mode of beige adipocyte recruitment depends on the previous history of cold exposure (Shao et al., 2019).

Similar to BA, beige adipocytes can also undergo a whitening process which depicts a transdifferentiation of BA to adipocytes with rather WA characteristics. This process is based on a remodelling of chromatin state after exposure to warmth, but the adipocytes remain an epigenetic memory of previous cold exposure (Roh et al., 2018). Consequently, beige adipocytes can rather be understood as bidirectional adipocytes capable of switching between a phenotype of energy storage similar to WA and energy dissipation similar to BA (Wu et al., 2012).

1.1.4 Adipose tissue in obesity

Obesity is caused by an imbalance of calorie intake and calorie expenditure leading to the accumulation of fat and a pathological increase in body weight. Worldwide, obesity prevalence has nearly tripled between 1975 and 2016. According to the World Health Organization's definition of overweight (Body mass index ≥ 25) and obesity (Body mass index ≥ 30), 1.9 billion adults were overweight or obese in 2016 (WHO datasheet 2020). Especially the increasing prevalence of obesity amongst children with a portion of 20 % - 30 % obese children in 2016 is an emerging health issue as 70 % of obese children are predicted to become obese adults (Dehghan et al., 2005; NCD Risk Group Collaboration, 2017). Therefore, obesity can be regarded as a global pandemic which urgently requires more educational work and prevention alongside research on molecular and pharmacological targets.

Obesity is a burden for both the socioeconomic system and the individual as obesity associates with diverse comorbidities such as hypertension, cardiovascular disease, certain types of cancer, metabolic syndrome (MetS) and especially type 2 diabetes mellitus (T2DM) (Pfeifer et al., 2015). One reason why obesity leads to diverse comorbidities can be seen in the dysfunction of AT in storing excess energy. The exhaustion of storage capacity in AT contributes to the ectopic accumulation of lipids in liver, muscles and other organs resulting in impaired cell function (Hardy et al., 2012; Virtue et al., 2010). This effect termed lipotoxicity manifests itself in terms of insulin resistance, mitochondrial dysfunction, chronic inflammation and apoptosis (Engin, 2017).

Currently, more attention is drawn to the role of the immune system in this process. Macrophages were found to infiltrate expanding AT resulting in inflammatory responses and the development of insulin resistance (Weisberg et al., 2003; Xu et al., 2003). Many mechanisms leading to macrophage invasion are now known, such as adipocyte death, chemotactic regulation, altered fatty acid fluxes, hypoxia and hypoxia-induced fibrosis (Sun et al., 2011). Chronic inflammation is fuelled by the transformation of macrophages from an anti-inflammatory phenotype of alternatively activated macrophages to a rather proinflammatory phenotype of classically activated macrophages (Lumeng et al., 2007). Subsequently, other immune cells such as T lymphocytes and mast cells invade inflamed and

obese AT (Nishimura et al., 2009) leading to a vicious circle of inflammation and cell dysfunction. Systemic effects are mediated via altered cytokine and adipokine secretion by various cell types in obese AT which therefore promotes the development of so called immunometabolic disorders (Hotamisligil, 2006). In the concept of immunometabolism as an interface of immunity and metabolism, cytokines can be even regarded as metabolic hormones (Hotamisligil, 2017). In conclusion, targeting the immune system depicts a new promising approach in the therapy of obesity (Winer et al., 2009).

1.2 Oxysterols

1.2.1 General characteristics of oxysterols

Oxysterols are oxygenated derivatives of cholesterol and its precursors (Schroepfer, 2000). Indeed, oxysterols are formed by modifying cholesterol structure with hydroxylations, ketone groups, epoxides or carboxyl groups on the steroid backbone, on the sidechain or both (Mutemberezi et al., 2016b).

One major pathway of oxysterol synthesis is the enzymatic hepatic biotransformation of cholesterol and its precursors (Schroepfer, 2000). The liver plays an important role in the homeostasis of cholesterol metabolism as it eliminates excess cholesterol by transforming it into more polar compounds such as bile acids. Therefore, a whole machinery of biotransformation enzymes are needed, including oxidoreductases, enzymes of the cytochrome P450 family, hydrolases and transferases. Moreover, these enzymes work in a redundant manner: the same modification can be carried out by multiple enzymes on an oxysterol, and a single enzyme can use various oxysterols as substrate (Mutemberezi et al., 2016b). Additionally, enzyme-independent modifications were described by cholesterol autoxidation involving reactive oxygen species (ROS), such as free radicals, or reactive nitrogen species (Bergstrom et al., 1941; Iuliano, 2011).

In the past years, it became obvious that oxysterols are not mere intermediates in bile acid synthesis but also exert more pleiotropic functions. For example, oxysterols were shown to regulate cholesterol synthesis (Kandutsch et al., 1973) and were detected as intermediates in steroid hormone production including pregnenolone and vitamin D3 (Luu-The, 2013). Accordingly, oxysterols were found to be involved in bone mass homeostasis

and the pathogenesis of osteoporosis (Nelson et al., 2013). In addition, certain oxysterols can activate hedgehog signalling, a signalling pathway important in developmental patterning (Myers et al., 2013). Consequently, it is no surprise that oxysterols are also linked to the development of certain types of cancer, e.g. hedgehog-related medulloblastoma, basal cell carcinoma (Briscoe et al., 2013) and estrogen-related breast cancer (Wu Q et al., 2013). On top, oxysterols are related to nervous system development and homeostasis in terms of promoting neurogenesis and myelination (Theofilopoulos et al., 2013; Meffre et al., 2015).

Importantly, some oxysterols are described to play a role in immune regulation, anti-viral responses, cytokine secretion and the development of autoimmunity. Certain oxysterols, such as 7α,25-dihydroxycholesterol (7α,25-OHC), 7α,27-OHC and 7β,27-OHC are key mediators in the differentiation and chemotaxis of immune cells, especially of T and B cells (Hannedouche et al., 2011; Liu et al., 2011; Soroosh et al., 2014). Oxysterols contribute to the development and promotion of various autoimmunity conditions including multiple sclerosis (MS), inflammatory bowel disease, rheumatoid arthritis and type 1 diabetes mellitus (Duc et al., 2019). On a molecular level, oxysterols can mediate their effects via different receptors and target proteins (Tab. 1).

Tab. 1: Oxysterol receptors and target proteins with their mediated effects. Based on Mutemberezi et al. (2016b) and references therein.

type of receptor	receptor	effect
nuclear receptors	liver X receptors (LXR)	modulation of transcriptional activity depending on agonism or (partial/inverse) antagonism of the ligand and the functional constitution (homo-/heterodimer) of the receptor
	RAR-related orphan receptors (ROR)	
	estrogen receptors (ER)	
G protein coupled receptors (GPCR)	EBI2	chemotaxis of immune cells and especially B cells, humoral response, autoimmunity
	CXCR2	
	smoothened receptor (SMO)	Hedgehog signalling, development, oncogenesis
ion channels	NMDA	allosteric modulation of calcium signalling
transport proteins	insulin induced gene protein (INSIG)	modulation of cholesterol synthesis, vesicle trafficking, lipid metabolism and signal transduction
	oxysterol binding protein (OSBP)	

Currently, the two commonly used methods for measuring oxysterol levels in tissue and serum are gas chromatography-mass spectrometry (Dzeletovic et al., 1995) and liquid chromatography tandem-mass spectrometry (McDonald et al., 2012). Both methods involve chromatographic separation of oxysterols which is challenging due to a high diversity of isomeric oxysterols. Additionally, careful and rapid sample collection is mandatory to avoid adulterated results because of short half-lives and *ex vivo* oxidation of cholesterol (Griffiths et al., 2019).

Overall, research on oxysterols has attracted attention and consideration in the last decades. Despite the complexity due to complex synthesis mechanisms, various molecular targets, diverse biological effects and challenging methods in measuring oxysterol levels, oxysterol research currently draws great interest in unravelling the signalling mechanisms as well as their possible role in an outstanding variety of diseases.

1.2.2 The oxysterol 7α,25-OHC, the enzyme CH25H and the receptor EBI2

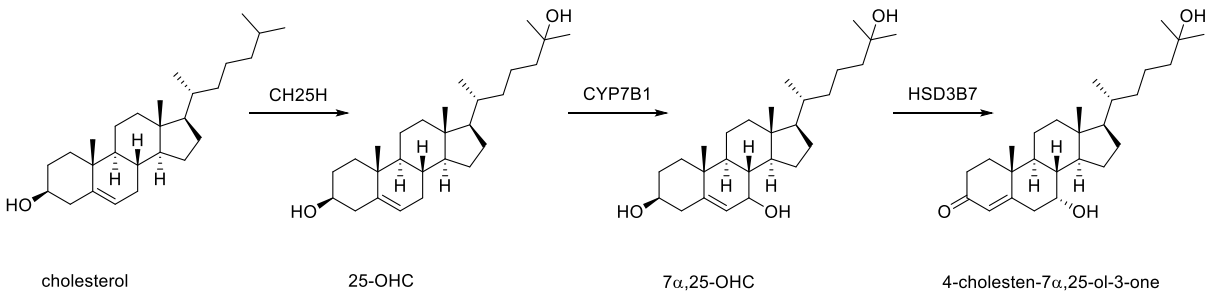

Fig. 3: Main biosynthesis pathway of 7α,25-OHC. Cholesterol is enzymatically hydroxylated on position 7 and 25. 7α,25-OHC is inactivated by HSD3B7. 25-OHC = 25-hydroxycholesterol, 7α,25-OHC = 7α,25-dihydroxycholesterol, CH25H = cholesterol-25-hydroxylase, CYP7B1 = Cytochrome P450 family 7 subtype b member 1, HSD3B7 = 3 beta-hydroxysteroid dehydrogenase type 7.

7α,25-OHC is a dihydroxylated oxysterol directly synthesised from cholesterol in two enzymatic steps. The main synthesis pathway involves cholesterol-25-hydroxylase (CH25H) and Cytochrome P450 family 7 subtype b member 1 (CYP7B1) (Russell, 2000) (Fig. 3). Alternatively, 7α,25-OHC can be produced by the enzymes CYP7A1, CYP3A and

CYP27A1 which perform 7- and 25-hydroxylation subordinated to their main catalytic function (Honda et al., 2011; Lund et al., 1993). However, 7α,25-OHC formation can also take place to a lesser extent by autoxidation involving ROS or reactive nitrogen species (Iuliano, 2011). 3 beta-hydroxysteroid dehydrogenase type 7 (HSD3B7) is responsible for the degradation of 7α,25-OHC (Yi et al., 2012).

In 2011, two independent studies identified 7α,25-OHC to be the most potent activator of Epstein-Barr virus-induced G-protein coupled receptor 2 (EBI2 also known as GPR183) (Hannedouche et al., 2011; Liu et al., 2011). Interestingly, its enantiomer 7β,25-OHC was proven to be a less potent activator of EBI2 (Hannedouche et al., 2011). Originally, EBI2 was found to be significantly upregulated in Burkitt's lymphoma cells upon Epstein-Barr virus infection (Birkenbach et al., 1993). Receptor activity studies revealed that EBI2 most likely acts via $G\alpha_i$ protein (Rosenkilde et al., 2006) but further $G\alpha_i$-independent signalling pathways could be detected for EBI2 (Fig. 4). EBI2 was identified to play a crucial role in the positioning of B cells in secondary lymphoid organs and the promotion of antibody production during immune responses (Gatto et al., 2009; Pereira et al., 2009). Besides, EBI2 was reported to be involved in the development of autoimmune diseases such as type 1 diabetes mellitus and MS as well as in cancer cell proliferation (Sun et al., 2015).

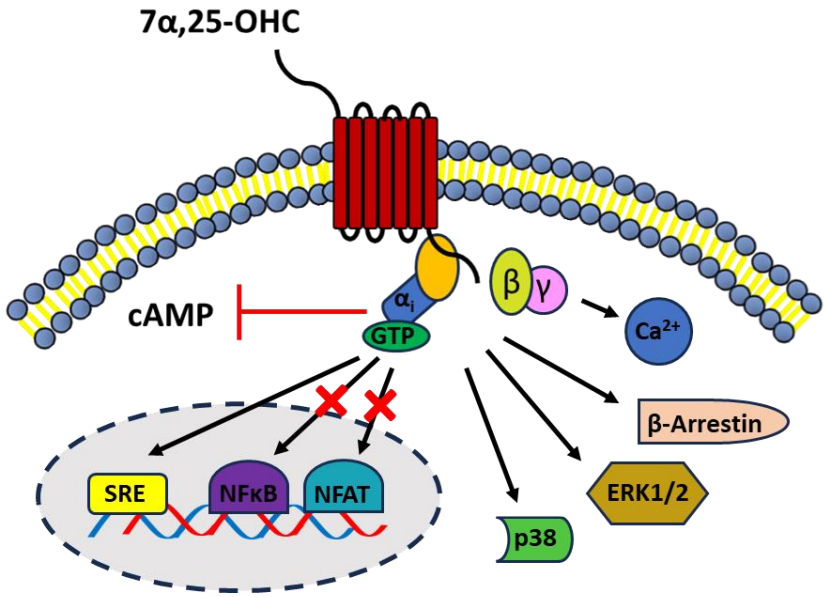

Fig. 4: EBI2 signalling pathways. Whereas the $G\alpha_i$-subunit of the EBI2 receptor decreases intracellular cAMP levels, the Gβγ-subunit activates Ca^{2+} signalling. In a G-protein independent manner, EBI2 signalling activates SRE (sterol-regulatory element), β-Arrestin, p38 and ERK signalling. 7α,25-OHC = 7α,25-dihydroxycholesterol, cAMP = cyclic adenosine monophosphate, GTP = guanosine triphosphate.

Unlike most enzymes involved in oxysterol synthesis, CH25H, the first enzyme involved in the production of 7α,25-OHC from cholesterol, does not belong to the family of cytochrome P450 enzymes. Instead, CH25H uses diiron cofactors for hydroxylation (Griffiths et al., 2018). CH25H expression is high in macrophages and even increases upon lipopolysaccharide (LPS) stimulation indicating that CH25H plays an important role in innate immune regulation (Preuss et al., 2014). Indeed, *Ch25h* was demonstrated to be a type I interferon regulated gene leading to increased levels of 25-OHC which acts as a potent paracrine molecule in antiviral responses (Blanc et al., 2013). However, there is still controversial data on the question whether CH25H and its product 25-OHC act in a rather proinflammatory or anti-inflammatory manner. Several studies showed diverging expression profiles of inflammatory markers upon 25-OHC administration (Gold et al., 2014; Morello et al., 2009; Reboldi et al., 2014; Zhao et al., 2020). Currently, more studies are conducted on this topic.

Most likely, several studies already indicated that CH25H, 25-OHC and the EBI2-signalling pathway are involved in the pathogenesis of inflammatory diseases such as chronic rhinosinusitis (Hulse et al., 2013), rheumatoid arthritis (Dulos et al., 2004), osteoarthritis (Choi et al., 2019), MS (Duc et al., 2019) and inflammatory bowel disease (Raselli et al., 2019).

Hannedouche et al. (2011) could demonstrate that mice lacking the gene *Ch25h* showed almost non-detectable levels of 7α,25-OHC and failed to attract B cells equally as *Ebi2* deficient mice. Therefore, the *Ch25h* knock out (KO) model will be used to further investigate the role of 7α,25-OHC in AT.

1.2.3 Oxysterols in adipose tissue and obesity

Previous studies showed that adipocytes express important proteins and enzymes for cholesterol transport, metabolism and oxysterol synthesis (Li et al., 2014). CYP27A1 was identified as a crucial enzyme in the *de novo* synthesis of oxysterols in adipocytes. Furthermore, its product 27-OHC was shown to influence white adipocyte differentiation in a paracrine or autocrine manner (Li et al., 2014). Thus, together with growing attention to AT as an endocrine organ, it is of great interest to investigate whether other oxysterols can be produced by adipocytes themselves.

Furthermore, several ensuing studies investigated the effect of obesity on oxysterol levels in liver, plasma and AT in mice (Wooten et al., 2014; Guillemot-Legris et al., 2016a). Those studies provided a first insight in the complexity of oxysterol metabolism in obesity as they showed that a magnitude of oxysterols was increased in liver, plasma, brain and AT in obese mice. However, a correlation between altered oxysterol levels and correspondingly altered expression of the synthesising enzyme could not be established indicating that nonenzymatic autoxidation might also play an important role in obesity.

1.3 Aims of the project

CH25H and 7α,25-OHC were described to play a major role in the regulation and function of our immune system rendering those molecules important players in the development of autoimmune and immunometabolic diseases like obesity. Interestingly, we were able to show in preliminary experiments (data unpublished) that 7α,25-OHC is present in AT and exerts an inhibitory function in the regulation of lipolysis. Therefore, we hypothesised a role of 7α,25-OHC in the development or promotion of obesity. Thus, to investigate the role and production of 7α,25-OHC in AT my thesis project has been divided in four major parts addressing the following issues:

1) Expression analysis of enzymes involved in 7α,25-OHC metabolism: Expression was analysed on messenger ribonucleic acid (mRNA) and protein level using quantitative polymerase chain reaction (PCR) and Western Blot in different tissues and tissue fractions from lean and obese mice.

2) Investigation of cell interaction in AT: To study the mutual influence of adipocytes and other cell types, I used a transwell system to perform co-cultivation studies with bone marrow-derived macrophages (BMDM), endothelial cells and fibroblasts.

3) Investigation of oxysterol levels in *Ch25h* WT and KO mice: Thanks to our collaborators in Belgium (Prof. G. G. Muccioli, Louvain University) we could measure oxysterol levels in different tissues of *Ch25h* wild type (WT) and KO mice using high-performance liquid chromatography coupled with mass spectrometry (HPLC-MS) method.

4) Metabolic characterisation of *Ch25h* KO mice *in vivo*: In the first part, *Ch25h* WT and KO mice housed at 23 °C were metabolically characterised by indirect calorimetry (measurement of O_2 consumption, CO_2 production and motility), analysis of body composition and *Ucp1* expression. Additionally, *ex vivo* lipolysis of BAT and WAT explants from *Ch25h* WT and KO mice was conducted. Metabolic characterisation was also performed on *Ch25h* WT and KO mice housed at 4 °C to investigate the browning process in WAT. Finally, metabolic characterisation and *Ucp1* expression analysis was performed on *Ch25h* WT and KO mice fed with either normal (ND) or high fat diet (HFD) for 12 weeks to study the effects of diet induced obesity.

2. Material and Methods

2.1 Common chemicals and equipment

If not stated otherwise, all common chemicals for media, buffers and solutions were purchased from Carl Roth GmbH (Karlsruhe), Merck (Darmstadt) and Sigma-Aldrich (München).

Common equipment

- Autoclave, Varioklav 135 T (Faust)
- β-mercaptoethanol (Sigma-Aldrich, Cat. No. M6250)
- Bovine Serum Albumin (BSA) (Sigma-Aldrich, Cat. No. A7030)
- Canulaes (Braun, Sterican 0,90 x 40 mm, Cat. No. 4657519)
- Canulaes (Braun, Sterican, 0,40 x 20 mm, Cat. No. 4657705)
- Centrifuge, Biofuge Primo (Heraeus) in cell culture
- Centrifuge 5430R (Eppendorf) for protein and RNA methods
- Conical tubes, 15 ml and 50 ml (Sarstedt, Cat. No. 62.554.502, 62.547.254)
- Collagenase, Type II (Worthington, Cat. No. CLS2)
- Countess Automated Cell Counter (Invitrogen, Cat. No. C10227)
- Countess cell counting chamber slides (Invitrogen, Cat. No. C10283)
- Cryogenic vials (Sarstedt, Cat. No. 72.379.992)
- Fetal Bovine Serum (FBS) (Biochrom, Cat. No. S0115)
- HFD food (ssniff Spezialdiäten, EF D12492 (II) mod., Cat. No. E15741-34)
- Homogenizer, T10 basic Ultra-Turrax (IKA)
- Incubator, HERAcell® 150 (Heraeus)
- Isofluran-Piramal (Piramal Group, Cat. No. 9714675)
- Laminar air flow, HerasafeTM (Heraeus)
- Liquid nitrogen (Linde)
- Microscope EVOS XL (Thermo Scientific) for histology
- Microscope, LEICA DM IL (Leica Microsystems GmbH) for cell culture
- Mili-Q Water Purification System (Merck EMD Milipore)
- Minispin centrifuge (Sigma-Aldrich, Cat. No. Z606235)

- ND food (ssniff Spezialdiäten, EF D12450B mod. LS, Cat. No. E15748-04)
- Penicillin/streptomycin (P/S) (Merck, Cat. No. A2212)
- pH meter HI2210 (Hanna Instruments)
- Pipetboy acu 2 (Integra)
- Reaction tube 0.5 ml, 1.5 ml, 2 ml (Sarstedt, Cat. No. 72.699, 72.706, 72.695500)
- Scales (Sartorius Extend ED124S)
- scissors, forceps (Fine science tools)
- Screw cap bottle (Kautex 1000 ml, Cat. No. 303-1000)
- Serological pipettes 5 ml, 10 ml, 25 ml (Sarstedt, Cat. No. 86.1253.001, 86.1254.001, 86.1685.001)
- Thermocycler Biometra TOne (Analytik Jena)
- Thermomixer comfort (Eppendorf, Cat. No. 2050-120-04)
- Trypan Blue Stain (Gibco, Cat. No. 15250)
- Trypsin-Ethylenediaminetetraacetic acid (EDTA) (0.05 %), phenol red (Trypsin; Gibco, Cat. No. 25300054)

2.2 Animals and animal models

An initial breeding pair of *Ch25h* $^{+/-}$ mice with C57BL/6 background was kindly provided by Caroline Pot, Department of Clinical Neurosciences, Lausanne University Hospital, Switzerland. WT mice with C57BL/6j background needed for further experiments were purchased from Jackson Laboratories.

All mice were kept and bred at Haus für experimentelle Therapie, Universitätsklinikum Bonn, or at Institut für Pharmakologie und Toxikologie, Universitätsklinikum Bonn, during experiments. All mice were housed at 23 °C ± 1 °C and had *ad libitum* access to food and water.

All experiments were approved by Landesamt für Natur, Umwelt und Verbraucherschutz, Nordrhein-Westfalen, Germany (Aktenzeichen 84-02.04.2017.A311).

2.2.1 Genotyping of *Ch25h* WT and KO mice

Material and equipment

- Agarose Standard (Roth, Cat. No. 9012-36-6)
- Casting platforms (EmbiTech)
- Electrophoresis chamber (Peqlab)
- Ethidium bromide 10 mg/ml (Roth, Cat. No. 2218.1)
- GelDoc XR (BioRad)
- Microwave (Panasonic)
- Phire Tissue Direct PCR Mix (Thermo Scientific, Cat. No. F-170)
- QuantityOne Software (BioRad)

Buffers and solutions

Tris-acetate-EDTA (TAE) buffer 50x

Acetic acid	5.71 %
Na_2-EDTA	50 mM
Tris-HCl	2 M

All compounds were dissolved in water.

Phire Tissue Direct PCR Mix was used to investigate the genotype of *Ch25h* WT and KO littermates. Therefore, ear biopsies were taken at the age of 3 weeks and incubated at room temperature (RT) for 5 minutes in a solution of 20 µl Dilution Buffer and 0.5 µl of deoxyribonucleic acid (DNA) Release Additive. Samples were mixed by vortexing and centrifuged before they were incubated in a prewarmed heating block at 98 °C for 2 minutes. A reaction mix was prepared in the following composition:

10 µl	2X Phire Tissue Direct PCR Master Mix
1 µl	each primer in 0.5 µM concentration (Tab. 2)
1 µl	sample
6 µl	water

PCR was performed in a Biometra Tone thermocycler (Tab. 3).

Tab. 2: List of primers used for genotyping PCR. Final concentration 0.5 µM.

Primer	Sequence (5' – 3')
CH25H common	CAC AGT CTT AAG AAA AGT CGG CGG GG
CH25H WT	GTA GGC AGA AGC CCA CGT AAG TGA TG
CH25H KO	GCA TCA GAG CAG CCG ATT GTC TGT TG

Tab. 3: Amplification program for genotyping PCR.

Step	Temperature	Time	Repetitions
1	98 °C	30 s	
2	98 °C	5 s	
3	65 °C	5 s	- 0.5 °C/cycle
4	72 °C	10 s	to step 2 for 10 times
5	98 °C	5 s	
6	60 °C	5 s	
7	72 °C	10 s	to step 5 for 28 times
8	72 °C	1 min	
9	4 °C	∞	

PCR products were visualized in a 2.5 % agarose gel which was prepared by dissolving agarose in TAE buffer under constant heating in a microwave. 800 ng/ml Ethidium bromide was added and the gel solution was poured into cassettes. After the gel solidified at RT, 12 µl of PCR product were loaded onto the gel and electrophoresis started in an electrophoresis chamber filled with TAE buffer at 120 V for approximately 30-40 minutes. Subsequently, PCR products were detected under 366 nm ultraviolet (UV) light using a UV transilluminator (GelDoc XR) and QuantityOne Software. WT genotypes were detected at the size of 200 base pairs (bp), KO genotypes were expected at 400 bp.

2.3 Cell culture methods

Material and equipment

- 4-(2-Hydroxyethyl) piperazine-1-ethanesulfonic acid (HEPES) (Sigma Aldrich, Cat. No. PHG0001)
- 8-Brom-cAMP (Biolog, Cat. No. B007-100)
- 30 µm and 100 µm nylon meshes (Millipore, Cat. No. NY3002500, NY1H00010)
- 10 cm^2 TC dishes, Standard (Sarstedt, Cat. No. 83.3902)

- 6-well and 12-well TC plates (Sarstedt, Cat. No. 83.3920, 83.3921)
- 3, 3′, 5-Triiodo-L-thyronine sodium salt (T3) (Sigma-Aldrich, Cat. No. T6397)
- 3-Isobutyl-1-methylxanthine (IBMX) (Sigma-Aldrich, Cat. No. I5879)
- Dexamethasone (Sigma-Aldrich, Cat. No. D4902)
- Dulbecco's Modified Eagle's Medium (DMEM), high glucose, GlutaMAX Supplement, pyruvate (Gibco, Cat. No. 31966)
- Dulbecco's Modified Eagles's Medium (DMEM), high glucose, GlutaMAX supplement (Gibco, Cat. No. 61965)
- Dulbecco's Modified Eagles's Medium (DMEM) Nutrient Mixture F-12 (Gibco, Cat. No. 11320033)
- Insulin solution human (Sigma-Aldrich, Cat. No, I9278)
- Lipopolysaccharide (LPS) (Thermo Fisher Scientific, Cat. No. 00-4976-93)
- Macrophage Colony Stimulation Factor (MCSF) (PeproTech, Cat. No. 315-02)
- Non-essential amino acids solution (NEAA) (Gibco, Cat. No. 11140050)
- Retinoic acid (Sigma-Aldrich, Cat. No. R2625)
- Syringe filter 0.45 µm (VWR, Cat. No. 514-0063)
- Syringes 5 ml (BD Discardit II, Cat. No. 309050)
- T175 tissue culture flasks (Sarstedt, Cat. No. 83.3912.002)

2.3.1 Cell culture of brown adipocytes

Buffers and media

Phosphate-buffered saline (PBS)

NaCl	137 mM
KCl	2.7 mM
Na_2HPO_4 * 12 H_2O	8 mM
KH_2PO_4	1.4 mM

All compounds were dissolved in water, the pH was adjusted to 7.4 and the solution was autoclaved.

BA isolation buffer

NaCl	123 mM
KCl	5 mM
CaCl2	1.3 mM
HEPES	100 mM

All compounds were dissolved in sterile water and the pH was adjusted to 7.4. The solution was sterile filtered with a 0.45 µm nylon filter and stored at 4 °C.

BSA fatty acid free	2 %
Collagenase II	2 mg/ml

BSA and Collagenase II were added shortly before use, properly dissolved and sterile filtered with a 0.45 µm nylon filter.

BA culture medium

DMEM, high glucose, GlutaMAX supplement (Gibco, Cat. No. 61965) supplemented with

FBS	10 %
P/S	1 %
HEPES	10 mM
Insulin	4 nM
T3	4 nM
Sodium-Ascorbate	25 µg/ml

BA growth medium (GM)

DMEM, high glucose, GlutaMAX (Gibco, Cat. No. 61965) supplemented with

FBS	10 %
P/S	1 %

BA differentiation medium (DM)

BA GM supplemented with

Insulin	20 nM
T3	1 nM

BA induction medium (IM)

BA DM supplemented with

IBMX	0.5 mM
Dexamethasone	1 µM

IM was prepared freshly every time. IBMX was dissolved in dimethyl sulfoxide (DMSO) and warmed up in the water bath to avoid precipitation.

2.3.1.1 Primary murine brown adipocytes isolation

Newborn WT C57BL/6 mice were sacrificed by decapitation. The interscapular brown fat depot was taken and transferred to a reaction tube with 0.5 ml of BA isolation buffer. Tissue was minced into small pieces and transferred to a 15 ml conical tube containing 2.5 ml of BA isolation buffer. The suspension was digested at 37 °C in the water bath for 30 minutes with powerful shaking every 5 minutes. Larger pieces were extracted by filtering the suspension through a 100 µm nylon mesh. After 30 minutes on ice, the middle phase was collected and filtered again through a 30 µm nylon mesh. Subsequently, suspensions were centrifuged at 700 relative centrifugal force (rcf) for 10 minutes. The pellet was resuspended in 2 ml of BA culture medium and seeded in a 6-well-plate.

One day after BA isolation, cells were immortalised with 200 ng of rrl156-PGK-Tag virus (Simian Virus 40 large T-antigen under the control of phosphoglycerate kinase PGK promotor) diluted in 800 µl of BA GM. On the next day, wells were filled up to 3 ml with BA GM and cells were consecutively grown till 90 % confluency with medium change every second day.

Then, cells were washed with PBS twice and 1 ml of prewarmed 0.05 % Trypsin-EDTA was added. After 5 minutes of incubation at 37 °C, the reaction was stopped by adding BA GM. The cell suspension was collected and distributed equally in two 10 cm^2 plates which were filled up to 10 ml with BA GM. Cells were passage 1 then.

This procedure was repeated three times with a splitting ratio of 1:10 till cells were passage 4. In every splitting step a certain part of cells was frozen in cryogenic vials.

Therefore, cells were washed twice with PBS and detached with 1 ml of 0.05 % Trypsin-EDTA. After 5 minutes of incubation at 37 °C the reaction was stopped by adding BA GM. Cells were counted with Trypan Blue Stain in the Countess Automated Cell Counter and pelleted at 1000 rounds per minute (rpm) for 10 minutes. Supernatant was discarded and

the pellet resuspended in a suitable volume of BA GM with 10 % DMSO for a final concentration of 1 million cells/ml. Cell suspension was immediately distributed in cryogenic vials which were stored at -80 °C.

2.3.1.2 Brown adipocyte differentiation

All cells used for *in vitro* experiments were passage 4. Cells in cryogenic vials were shortly prewarmed in a 37 °C water bath. Cell suspension was diluted in BA GM and seeded in a density of 80.000 cells (12 well plate) or 160.000 cells (6 well plate) per well. Cells were always kept in the incubator at 37 °C with 5 % CO_2.

Medium was changed every second day according to the following scheme (Fig. 5):

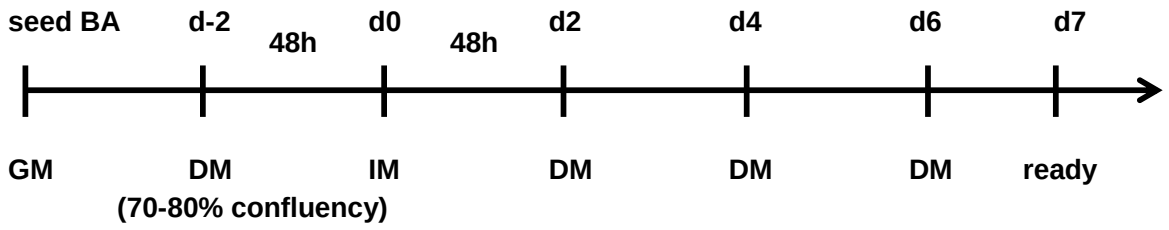

Fig. 5: BA cultivation scheme for *in vitro* experiments. Cells were seeded in BA growth medium (GM). When cells reached 70-80 % confluency (usually after two days) medium was changed to BA differentiation medium (DM). Cells were induced on d0 with induction medium (IM), henceforth only DM was used. On d7, cells could be used for lipolysis assay, protein or RNA isolation.

2.3.2 Cell culture of bone marrow-derived macrophages

Media

<u>BMDM GM</u>

DMEM Nutrient Mixture F-12 (Gibco, Cat. No. 11320033) supplemented with

FBS	5 %
P/S	1 %

2.3.2.1 BMDM isolation

BMDM were isolated from 8 weeks old WT C57BL/6 mice. Leg bones (i.e. femur and tibia) were freed from fur and muscles and cut open on both sides. With the help of a needle and a syringe filled with BMDM GM, the hollow inner part of the bone was washed and BMDM collected in a conical tube. Cells were pelleted in the centrifuge at 1000 rpm for 5 minutes and resuspended in BMDM GM containing 10 % DMSO. Cell suspension was distributed in cryogenic vials (one vial per mouse) and stored at -80 °C.

2.3.2.2 Differentiation and polarisation of BMDM

Cells were prewarmed in a 37 °C water bath and resuspended in 32 ml BMDM GM supplemented with 1 µl/ml MCSF. 8 ml of cell suspension was distributed in each of four 10 cm^2 dishes. Cells were always kept in the incubator at 37 °C with 5 % CO_2.

After 3-4 days, 3 ml of BMDM GM with 1 µl/ml MCSF was added.

On day 6 cells were ready to be polarised:

- M_0 macrophages: M_0 macrophages remained unpolarised. The old medium was simply replaced by new BMDM GM without MCSF.
- M_{LPS} macrophages (LPS stimulated macrophages): The old medium was replaced by 10 ml of new BMDM GM supplemented with 10 µl of LPS.

Cells were polarised overnight and used for experiments the next day.

2.3.3 Cell culture of NIH-3T3 fibroblasts

NIH-3T3 is a murine fibroblast cell line which was originally established by George Todaro and Howard Green (Todaro et al., 1963). NIH-3T3 cells were used at passages 21-24 for all experiments.

BA GM was used for seeding and passaging NIH-3T3 fibroblasts. Cells in cryogenic vials were prewarmed in a 37 °C water bath and diluted in 15 ml of BA GM. After centrifugation at 500 rcf for 10 minutes medium was discarded and the pellet resuspended in 10 ml of BA GM. Cells were seeded in a 10 cm^2 plate and incubated at 37 °C and 5 % CO_2.

Cells were grown to 80-90 % confluency and then split in a ratio of 1:5-10 depending on confluency. Therefore, cells were washed twice with PBS. For detachment, cells were

incubated with 1 ml of 0.05 % Trypsin-EDTA for 3-5 minutes in an incubator at 37 °C. Reaction was stopped by adding 10 ml of BA GM. Cell suspension was centrifuged at 1000 rpm for 5 minutes, medium was discarded and pellet was resuspended in 10 ml of BA GM. Cells were equally distributed in new 10 cm^2 plates which were filled up to 10 ml with BA GM.

Freezing of NIH-3T3 cells followed the same protocol as for BA in 2.3.1.1.

2.3.4 Cell culture of T17b cells

T17b is a murine embryonal endothelial progenitor cell line which was initially characterised by Antonis Hatzopoulos (Hatzopoulos et al., 1998). T17b cell line was kindly provided by Christian Kupatt (LMU Munich, Germany).

Media and solutions

T17b basal medium

DMEM, high glucose, GlutaMAX (Gibco, Cat. No. 61965) supplemented with

FBS	20 %
P/S	1 %
NEAA	1 %
HEPES	0,5 mM
β-mercaptoethanol	1 µM

T17b DM

T17b basal medium supplemented with

8-Brom-cAMP	100 mM
Retinoic acid	1 mM (in DMSO)

T17b cells were used at passages 4-5 for all experiments. As T17b cells do not recover their full proliferation potential after seeding, freshly thawed cells were passaged before using them in experiments. To achieve that, cells were prewarmed in a 37 °C water bath and seeded in a cell culture flask coated with 0.1 % gelatine in T17b basal medium. Cells were incubated at 37 °C and 5 % CO_2.

Cells were passaged at 70-80 % confluency as T17b cells tend to dedifferentiate when reaching high confluency. T17b splitting followed the same protocol as for NIH-3T3 cells in 2.3.3. Cells were seeded in 12-well plate wells (for control) or directly in transwell inserts (for the experiment) without gelatine coat in T17b basal medium.
During the next three days, T17b cells were successively differentiated with T17b DM. Medium was changed daily. After differentiation, T17b cells almost stop proliferating and can be cultured for further 2-3 days. At this point, co-cultivation experiments with BA were performed.

2.4 Co-cultivation experiments

Material and equipment

- 12-well and 24-well TC plates (Sarstedt, Cat. No. 83.3921, 83.3922)
- TC-Inserts, 12-well (Sarstedt, Cat. No. 83.3931.041)

The aim of co-cultivation experiments is to study the mutual influence of two different cell lines on each other. To examine that, plastic inserts were used to allow the exchange of soluble factors (Fig. 6).

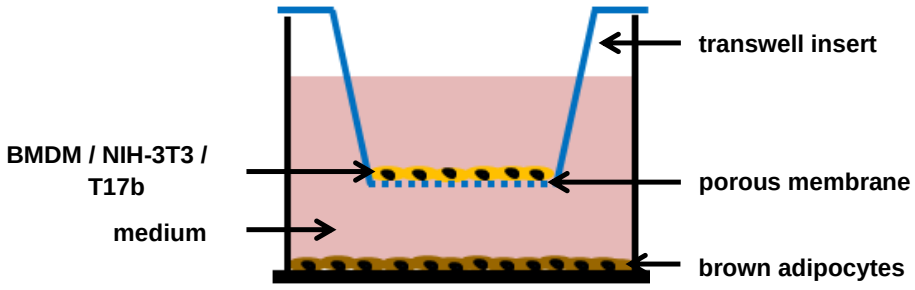

Fig. 6: Experimental setup for co-cultivation studies of brown adipocytes using a transwell insert system. The transwell inserts have a semipermeable porous membrane which enables the exchange of soluble factors either produced by brown adipocytes or the cells in the transwell. BA were seeded at the bottom of a 12-well plate well. The medium consists of a 50:50 mixture of BA DM and the growth or basal medium of the cocultured cell line.

BA were co-cultivated with BMDM, NIH-3T3 and T17b cells for 72 h. To do that, BA were seeded in a 12-well plate and cultured as described in 2.3.1.2 till d4.

On d4 of BA differentiation, transwell inserts with BMDM, NIH-3T3 or T17b cells were added. The cell lines were grown and cultured as described in the following:

- BMDM were seeded one day after the corresponding BA have been seeded. Consequently, BMDM were polarised on d3 of BA differentiation to M_0 and M_{LPS} overnight and used for the transwell the next day. BMDM were detached with 0.05 % Trypsin-EDTA following the standard protocol as described for NIH-3T3 cells.
- NIH-3T3 cells were passaged and cultured as described in 2.3.3. On d3 of BA differentiation, a NIH-3T3 culture plate with 80-90 % confluency was splitted and cells were directly seeded in transwell inserts. Remaining cells were seeded in 12-well plates as control. Cells were incubated overnight at 37 °C and 5 % CO_2. Inserts were put on BA the next day.
- T17b cells were passaged and cultured as described in 2.3.4. On d-1 of BA differentiation, T17b cells were splitted and directly seeded in transwell inserts. Remaining cells were seeded in 24-well plates as control. From the next day on, T17b cells were differentiated in the inserts for the following three days. On d3 of BA differentiation, T17b DM was changed to basal medium again. Inserts were put on BA the next day.

Cells were always counted in the Countess Automated Cell Counter using Trypan Blue Stain and were seeded in a density of 400.000 cells per transwell insert.

The medium used in the co-cultivation experiments was a 50:50 mixture of BA DM and the growth or basal medium of the cocultured cell line. The bottom of the system contained 1 ml of medium, the insert 0.5 ml of medium.

After 72 h of co-cultivation in an incubator at 37 °C and 5 % CO_2, inserts were discarded and BA were used for either lipolysis assay, real-time quantitative polymerase chain reaction (RT-qPCR) or Western Blot.

2.5 Lipolysis assay

Material and equipment

- 96-well TC plates (Sarstedt, Cat. No. 83.3924)
- Dulbecco's Modified Eagle's Medium (DMEM), high glucose, HEPES, no phenol red (Gibco, Cat. No. 21063)
- Free glycerol reagent (Sigma-Aldrich, Cat. No. F6428)
- Forskolin (Sigma-Aldrich, Cat. No. F6886)
- Glycerol standard (Sigma-Aldrich, Cat. No. G7793)
- Norepinephrine (Sigma-Aldrich, Cat. No. A9512)

2.5.1 *In vitro* lipolysis

BA were washed 3 times with lipolysis medium (DMEM Gibco, Cat. No. 21063, supplemented with 2 % BSA). Afterwards, 400 µl of lipolysis medium were added and cells were incubated for 2 h at 37 °C and 5 % CO_2.

To measure the free glycerol release of the cells, 40 µl of the plate lipolysis medium supernatant were mixed with 60 µl of Free glycerol reagent in a 96-well plate well. As a positive control, 5 µl of Glycerol standard were mixed with 95 µl of Free glycerol reagent whereas the blank was pipetted with 40 µl of lipolysis medium and 60 µl of Free glycerol reagent. Each sample was prepared in duplicates and incubated at 37 °C for 5 minutes. Absorption was measured at 540 nm and 600 nm as a reference wavelength using Enspire Microplate Reader.

Afterwards, BA were washed with PBS twice. Protein was isolated following the standard protocol in 2.8.1 and protein concentration was measured using Bradford method (2.8.2). Absorbance values were normalised to protein concentration.

2.5.2 *Ex vivo* lipolysis

8 weeks old male *Ch25h* WT and KO mice were sacrificed. Three pieces of each 4-5 mg BAT and 25-30 mg WATi/WATg were prepared and the exact weight recorded. The pieces of tissue were kept in PBS on ice and were finally cut in three smaller pieces. Afterwards, the pieces were incubated in 400 µl of lipolysis medium (DMEM Gibco, Cat. No. 21063,

supplemented with 2 % BSA) ± substances (blank, 1 µM NE and 10 µM forskolin) in a 24-well plate for 2 h at 37 °C and 5 % CO_2.
The subsequent procedure was the same as for *in vitro* lipolysis assay (2.5.1). Absorbance values were normalised to tissue weight in mg.

2.6 Fractionation of adipose tissue in SVF and floating adipocytes

Material and equipment

- Dulbecco's Modified Eagle's Medium (DMEM), high glucose, GlutaMAX Supplement, pyruvate (Gibco, Cat. No. 31966)
- Syringe filter 0.45 µm (VWR, Cat. No. 514-0063)

Buffers and media

WA isolation buffer

DMEM, high glucose, GlutaMAX, pyruvate (Gibco, Cat. No. 31966) supplemented with

Collagenase II	1.5 mg/ml
BSA fatty acid free	0.5 %

Isolation buffer was prepared freshly in PBS and sterile filtered through a 0.45 µm filter.

WA GM

DMEM, high glucose, GlutaMAX, pyruvate (Gibco, Cat. No. 31966) supplemented with

FBS	10 %
P/S	1 %

Isolation buffer was prepared freshly and sterile filtered through a 0.45 µm filter.

10 WT C57BL/6 mice each were set on HFD and ND for 12 weeks. All three fat depots (BAT, WATi, WATg) were taken, washed with PBS and kept on ice. 2 ND and HFD mice were each pooled resulting in 5 samples for ND and HFD each. Tissues were minced with scissors and transferred to a conical tube containing 7 ml of WA isolation buffer. Samples were incubated at 37 °C in the water bath for 30-45 minutes with powerful shaking every

5 minutes. Digestion was stopped by adding 7 ml of WA GM. After 10 minutes of incubation at RT, samples were centrifuged at 153 rcf for 10 minutes. Floating adipocytes were collected with a pipette tip and transferred to a 1.5 ml reaction tube which was immediately frozen in liquid nitrogen.
Supernatant was discarded and the pellet was resuspended in 1 ml of PBS. After centrifugation at 100 rcf for 10 minutes, the resulting pellet contained the stromal vascular fraction (SVF). SVF comprises all non-adipocyte cells as endothelial cells, immune cells, fibroblasts and preadipocytes (Han et al., 2015). Supernatant was discarded and samples frozen in liquid nitrogen. Currently, there are multiple protocols available for the fractionation of adipose tissue, which differ in the amount and force of centrifugation steps. They all have in common, that the centrifugation steps serve the receipt of a higher amount of SVF.

2.7 RNA methods

Material and equipment

- Diethyl pyrocarbonate, DEPC (Roth, Cat. No. K028.1)
- InnuSOLV RNA Reagent (Analytik Jena AG, Cat. No. 845-SB-2090100)
- Nanodrop2000 Spectrophotometer (ThermoScientific)
- ProtoScript II First Strand cDNA Synthesis Kit (NEB, Cat. No. E6560S)
- Real-time PCR machine, 7900HT (Applied Biosystems)
- SYBR-Green PCR master mix (Applied Biosystems, Cat. No. 4309155)
- Speed Vac Concentrator plus (Eppendorf, Cat. No. 5305)

2.7.1 RNA isolation

To isolate ribonucleic acid (RNA), cells, tissue or tissue fraction samples were mixed with 1 ml of innuSOLV RNA Reagent. If necessary, samples were homogenized with the help of T10 basic Ultra-Turrax Homogenizer. 200 µl of cold chloroform were added and samples were shaken powerfully for 15 seconds. After keeping the samples on ice for 5 minutes, samples were centrifuged at 13.000 rpm and 4 °C for 10 minutes. The clear

upper layer containing the RNA was collected and transferred to a 1.5 ml reaction tube. 500 µl of cold isopropanol were added and tubes were powerfully shaken for 15 seconds. Again, samples were centrifuged at 13.000 rpm and 4 °C for 10 minutes resulting in RNA being pelleted. Supernatant was discarded and RNA pellet was washed using 75 % ethanol (EtOH) followed by centrifugation at 13.000 rpm and 4 °C for 5 minutes. This washing step was performed 4 times. Samples were dried in the SpeedVac Concentrator Plus at 45 °C for 30 minutes. Dry pellets were solved in 20 µl of DEPC-water for 10 minutes at 55 °C.

RNA concentration and purity was assessed with Nanodrop2000 Spectrophotometer. RNA was stored at -80 °C.

2.7.2 cDNA synthesis

Complementary DNA (cDNA) synthesis was performed with the ProtoScript II First Strand cDNA Synthesis Kit from New England BioLabs. For each sample 1000 ng of RNA were used. Reaction buffer, enzymes and primers were added according to the manufacturer's instructions. cDNA was synthesised in Thermocycler Biometra TOne using the following reaction steps: 25 °C for 5 min, 42 °C for 60 min and finally 80 °C for 5 min.

Afterwards, cDNA was diluted 1:20 to a concentration of 2.5 ng/µl.

2.7.4 RT-qPCR

4 µl of cDNA were mixed with 5 µl of SYBR Green Master Mix and 0.5 µl of each primer (Tab. 4) resulting in a total volume of 10 µl. Samples were amplified in duplicates using the following program in the 7900HT Real-time PCR machine (Tab. 5):

Tab. 4: Sequences of primers used for RT-qPCR.

Target	Forward (5' - 3')	Reverse (5' – 3')
CH25H	CAT AAG GAC AAG GGA GGC G	CAC GAA CGG TAG GCA GAA G
CYP7B1	CCT CTT TCC TCC ACT CAT ACA C	GTC CAA AAG GCA TAA CGT AAG TC
EBI2	CAG CTT TAC CCA CTC GGA TA	AAG AAG CGG TCT TGC TCA A
HSD3B7	CAT CCA CCA AGT CAA CGT GC	GGT ATC TTC ATT GCC CCT GTA G
HPRT	ACA TTG TGG CCC TCT GTG TGC TCA	CTG GCA ACA TCA ACA GGA CTC CTC GT
UCP1	GGT GAA CCC GAC AAC TTC CGA AGT G	GGG TCG TCC CTT TCC AAA GTG TTG A

Tab. 5: RT-qPCR amplification program. Steps 5-7 comprised the melting curve for evaluating primer pair quality.

Step	Temperature	Time	Repetitions
1	25 °C	30 s	
2	95 °C	600 s	
3	95 °C	15 s	
4	60 °C	60 s	to step 3 for 40 times
5	95 °C	15 s	
6	56 °C	15 s	
7	95 °C	15 s	

2.8 Protein methods

Material and equipment

- Acrylamide (Rotiphorese Gel 30, Roth, Cat. No. 3029.1)
- Aluminium foil (Roth, Cat. No. 2596.1)
- Ammonium persulfate (APS) (Roth, Cat. No. 9592.2)
- BioPhotometer D30 (Eppendorf)
- Complete protease inhibitor cocktail (Roche, Cat. No. 04693116001)
- Color Prestained Protein Standard, Broad Range (New England BioLabs, Cat. No. P7712S)
- Coomassie brilliant blue G250 (Merck, Cat. No. 1.15444.0025)
- Electrophoresis power supply Consort EV202 (Consort)
- Mini Protean Tetra Vertical Electrophoresis System (BioRad, Cat. No. 1658006FC)
- Nitrocellulose blotting membrane (GE Healthcare Life science, Cat. No. 10600002)
- Nonfat dried milk powder (Applichem Panreac, Cat. No. 271-045-3)
- Nonidet P40 substitute (NP-40) (Sigma-Aldrich, Cat. No. 74385)
- Odyssey Fc Imaging System (LI-COR)
- Rocking Platform (VWR, Cat. No. 444-0145)
- Rolling Platform RM5 (Ingenieurbüro CAT, Cat. No. 60207-00)
- Sodium dodecyl sulfate (SDS) (Roth, Cat. No. 4360)

- Syringe filter 0.2 µm (VWR, Cat. No. 514-0061)
- Tetramethylethylenediamine (TEMED) (Sigma-Aldrich, Cat. No. T7024)
- Trans-Blot Turbo Transfer System (BioRad, Cat. No. 1704150)
- Tween 20 (Roth, Cat. No. 9127.2)
- Whatman gel blotting paper GB003 (Sigma-Aldrich, Cat. No. WHA10426892)

Buffers and solutions

Radio Immunoprecipitation Assay (RIPA) buffer

NaCl	150 mM
Tris-Cl pH 7.5	50 mM
NP-40	1 %
Desoxycholic acid-Na	0.25 %
SDS	0.1 %

Compounds were dissolved in distilled water. Solution was sterile filtered through a 0.2 mm syringe filter.

RIPA+ buffer (protein lysis buffer)

RIPA buffer	
NaF	10 mM
Na_3VO_4	1 mM
Complete protease inhibitors	40 µl/ml

One pill of the Complete protease inhibitors was dissolved in 2.5 ml of water.

Coomassie brilliant blue G250 solution

Coomassie brilliant blue G250	0.01 %
EtOH 95 %	5 %
H_3PO_4 85 %	10 %

Compounds were dissolved in water. Solution was filtered through a folded filter and stored at 4 °C.

3x Lämmli loading buffer

Tris-Cl pH 6.8	18.75 mM
Glycerol	3 %
SDS	0.6 %
bromophenol blue	0.0015 %

Compounds were dissolved in water. Aliquots were stored at -20 °C and were complemented with 5 % of β-mercaptoethanol shortly before usage.

1.5 M 4xTris-Cl / SDS (for Resolving Gel)

Tris base	18.2 %
SDS	0.4 %

Compounds were dissolved in distilled water and pH was adjusted to 8.8 with 37 % HCl. Storage at 4 °C.

1 M 4x Tris-Cl / SDS (for Stacking Gel)

Tris base	12.08 %
SDS	0.4 %

Compounds were dissolved in distilled water and pH was adjusted to 6.8. Storage at 4 °C.

10x Electrophoresis buffer

Tris base	248 mM
Glycine	1.92 M
SDS	1 %

Compounds were dissolved in distilled water.

Towbin buffer (transfer buffer)

Tris base	25 mM
glycine	192 mM
methanol	20 %

Compounds were dissolved in distilled water and pH adjusted to 8.1 - 8.5.

10x TBS (Tris-buffered saline) and TBST

Tris base	100 mM
NaCl	1.4 M

Compounds were dissolved in distilled water and pH adjusted to 8. For TBST (Tris-buffered saline with Tween 20) TBS was supplemented with 0.1 % of Tween 20.

2.8.1 Protein isolation

For protein isolation from *in vitro* experiments, plates with cells were washed twice with PBS and put on ice immediately. Cold RIPA+ lysis buffer was added to a desired end volume of 100-200 µl. After 10 minutes of incubation on ice, cells were scraped from the plate and transferred to a reaction tube. Samples were centrifuged at 13.000 rpm for 10 minutes at a temperature of 4 °C resulting in a floating fat layer and a pellet containing cell debris. The middle clear phase with protein was taken and transferred to a new reaction tube. Storage at -20 °C.

For protein isolation from tissue, samples were homogenised in RIPA+ lysis buffer using T10 basic Ultra-Turrax Homogenizer. The amount of RIPA+ lysis buffer corresponded to the estimated sample volume.

2.8.2 Bradford assay and protein quantification

Protein concentration was assessed by performing Bradford protein assay, a photometric method using Coomassie Brilliant blue. 98 µl of 0.15 M NaCl were mixed with 2 µl of protein solution. 1 ml of Coomassie Brilliant blue solution was added and the samples were incubated for 2 minutes at RT. Absorbance was spectrophotometrically measured at 595 nm with BioPhotometer D30. Protein concentration was calculated with the help of a BSA standard calibration curve which was established beforehand.

2.8.3 SDS-PAGE and Western Blot

For SDS polyacrylamide gel electrophoresis (PAGE), protein samples with a protein amount of 30 µg were prepared. To do that, the corresponding volume was calculated according to the protein concentration and 3x Lämmli buffer was added in the appropriate volume. Protein samples were denatured at 95 °C for 10 minutes in the Thermocycler.

SDS-PAGE gels were prepared by resolving gel in the lower part und stacking gel in the upper part (Tab. 6). Samples and protein ladder were loaded on the gel and electrophoresis was started using Mini Protean Tetra Vertical Electrophoresis System. Electrophoresis was performed at 180 V and 300 mA for 50-70 minutes depending on how far the proteins were supposed to be separated.

Tab. 6: Composition of resolving and stacking gels for SDS-PAGE. 12 % gels were used for low molecular weight proteins (15-30 kDa, i.e. UCP1). 10 % gels were used for proteins of higher molecular weight (30-100 kDa, i.e. CH25H). pH of Tris-HCl for resolving gels was adjusted to 8.8, for stacking gels to 6.8.

	Resolving gel		**Stacking gel**
Compound	**10 %**	**12 %**	
H_2O	4 ml	3.3 ml	3.4 ml
Acrylamide	3.3 ml	4 ml	830 µl
Tris-HCl	2.5 ml	2.5 ml	630 µl
20 % APS	50 µl	50 µl	25 µl
TEMED	4 µl	4 µl	5 µl

Following the protein separation in the SDS-PAGE, proteins were transferred to a nitrocellulose membrane using the Trans-Blot Turbo Transfer System at 25 V for 30 minutes in semidry technique with Towbin buffer. After the transfer, the nitrocellulose membranes were cut into appropriate pieces according to the size of the target proteins. Membrane stripes were blocked in a 2.5 % milk powder-TBST solution for at least 1 h on a shaking platform. Subsequently, membranes were washed in TBST for 5 minutes and incubated with the corresponding primary antibody overnight at 4 °C on a rolling platform (Tab. 7). Primary antibodies were diluted 1:1000 in a 2.5 % milk powder – TBST solution supplemented with 0.5 % of NaN_3 10 %.

The next day, membranes were washed 3 x 5 minutes in TBST on a shaking platform. Secondary antibody was diluted 1:15.000 in TBST and incubated with the membranes on a shaking platform with aluminium foil as protection for fluorescent antibodies. After 1 h of incubation at RT membranes were washed again 3 x 5 minutes in TBST.

Finally, membranes were developed at 800 nm using Odyssey Fc Imaging System.

Tab. 7: List of primary and secondary antibodies for Western Blot.

	Target	Host species	Company	Cat. No.
primary	Calnexin, C-terminal (575-593)	rabbit	Sigma Aldrich	208880
	CH25H, clone 1G8	mouse	Sigma Aldrich	SAB1403010
	UCP1 (293-307)	rabbit	Thermo Fisher Scientific	PA9514
secondary	Anti-mouse-IgG, DyLight 800 4x PEG Conjugate	(goat)	Cell signalling	5257S
	Anti-rabbit-IgG, DyLight 800 4x PEG Conjugate	(goat)	Cell Signalling	5151S

2.9 Histology methods

Material and equipment

- Anti-UCP1 (293-307), Rabbit Ab (Thermo Fisher Scientific, Cat. No. PA9514)
- Coverslips, Menzel-Gläser 24 * 60mm (Thermo Scientific, Cat. No. 15747592)
- 3,3´-Diaminobenzidine (DAB) Peroxidase Substrate Kit (Vector Laboratories, Cat. No. SK-4100)
- Eosin (Sigma-Aldrich, Cat. No. HT110216)
- Heating magnetic stirrer, ARE (VELP scientifica)
- Leica EG1160 Embedding Center (Leica)
- Low-profile disposable blades 819 (Leica, Cat. No. 14035838925)
- Microscope Slides Menzel-Gläser Superfrost Plus (Thermo Scientific, Cat. No. J1800AMNT)
- Microtome Microme HM355E (Thermo Scientific)
- Normal Goat Serum (Cell signalling, Cat. No. 5425S)
- Paraffin Paraplast (Leica, Cat. No.39601006)
- Paraffin tissue floating bath Microm SB80 (Thermo Scientific)
- ParaFree Disposable Base Mold (Leica, Cat. No. 39-LC-705-2)
- Pap Pen Liquid Blocker (Science Services, Cat. No. N71310)
- Roti Histokitt (Roth, Cat. No. 6638.2)

- SignalStain Boost IHC Detection Reagent, HRP/Rabbit (Cell Signalling, Cat, No. 8114S)
- Staining cuvettes and slides tray
- Tissue cassettes (Histosette, Simport, Cat. No. M490)
- Transferpipette 3.5 ml (Sarstedt, Cat. No. 86.1171)
- Weigert's hematoxylin (Roth, Cat. No. solution A: X906.1, solution B: X907.1)

Buffers and solutions

4 % paraformaldehyde (PFA)

PFA	4 %
NaOH 1M	0.1 %

Compounds were dissolved in PBS at 65 °C and stirred till the solution got clear. Storage at -20 °C.

20 mM sodiumcitrate

5,882 g sodiumcitrate was dissolved in 1 l of deionized water (dH_2O) and pH was adjusted to 6.

Blocking buffer

Goat serum was dissolved in 0.1 % PBST in a concentration of 2.5 %.

2.9.1 Embedding and cutting of tissue

Small tissue pieces of BAT, WATi, WATg and liver were taken during animal preparation and were transferred to tissue cassettes. These samples were stored in a screw cap bottle with 4 % PFA at 4 °C for 24-48 h.

Fixation continued according to the following scheme (Tab. 8):

Tab. 8: Fixation steps for paraffin embedding of tissue. During steps 1-5 tissue cassettes were kept in a screw cap bottle on a shaking platform.

Step	Repetitions	Time	Solution	Temperature
1	2	2 min	PBS	4 °C
2	3	20 min	50 % EtOH	4 °C
3	3	20 min	70 % EtOH	4 °C
4	3	20 min	95 % EtOH	RT
5	3	20 min	100 % EtOH	RT
6	3	10 min	Xylol	RT
7	2	1 h	Paraffin	60 °C
8		overnight	Paraffin	60 °C

Finally, tissues were embedded in liquid paraffin using Leica EG1160 Embedding Center. Histology blocks were kept at RT. Tissue sections of 5 µm were cut with the Microtome Microme HM355E and dried on microscope slides overnight at 45 °C.

2.9.2 Hematoxylin - Eosin staining (HE staining)

All tissue slides were positioned in a tray for deparaffination and rehydration. Tissue sections were washed 2 minutes each in Xylol, 100 % EtOH, 95 % EtOH, 75 % EtOH and finally PBS.

Hematoxylin staining for nuclei was performed by immersing tissue sections in Hematoxylin solution for 3 seconds. Tissues were immediately transferred to a cuvette with tap water and washed under flowing tap water for 10 min. Eosin staining for cytoplasm was performed by immersing tissue sections in Eosin solution for 1 minute. Subsequently, slides were washed in tap water for 4 minutes on a rocking platform. Tap water was exchanged several times. Afterwards, tissues were dehydrated by reversing the initial rehydrating steps starting with 2 minutes in 75 % EtOH. Finally, all tissue slides were fixed with Roti-Histokitt.

2.9.3 UCP1 staining

Tissue slides were put in a slides tray and were moved from one staining cuvette to the next one according to the following scheme (Tab. 9):

Tab. 9: First part of the UCP1 staining protocol. Na-citrate was heated on a heating magnetic stirrer.

Step	Repetitions	Time	Solution
1	3	5 min	Xylol
2	2	5 min	100 % EtOH
3	2	5 min	96 % EtOH
4	2	5 min	75 % EtOH
5	2	5 min	dH_2O
6	1	5 min	20 mM Na-citrate at 75-80 °C
7	1	5 min	10 mM Na-citrate at 75-80 °C
8	3	5 min	dH_2O
9	1	10 min	3 % H_2O_2
10	1	5 min	dH_2O

Afterwards, tissues were circled with PapPen Liquid Blocker and were incubated with blocking buffer for 1 h. Subsequently, blocking buffer was exchanged by primary UCP1 antibody solution (antibody diluted 1:50 in blocking buffer). Slides were incubated with the primary antibody in a box overnight at 4 °C.

The next day, all tissues were washed 3 x 5 min with PBS and then incubated with the secondary ready-to-use antibody (SignalStain Boost IHC Detection Reagent) for 1 h. In the meantime, DAB solution was prepared according to the manufacturer´s instructions. To allow comparability, all slides of the same tissue were visualised with DAB simultaneously and reaction was stopped with dH_2O when the first piece of tissue turned brown. Slides were washed in dH_2O for 5 minutes and then in PBS for 5 minutes. Finally, Hematoxylin staining, dehydration and fixation was performed as described in 2.9.2.

2.10 Oxysterol measurements

Liver, serum and all AT were taken from 8 weeks old *Ch25h* WT and KO mice in order to investigate oxysterol levels. Tissues were quickly collected and frozen in liquid nitrogen. Samples were sent to our partner laboratory (Giulio Muccioli, Louvain Drug Research Institute, Université Catholique de Louvain, Belgium) on dry ice. Our collaborators measured oxysterol levels using HPLC-MS (Mutemberezi et al., 2016a).

2.11 *In vivo* experiments

Material and equipment

- 12-well, 24-well and 96-well TC plates (Sarstedt, Cat. No. 83.3921, 83.3922, 83.3924)
- AccuCheck Aviva (Roche, Cat. No. 6114986)
- AccuCheck Aviva test stripes (Roche, Cat. No. 06114963)
- Glucose solution 0.25 g/ml (in sterile saline)
- Nuclear magnetic resonance (NMR) minispec analyser instrument (LF50H, Bruker)
- Phenomaster, TSE systems
- Syringe 1 ml (Braun, Ominfix-F Luer Solo, Cat. No. 9161406V)

2.11.1 Analysis of *Ch25h* deficiency in normal conditions

Male *Ch25h* WT and KO mice were obtained with heterozygous breedings. At the age of 9 weeks mice were housed at 23 °C in single cages of the Phenomaster TSE system which allowed indirect calorimetric measurements for each mouse. Locomotion, oxygen (O_2) consumption and carbon dioxide (CO_2) production were recorded for 24 h. Locomotion was measured with an Infrared Motion Sensor (InfraMot, TSE System).

All mice had a daily cycle of 12 h light from 6:00 to 18:00 followed by a period of darkness from 18:00 to 6:00. Humidity was set to 45 % and temperature to 23 °C for the whole period. All mice had permanent access to food and water. Health and weight were assessed daily.

Finally, body composition was analysed using a NMR minispec analyser. Afterwards, mice were narcotised with isoflurane and sacrificed via cervical dislocation. Liver, blood and all AT were taken, weighed and frozen in liquid nitrogen. A little piece of each tissue was saved for histology and stored in 4 % PFA on ice.

2.11.2 Cold exposure experiments

Male *Ch25h* WT and KO mice were obtained with heterozygous breedings. At the age of 8 weeks, mice were acclimatised to a temperature of 16 °C for three days. For the following 7 days, mice were housed at 4 °C in single cages of the Phenomaster TSE system (Fig. 7). The following procedures were the same as described for mice on 23 °C in 2.11.1.

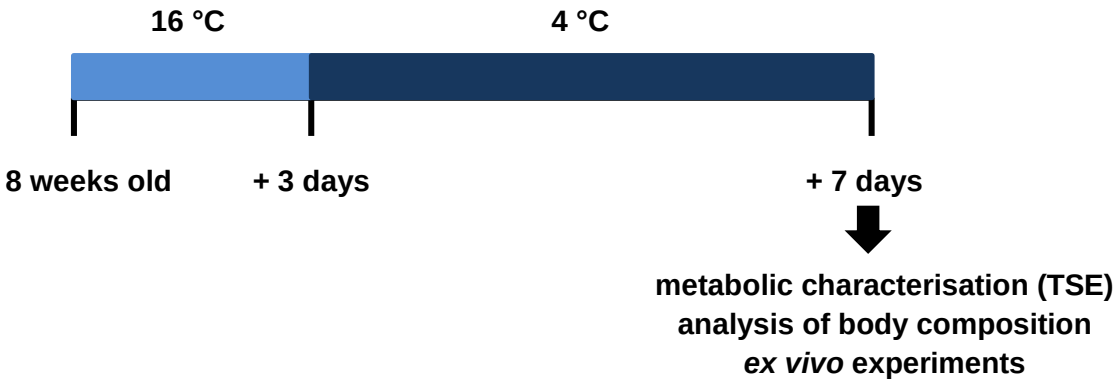

Fig. 7: Experimental setup of cold exposure experiments. 8 weeks old mice were housed in the TSE Phenomaster at 16 °C for three days and subsequently at 4 °C for 7 days. Then mice were sacrificed for further experiments.

2.11.3 Diet induced obesity experiments

Male *Ch25h* WT and KO mice were obtained with heterozygous breedings. At the age of 8 weeks, mice were randomly assigned to be fed with either ND (10 kJ% fat) or HFD (60 kJ% fat) for the following 12 weeks. In week 11 of special diet, mice underwent a glucose tolerance test (GTT, 2.11.4). At the end of week 12 and a final age of 20 weeks, mice were then calorimetrically characterised in the Phenomaster TSE system for two days (Fig. 8). Body composition analysis was performed using a NMR minispec analyser. The following procedures were the same as described for mice on 23 °C in 2.11.1.

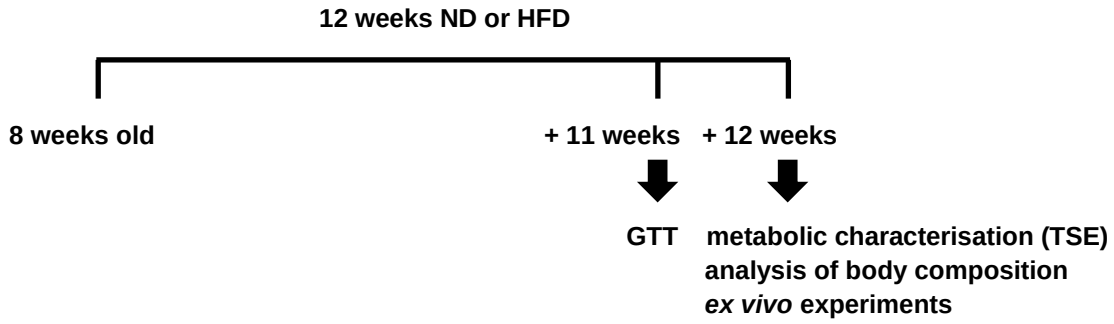

Fig. 8: Experimental setup of diet induced obesity experiments. 8 weeks old *Ch25h* WT and KO mice were either fed with ND or HFD for 12 weeks. After 11 weeks Glucose Tolerance Test (GTT) was performed, one week later metabolism (TSE Phenomaster) and body composition were analysed. Mice were sacrificed for further experiments.

2.11.4 Glucose tolerance test

GTT was performed after 11 weeks of ND or HFD. Mice were starved for 5 h. A piece of tail was cut off in order to obtain a blood drop for the empty-stomached blood glucose level. Subsequently, mice were intraperitoneally injected with 8 µl of 0,25 g/ml glucose solution per g body weight. Blood glucose level was then measured after 30, 60, 90 and 120 minutes using AccuCheck Aviva. Mice were then provided with food again.

2.12 Statistics

All statistical analyses were performed with GraphPad Prism 10. One-way Analysis of variance (ANOVA) and Dunnett's or Bonferroni's Multiple Comparison Test were applied for the analysis of multiple data sets. Two-way ANOVA and Bonferroni post hoc test were performed for GTT and body weight development in the diet induced obesity experiments, Analysis of covariance (ANCOVA) was used for the correlation of body weight and O_2 consumption in all *in vivo* experiments. For all other analyses between two data sets, a two tailed student's t-test was performed.

All data are represented as mean ± standard error of the mean (s.e.m). The number of "n" represents the number of biological replicates (i.e. individuals included in animal experiments and the number of independently of each other differentiated cell cultures in *in vitro* experiments).

3. Results

3.1 Regulation of 7α,25-OHC levels

3.1.1 Expression analysis of 7α,25-OHC-generating enzymes in adipose tissue

To analyse the 7α,25-OHC metabolism in diet induced obesity, mRNA expression of the 7α,25-OHC synthesising enzymes CH25H and CYP7B1 and the 7α,25-OHC degrading enzyme HSD3B7 were determined in BAT, WATi and WATg of mice fed ND or HFD (Fig. 9A-C). Moreover, the expression profile of EBI2 - the endogenous 7α,25-OHC receptor - was analysed (Fig. 9A-C). Liver served as control tissue for these 7α,25-OHC metabolising enzymes (Fig. 9D), whereas spleen served as control tissue for *Ebi2* expression (Fig. 9E).

Expression of both 7α,25-OHC generating enzymes was increased in BAT, WATi and WATg after HFD compared to ND, albeit not significantly (Fig. 9A-C). *Hsd3b7* expression was unchanged in BAT (Fig. 9A), insignificantly higher in WATi (Fig. 9B) and insignificantly lower in WATg (Fig. 9C). The expression of *Ebi2* was higher in all AT after HFD (Fig. 9A-C), albeit not significantly. In liver, the expression of *Cyp7b1* was significantly lower in HFD with a 3-4-fold change (Fig. 9D), whereas no significant changes could be observed for *Ch25h* and *Hsd3b7* expression in liver (Fig. 9D). No significant changes could be detected for *Ebi2* expression in spleen in HFD (Fig. 9E).

In humans, *Ch25h* expression in AT is known to be higher compared to liver, whereas it is the other way round for *Cyp7b1* and *Hsd3b7* expression (Uhlén et al., 2015). In mice, *Ch25h* expression was most abundant in WATg with an approximately 10-fold higher expression compared to BAT and WATi and an even 30-fold higher expression compared to liver (Fig. 9A-D). Conversely, *Cyp7b1* and *Hsd3b7* expression were higher in liver compared to all AT depots in ND and HFD mice (Fig. 9A-D).

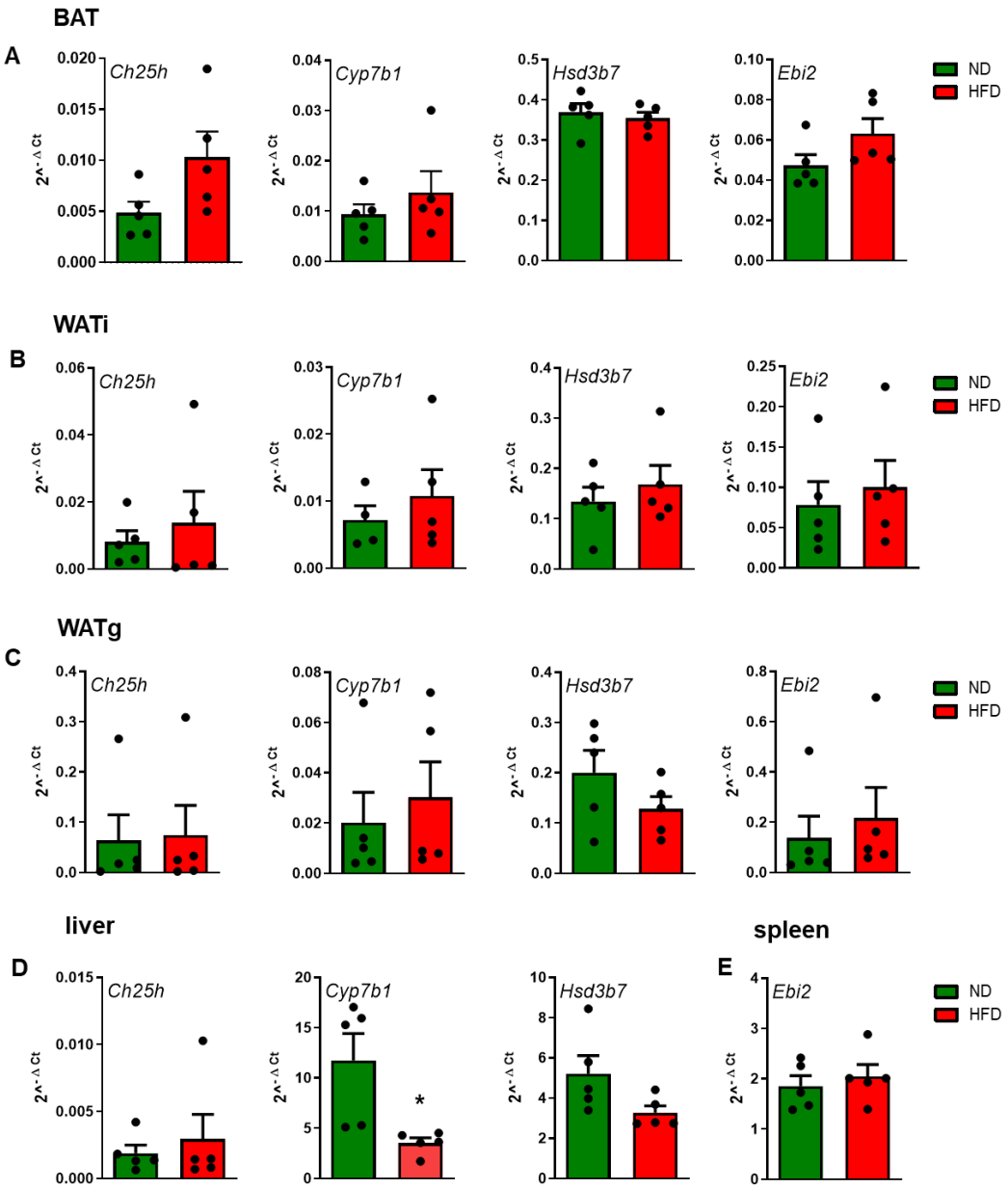

Fig. 9: mRNA expression of key enzymes in 7α,25-OHC metabolism and *Ebi2* in ND and HFD adipose tissues, liver and spleen. mRNA expression of *Ch25h*, *Cyp7b1*, *Hsd3b7* and *Ebi2* in **(A)** BAT, **(B)** WATi and **(C)** WATg; **D** mRNA expression of *Ch25h*, *Cyp7b1* and *Hsd3b7* in liver; **E** mRNA expression of *Ebi2* in spleen; n = 5; Student's t-test; *p < 0.05; mean ± s.e.m.

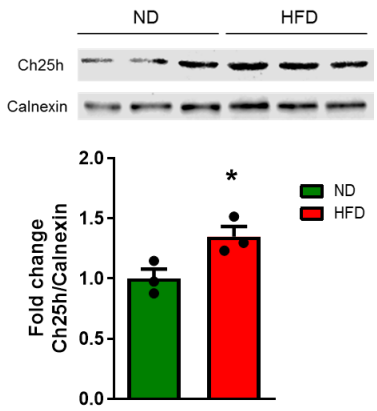

Ch25h expression in BAT was further analysed on protein level: CH25H was significantly higher in HFD compared to ND mice (Fig. 10).

Fig. 10: Protein expression of CH25H in ND and HFD BAT. n = 3, Student's t-test, *p < 0,05; mean ± s.e.m.

Taken together, these data show that all analysed AT depots express the full set of enzymes involved in 7α,25-OHC metabolism. Moreover, expression of *Ch25h* is significantly upregulated in BAT after HFD.

3.1.2 Enzyme expression in ND and HFD SVF and adipocytes

To study the expression of the key 7α,25-OHC-metabolising enzymes on a cellular level, a fractionation of AT from ND and HFD fed mice was performed to obtain floating adipocytes as well as stromal vascular fraction (SVF) from BAT and WATg. SVF comprises all non-adipocyte cells: endothelial cells, immune cells, fibroblasts and preadipocytes (Han et al., 2015).

In BAT, *Ch25h* expression was more abundant in SVF cells compared to mature adipocytes, albeit not significantly. Moreover, the expression of *Cyp7b1* was significantly higher in SVF in ND condition (Fig. 11A). Vice versa, expression of *Hsd3b7* was decreased in SVF cells compared to mature adipocytes, albeit not significantly. *Ebi2* expression was significantly and 28.4-fold higher in ND SVF cells compared to mature fat cells (Fig. 11A). The same tendency for *Ebi2* could be observed in HFD tissues, albeit not significantly (Fig. 11A).

In WATg, *Ch25h* expression was more abundant in SVF cells in ND, whereas it was the other way round in HFD, albeit not significantly in both cases. Moreover, the expression of *Cyp7b1* was significantly higher in SVF cells with a 6-8.6-fold-change compared to ma-

ture adipocytes in both ND and HFD mice (Fig. 11B). Expression of *Hsd3b7* was decreased and 3-3.2-fold lower in SVF cells compared to mature adipocytes, whereas this effect was significant in HFD mice. Moreover, the expression of *Hsd3b7* was significantly higher in HFD adipocytes compared to ND adipocytes (Fig. 11B). For *Ebi2*, expression was more abundant in SVF cells in ND mice, whereas the contrary tendency could be observed in HFD mice, albeit not significantly in both cases. (Fig. 11B).

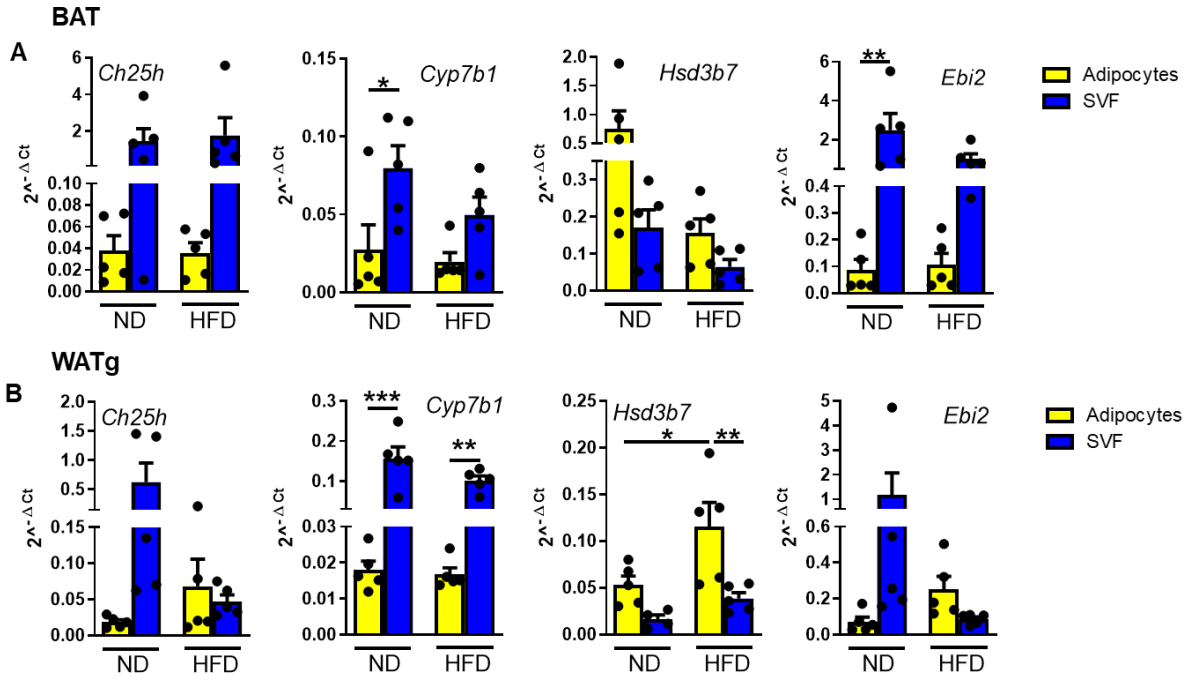

Fig. 11: mRNA expression of key enzymes in 7α,25-OHC metabolism and *Ebi2* in ND and HFD adipocytes and SVF. mRNA expression of *Ch25h*, *Cyp7b1*, *Hsd3b7* and *Ebi2* in **(A)** BAT and **(B)** WATg adipocytes and SVF. n = 5; One-way ANOVA with Bonferroni´s multiple comparisons tests; *p < 0.05, **p < 0.01, ***p < 0.001; mean ± s.e.m.

Overall, *Ch25h* and *Cyp7b1* showed the tendency of lower expression in HFD SVF compared to ND SVF - apart from *Ch25h* in BAT - in both AT depots. This was also evident for the receptor EBI2. The same tendency could be noticed for *Hsd3b7* expression in BAT whereas the expression was higher in the SVF of HFD WATg compared to the ND condition (Fig. 11A/B). Together, these data might indicate that 7α,25-OHC is produced predominantly in SVF and degraded by mature adipocytes. Moreover, 7α,25-OHC levels might be decreased in the SVF under HFD condition, especially in WATg.

3.2 Co-cultivation experiments

As the conducted expression analysis revealed higher abundance of *Ch25h* and *Cyp7b1* in the SVF compared to mature adipocytes isolated from BAT (cf Fig. 11A), co-cultivation studies of BA with macrophages, endothelial cells and fibroblasts were performed to examine a potential influence/crosstalk of those non-adipocyte cells on brown fat cell function and metabolism.

3.2.1 Bone marrow-derived macrophage - brown adipocyte co-cultivation

7α,25-OHC exerts main functions in innate and adaptive immune response and attracting lymphocytes (Hannedouche et al., 2011; Liu et al., 2011). *Ch25h* expression and 7α,25-OHC production were shown to be high in macrophages and even increased upon LPS stimulation (Preuss et al., 2014). As immune cells are known to crosstalk to white adipocytes (Huh et al., 2014), the co-cultivation studies performed here aimed at investigating the influence of BMDM on BA function. BMDM were co-cultivated *in vitro* with BA for 72 h using a transwell system. BMDM were either treated with LPS 24 h before co-cultivation to induce M_{LPS} which comprise an activated proinflammatory phenotype of macrophages or remained unpolarised inactive M_0 macrophages. After co-cultivation, BA function was analysed by measuring lipolysis.

Basal lipolysis was similar between BA and BA co-cultured with M_0. However, lipolysis was significantly higher after co-cultivation with $M_{LPS.}$ (Fig. 12). Together, these data show that LPS polarised, but not unpolarised macrophages elevated BA lipolysis.

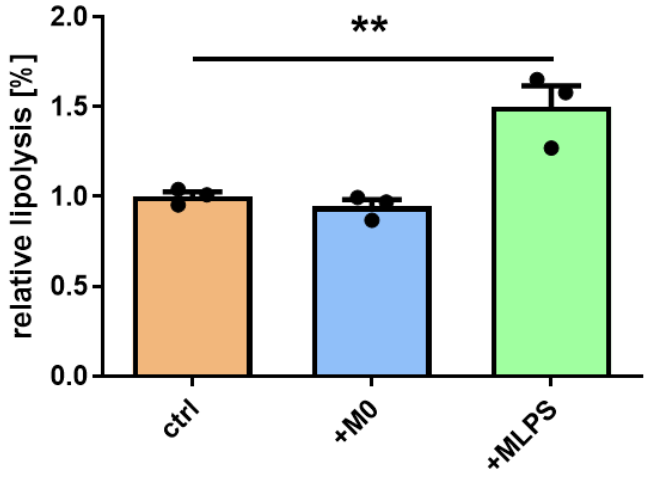

Fig. 12: 72 h BMDM co-cultivation studies. Lipolysis of BA after 72 h of co-cultivation with M_0/M_{LPS}. n = 3; One-way ANOVA with Dunnett's Multiple Comparison Test; **p < 0.01; mean ± s.e.m.

3.2.2 Co-cultivation of BA with fibroblasts and endothelial progenitors

Fibroblasts and endothelial cells are also known to regulate inflammatory processes like fibrosis, atherosclerosis, and endothelial cell dysfunction (Gimbrone et al., 2016; Jordana et al., 1994) which are also pathophysiological conditions in AT inflammation. Therefore, NIH-3T3 fibroblasts and T17b endothelial progenitor cells were co-cultivated with BA for 72h to study their potential role in the regulation of the BA thermogenic capacity, which was examined with UCP1 Western Blot after co-cultivation.

Co-cultivation of BA with both fibroblasts and endothelial progenitor cells resulted in a significant 10.1-14.4-fold decrease of UCP1 expression on protein level in BA (Fig. 13A/B). These data show, that fibroblasts and endothelial cells can decrease the thermogenic capacity of BA.

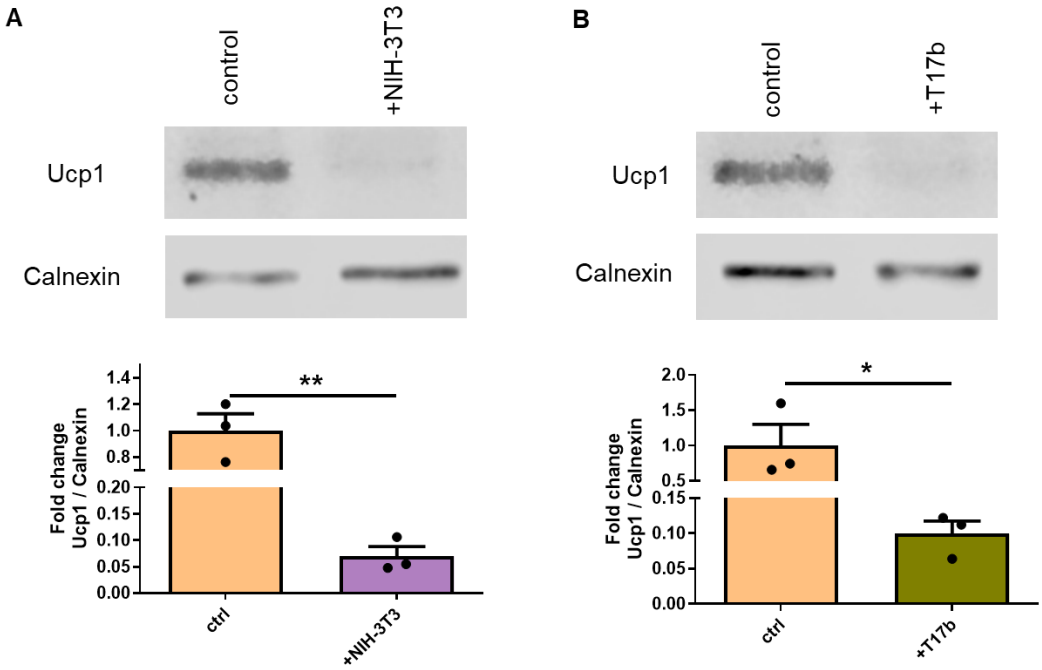

Fig. 13: Co-cultivation of NIH-3T3 and T17b with brown adipocytes. UCP1 protein expression of BA after co-cultivation with **(A)** NIH-3T3 fibroblasts and **(B)** T17b endothelial progenitor cells for 72 h. n = 3; Student's t-test; *p < 0.05, **p < 0.01; mean ± s.e.m.

3.3 Oxysterol measurements

To study the levels of oxysterols, liver, serum, BAT, WATi and WATg were isolated from 8 weeks old *Ch25h* WT and KO mice and analysed in collaboration with Prof. G. G. Muccioli (Université Catholique de Louvain, Belgium) using HPLC-MS. Oxysterol levels were only compared between WT and KO for each tissue to identify potentially altered synthesis pathways in KO mice. Fig. 14 shows a synopsis of the results. Unexpectedly, no difference could be observed in 7α,25-OHC levels between *Ch25h* WT and KO mice in all samples analysed (Fig. 15A) although Hannedouche et al. (2011) reported that *Ch25h* KO mice displayed almost non-detectable 7α,25-OHC levels in spleen. However, the CH25H dependent hydroxylation product 25-OHC was reduced in all fat depots, albeit not significantly. Similarly, levels of 7-keto-25-OHC were significantly lower in WATg of KO mice with a 1.7-fold change. Similarly, the levels of 7-keto-25-OHC were insignificantly reduced in BAT and WAT (Fig. 15B/E). Moreover, 4-cholesten-7α-ol-3-one (7α-OHCnone) is known to be a HSD3B7-mediated degradation product of 7-OHC. Similarly to its precursor, decreased levels in BAT and WATi of KO mice were observed (Fig. 15G/H). Interestingly, levels of the CYP27A1 hydroxylation product 27-OHC were significantly higher in BAT and significantly lower in WATg of *Ch25h* KO mice (Fig. 15C). In addition, CYP27A1 is known to catalyse 25-hydroxylations (Lund et al., 1993), therefore altered CYP27A1 activity also needs to be considered regarding 7α,25-OHC synthesis. In contrast, for some oxysterols such as 4β-OHC, 7-ketocholesterol and 24(S)-OHC, no considerable level changes were observed in KO mice (Fig. 15D/F/I). Levels of 5α,6α-epoxycholesterol and 5β,6β-epoxycholesterol, which are completely ROS-dependent hydroxylation products, remained stable or decreased in KO condition indicating that autoxidation is not supposed to be related to the altered oxysterol levels in KO mice (Fig. 15J/K). Both epoxides are known to be enzymatically converted to 5α,6β-OHC which did not show any significant level changes as well (Fig. 15L).

Fig. 14 (page 59): Synopsis of analysed oxysterol levels in *Ch25h* KO mice related to their synthesising and degrading enzymes. The coloured boxes show changes in oxysterol levels of *Ch25h* KO mice compared to WT mice. Red colour indicates higher concentrations in KO mice, whereas blue colour signifies lower oxysterol concentrations. From left to right the boxes represent liver, serum, BAT, WATi and WATg. Stars in the boxes indicate significant concentration changes based on the Student's t-tests performed in Fig. 15. The representation of metabolic pathways and involved enzymes is based on Guillemot-Legris et al., 2016b; Mutemberezi et al., 2016b and Russell, 2000.

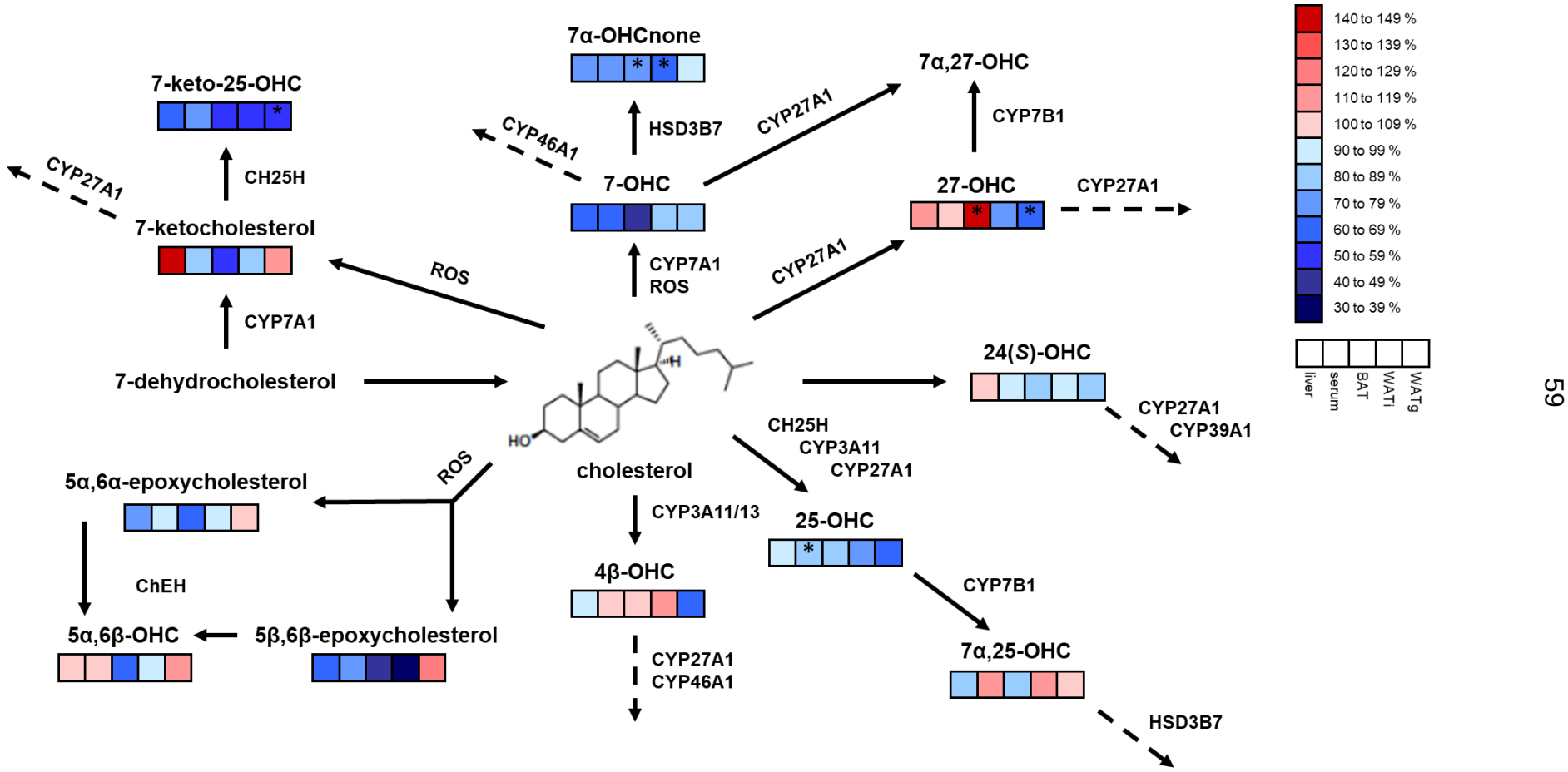
7α-OHCnone
7-keto-25-OHC
7α,27-OHC
CYP46A1
HSD3B7
CYP27A1
CYP7B1
CYP27A1
CH25H
7-OHC
27-OHC
CYP27A1
7-ketocholesterol
ROS
CYP7A1
ROS
CYP27A1
CYP7A1
7-dehydrocholesterol
24(S)-OHC
CYP27A1
CYP39A1
CH25H
CYP3A11
CYP27A1
cholesterol
5α,6α-epoxycholesterol
ROS
CYP3A11/13
25-OHC
ChEH
4β-OHC
CYP7B1
5α,6β-OHC
5β,6β-epoxycholesterol
CYP27A1
CYP46A1
7α,25-OHC
HSD3B7
140 to 149 %
130 to 139 %
120 to 129 %
110 to 119 %
100 to 109 %
90 to 99 %
80 to 89 %
70 to 79 %
60 to 69 %
50 to 59 %
40 to 49 %
30 to 39 %
liver
serum
BAT
WATi
WATg

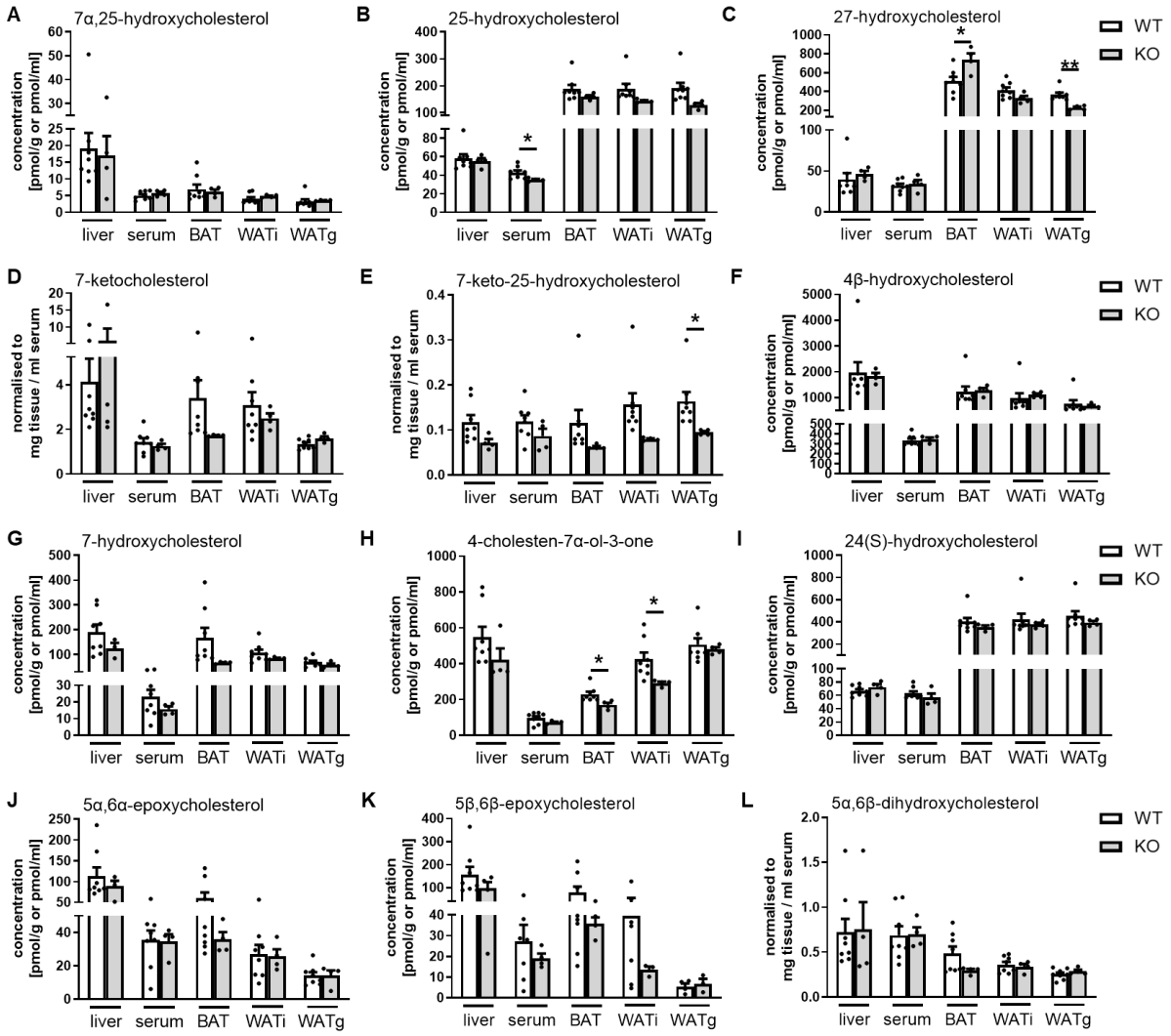

Fig. 15: Oxysterol levels in liver, serum and adipose tissue of *Ch25h* WT and KO mice using HPLC-MS. Concentration of **(A)** 7α,25-OHC, **(B)** 25-OHC, **(C)** 27-OHC, **(D)** 7-ketocholesterol, **(E)** 7-keto-25-OHC, **(F)** 4β-OHC, **(G)** 7-OHC, **(H)** 4-cholesten-7α-ol-3-one (7α-OHCnone), **(I)** 24(S)-OHC, **(J)** 5α,6α-epoxycholesterol, **(K)** 5β,6β-epoxycholesterol and **(L)** 5α,6β-OHC in liver, serum, BAT, WATi and WATg. n = 8 for WT mice, n = 4 for KO mice; Student's t-test; *p < 0.05, **p < 0.01; mean ± s.e.m.

Taken together, these data indicate that whole-body knockout of *Ch25h* did not significantly change 7α,25-OHC levels in the tissues analysed, whereas other CH25H hydroxylation products as 25-OHC and 7-keto-25-OHC showed decreased levels. Potential reasons for this discrepancy are taken into consideration in the discussion.

3.4 *In vivo* experiments

3.4.1 The role of *Ch25h in vivo*

To study the role of *Ch25h in vivo*, whole-body metabolism of mice deficient for *Ch25h* was analysed at standard housing conditions, i.e., 23°C using metabolic cages (TSE Phenomaster). Mice were 8 weeks old and were fed with standard food provided by Haus of experimentelle Therapie, Universitätsklinikum Bonn.

3.4.1.1 Indirect calorimetry of *Ch25h* WT and KO mice

O_2 consumption, CO_2 production and locomotor activity were recorded for 24 h in the TSE Phenomaster. The average amount of consumed O_2 and produced CO_2 was recorded in ml/h every 14 minutes. Every data point was used for the calculation of AUC resulting in an approximately 4-fold higher value. Respiratory exchange ratio (RER) was calculated as CO_2/O_2 ratio as indication of the preferred energy source, i.e., 0.7 = predominantly carbohydrates and 1.0 = predominantly fat (Speakman, 2013). Locomotor activity was recorded as counts for every movement detected by the motion sensor.

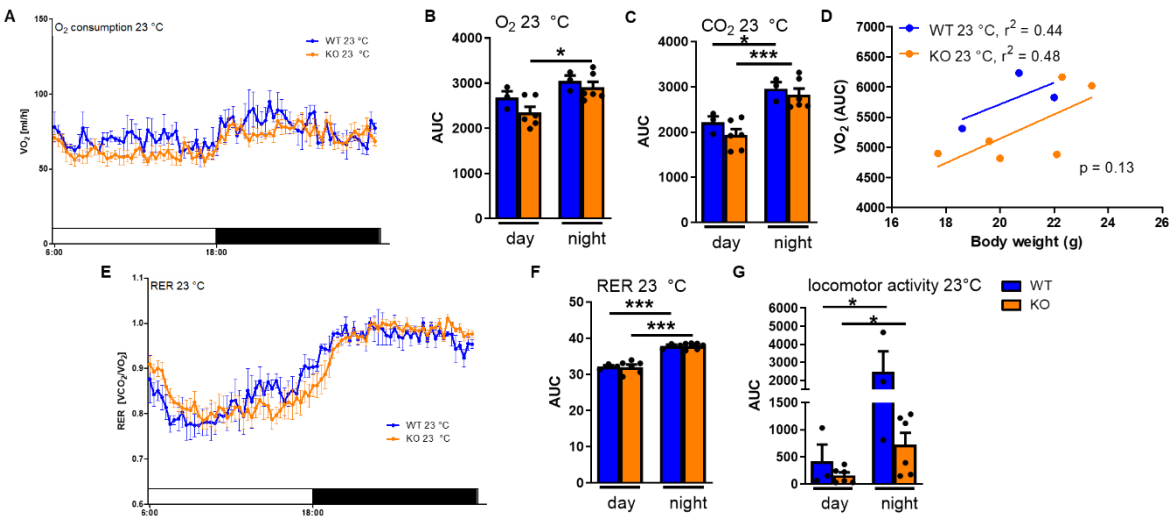

Fig. 16: Indirect calorimetry of *Ch25h* WT and KO mice at 23 °C. Profile of **(A)** O_2 consumption and **(E)** RER during day and night; Area under the curve (AUC) for **(B)** O_2 consumption, **(C)** CO_2 production, **(F)** RER and **(G)** locomotor activity divided in day and night; **D** ANCOVA analysis of VO_2 (AUC) over 24 h in relation to body weight; n = 3 for WT mice, n = 6 for KO mice; AUC and One-way ANOVA with Bonferroni´s multiple comparisons tests; *p < 0.05, ***p < 0.001; mean ± s.e.m.

Overall, *Ch25h* KO mice consumed less O_2 and produced more CO_2 compared to WT control mice independent of day time, albeit not significantly (Fig. 16A-C). Additionally, this effect was seen when correlating O_2 consumption to body weight (Fig. 16D). Again, this effect did not reach statistical significance. RER was not significantly changed suggesting that both genotypes used the same energy source in whole-body metabolism (Fig. 16E/F). *Ch25h* WT mice tended towards more locomotor activity compared to KO mice (Fig. 16G).

3.4.1.2 Analysis of body and tissue composition of *Ch25h* WT and KO mice

Next, body composition was analysed using a small animal NMR minispec analyser.
No differences were observed in fat and lean mass between both genotypes, while KO mice had significantly more free water (Fig. 17A). Moreover, organ weights of AT depots and liver were similar in *Ch25h* KO compared to WT mice (Fig. 17B). Histological analysis revealed no differences between KO and WT in BAT and WAT (Fig. 17C).

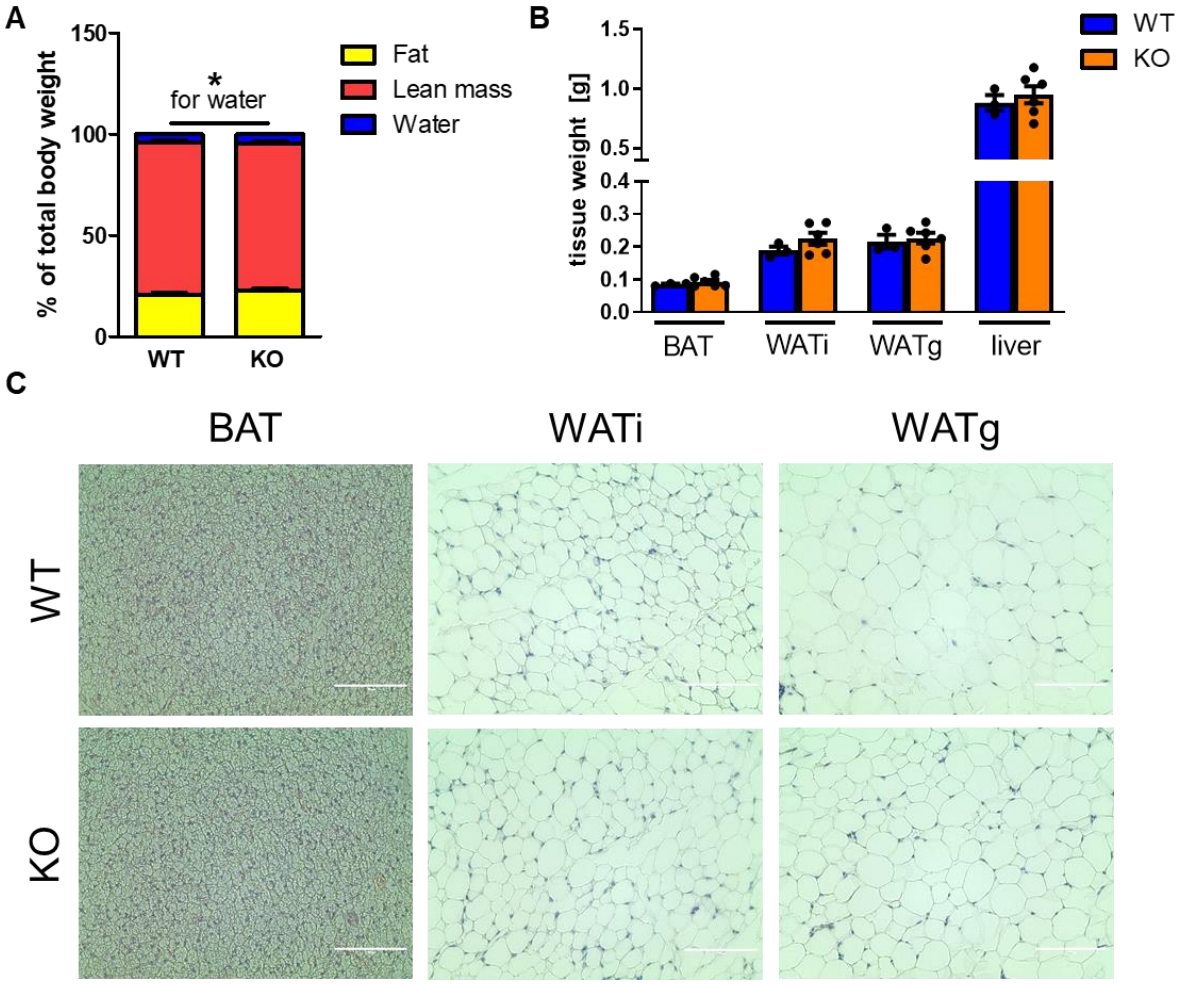

Fig. 17: Analysis of body and tissue composition of *Ch25h* WT and KO mice at 23 °C. A Body composition (fat, water and lean mass) of *Ch25h* WT/KO mice as proportion of total body weight; **B** tissue weights of BAT, WATi, WATg and liver of *Ch25h* WT/KO mice as proportion of total body weight; **C** HE staining of BAT (left), WATi (middle) and WATg (right) from *Ch25h* WT (up) and KO (down) mice. Scale bar: 100 µm. n = 3 for WT mice, n = 6 for KO mice; *p < 0.05; Student's t-test; mean ± s.e.m.

3.4.1.3 Analysis of UCP1 expression of *Ch25h* WT and KO mice

Next, UCP1 content was analysed using qPCR, Western Blot and histology. No differences were observed for *Ucp1* expression in all AT depots isolated from *Ch25h* WT or KO mice (Fig. 18A/B). Histologically, no substantial differences in DAB intensity were detected in WT and KO BAT, WATi and WATg (Fig. 18C).

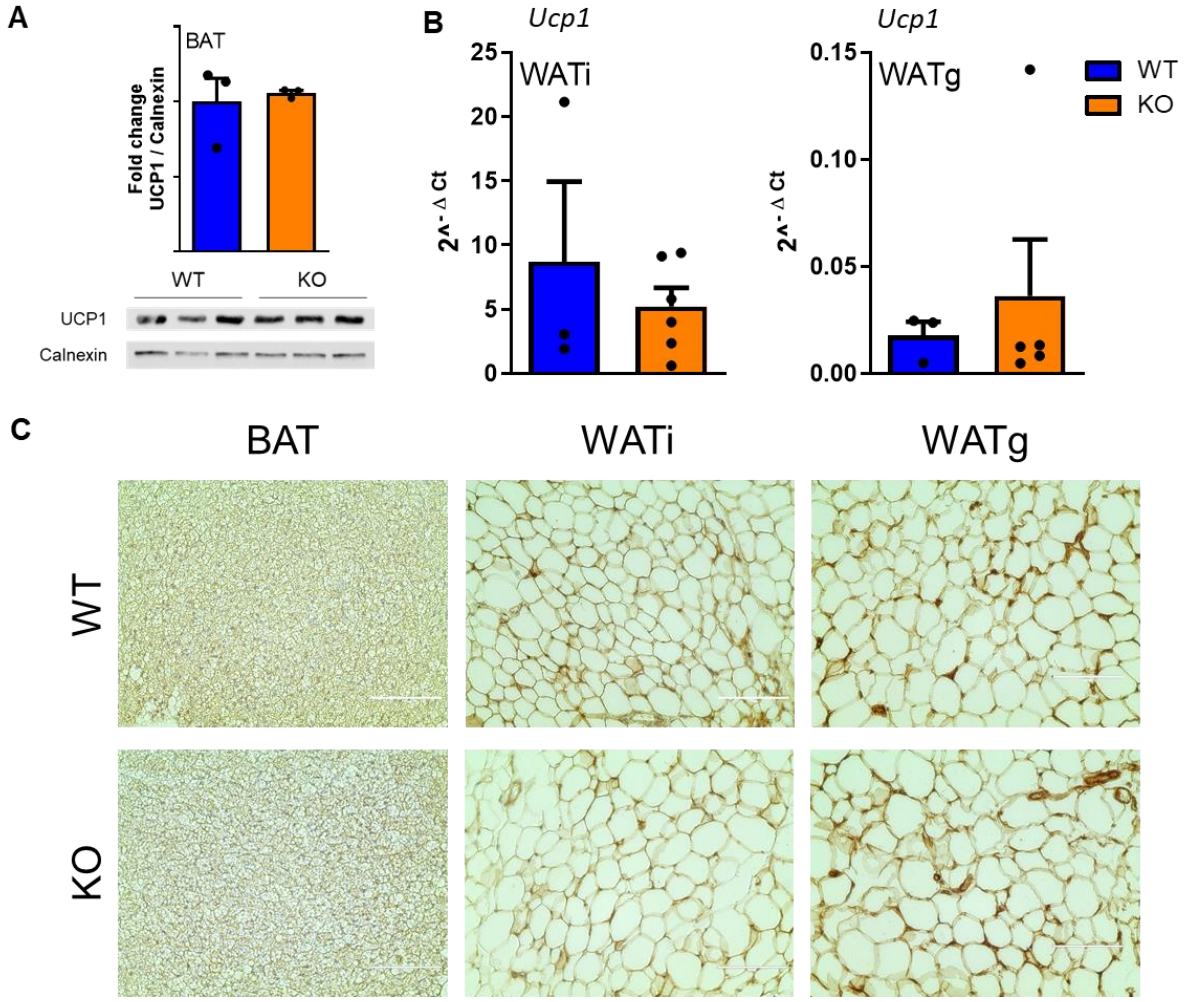

Fig. 18: Analysis of UCP1 expression in *Ch25h* WT and KO mice at 23 °C. A protein expression of UCP1 in BAT; **B** mRNA expression of *Ucp1* in BAT, WATi and WATg; **C** UCP1 DAB staining of BAT (left), WATi (middle) and WATg (right) from *Ch25h* WT (up) and KO (down) mice. Scale bar: 100 µm; qPCR: n = 3 for WT mice, n = 6 for KO mice; Western Blot: n = 3 for WT and KO. Student's t-test; mean ± s.e.m.

3.4.1.4 *Ex vivo* lipolysis of *Ch25h* WT and KO mice

To analyse the influence of *Ch25h* on AT function, *ex vivo* lipolysis of BAT and WAT from KO and WT mice was performed under basal conditions, as well as after NE or forskolin treatment. Forskolin is a widely used AC stimulator which increases intracellular cAMP levels (Alasbahi et al., 2012).

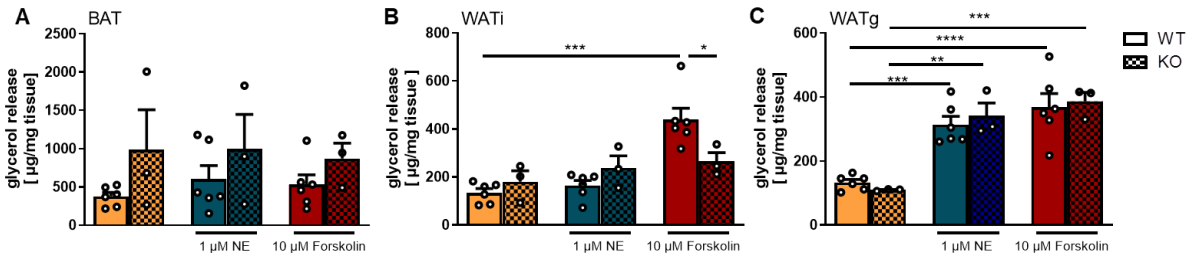

Fig. 19: *Ex vivo* lipolysis of *Ch25h* WT and KO mice without treatment, with 1 µM NE and 10 µM forskolin. *Ex vivo* lipolysis in **(A)** BAT, **(B)** WATi and **(C)** WATg. n = 3 for KO mice, n = 6 for WT mice; One-way ANOVA with Bonferroni´s multiple comparisons tests; *p < 0.05, **p < 0.01, ***p < 0.001, ****p < 0.0001; mean ± s.e.m.

In BAT, basal lipolysis was 2.6-fold higher in KO compared to WT tissue, albeit not significantly. Moreover, lipolysis was 1.6-1.7-fold higher upon NE and forskolin treatment in BAT deficient for *Ch25h* compared to WT. However, these effects were not statistically significant (Fig. 19A). In WATi, the tendency towards more lipolysis in KO mice was less clear than in BAT. Instead, lipolytic rate was significantly increased and 3.3-fold higher in WT tissue upon forskolin administration (Fig. 19B). Furthermore, a significantly higher lipolytic rate could be detected in WT mice upon forskolin stimulation in contrast to KO mice (Fig. 19B). In WATg, no difference was seen between lipolytic rates of WT and KO tissue. However, lipolytic rate was significantly increased with a 2.8-3.4-fold change upon NE and forskolin administration for both genotypes (Fig. 19C).

Together, these data indicate that *Ch25h* KO mice have more basal lipolytic activity especially in BAT. Independent of the examined genotype, basal lipolytic activity can be increased upon adrenergic stimulation especially in WAT.

3.4.2 The role of *Ch25h* in WAT browning

Prolonged cold exposure is known to induce WATi browning, a process by which white adipocytes gain a BA-like character due to an increased number of mitochondria and UCP1 expression (Lo et al., 2013). To study the effect of *Ch25h* deficiency in browning, *Ch25h* WT and KO mice were exposed to acclimatisation at 16 °C for 3 days followed by 4 °C for 1 week.

3.4.2.1 Indirect calorimetry of *Ch25h* WT and KO mice during cold exposure

Similar to the analysis of whole-body metabolism at 23° C, O_2 consumption, CO_2 production and locomotion were recorded for 24 h using metabolic cages.

Ch25h KO mice had a significantly higher EE during the night compared to WT mice (Fig. 20A/B). CO_2 production was also significantly higher during day as well as during night (Fig. 20C). Importantly, ANCOVA analysis revealed that EE was higher in KO mice independent of body weight (p = 0.06) (Fig. 20D). As O_2 consumption and CO_2 production was equally increased in KO mice, no difference was detected for RER indicating that both genotypes used the same energy source (Fig. 20E/F). No significant difference was observed in locomotor activity (Fig. 20G).

Taken together, these data show that loss of *Ch25h* increases EE of mice.

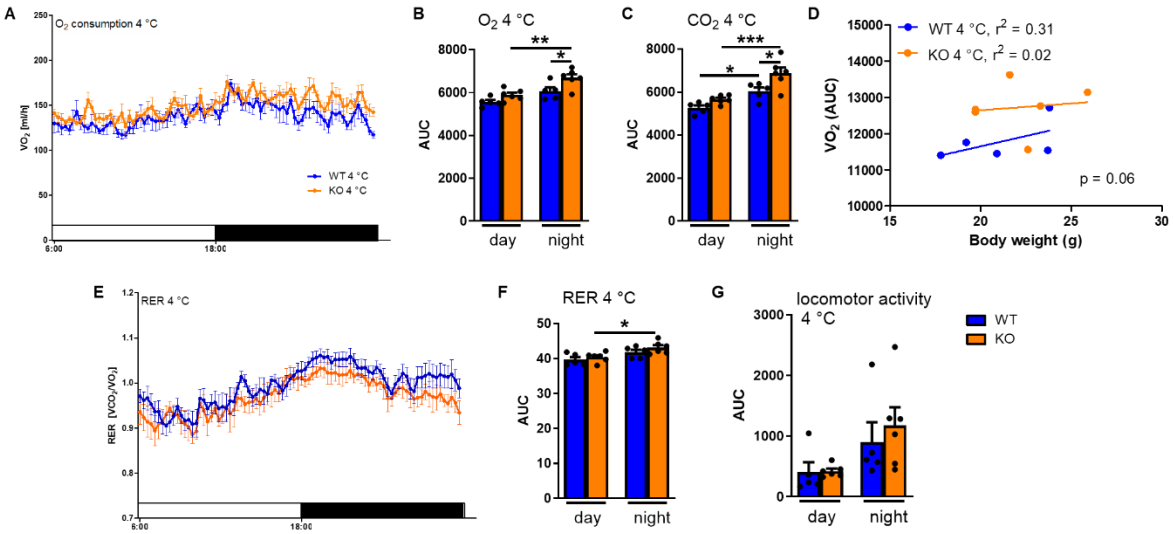

Fig. 20: Indirect calorimetry of *Ch25h* WT and KO mice at 4 °C. Profile of **(A)** O_2 consumption and **(E)** RER during day and night; Area under the curve (AUC) for **(B)** O_2 consumption, **(C)** CO_2 production, **(F)** RER and **(G)** locomotor activity divided in day and night; **D** ANCOVA analysis of VO_2 (AUC) over 24 h in relation to body weight; n = 5 for WT mice, n = 6 for KO mice; AUC and One-way ANOVA with Bonferroni´s multiple comparisons tests; *p < 0.05, **p < 0.01, ***p < 0.001; mean ± s.e.m.

3.4.2.2 Analysis of body and tissue composition of *Ch25h* WT and KO mice during cold exposure

After indirect calorimetry, body composition was analysed using NMR minispec analyser. No changes were observed in body weight and body composition except that *Ch25h* KO mice had more free water than WT mice at 4 °C (Fig. 21A).

Interestingly, KO mice had significantly more BAT mass than WT mice. A similar trend was observed for WAT, albeit to no statistical significance (Fig. 21B). While histological analysis of BAT showed no difference between *Ch25h* KO and WT (Fig. 21C), an increased number of multilocular adipocytes with smaller lipid droplets in WAT depots was observed indicative of WAT browning in WT mice (Fig. 21C).

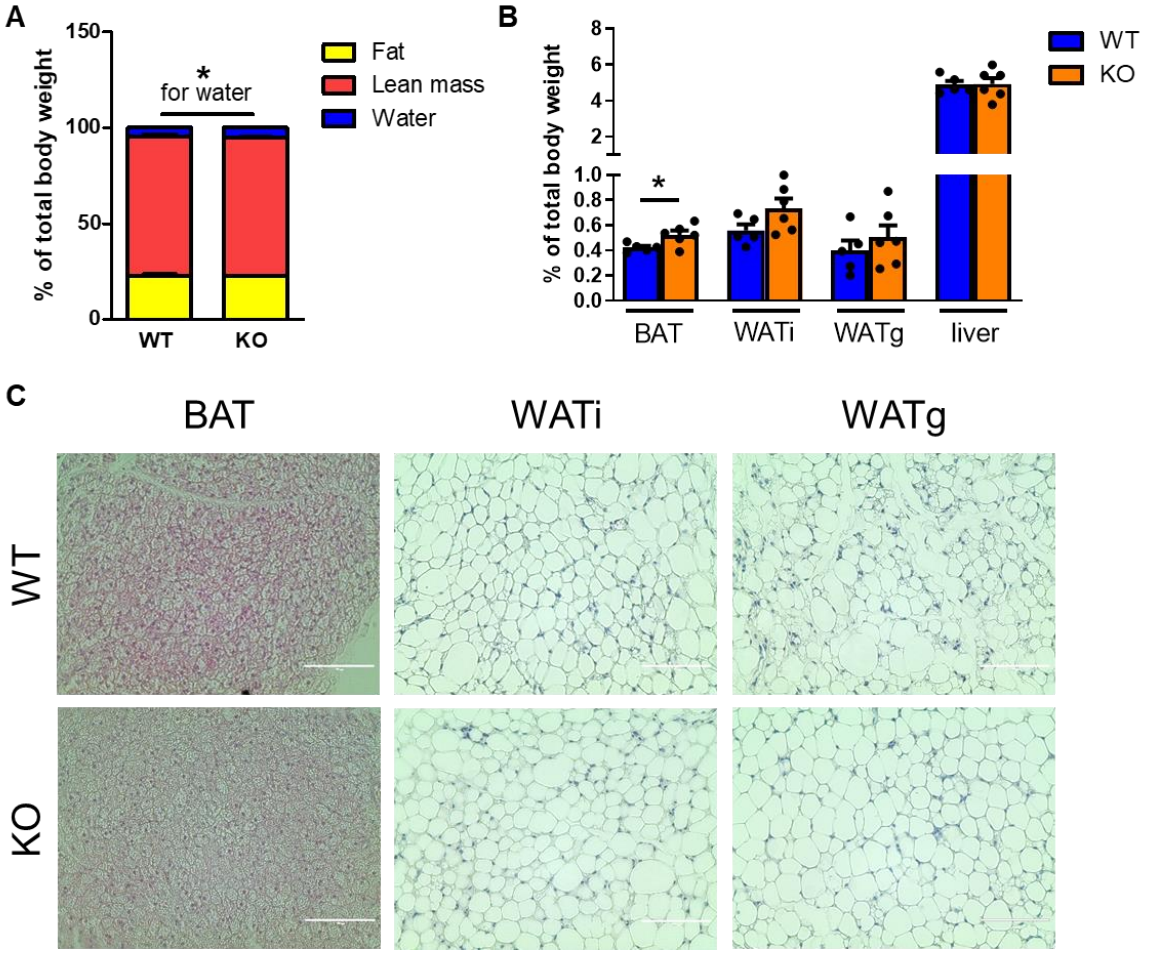

Fig. 21: Analysis of body and tissue composition of *Ch25h* WT and KO mice at 4 °C. **A** Body composition (fat, water and lean mass) of *Ch25h* WT/KO mice as proportion of total body weight; **B** tissue weights of BAT, WATi, WATg and liver of *Ch25h* WT/KO mice as proportion of total body weight; **C** HE staining of BAT (left), WATi (middle) and WATg (right) from *Ch25h* WT (up) and KO (down) mice. Scale bar: 100 µm. n = 5 for WT mice, n = 6 for KO mice; Student's t-test; *p < 0.05; mean ± s.e.m.

These data show that mice deficient for *Ch25h* have higher EE upon prolonged cold stress and increased BAT mass. However, total fat mass was not significantly changed.

3.4.2.3 Analysis of UCP1 expression of *Ch25h* WT and KO mice during cold exposure

In line with the increased EE of *Ch25h* KO mice, we found 2-fold higher UCP1 protein expression in BAT (Fig. 22A). Moreover, *Ucp1* expression was increased in WATi as well as in WATg of *Ch25h* KO mice, although not significantly (Fig. 22B). Histological analysis of AT sections revealed no substantial differences in UCP1 staining between both genotypes (Fig. 22C). Together, these data indicate that mice deficient of *Ch25h* exhibit increased UCP1 protein expression in AT after cold exposure.

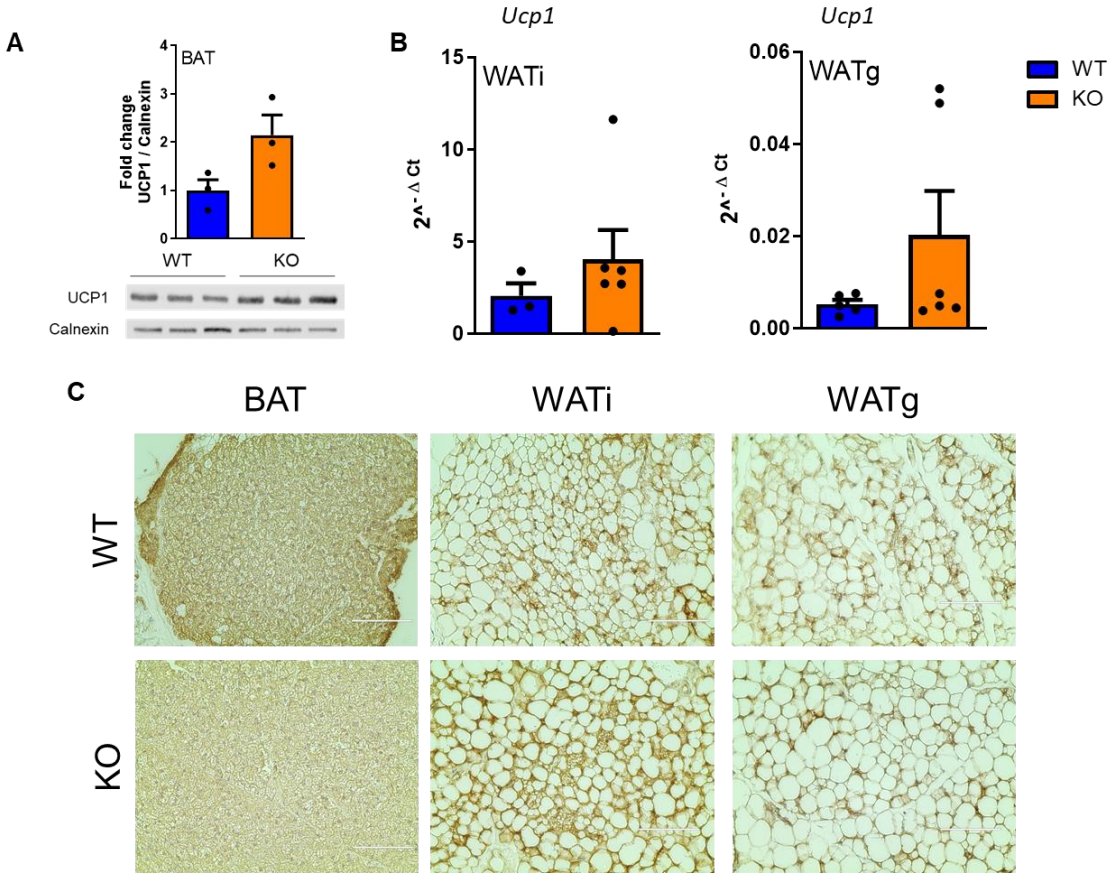

Fig. 22: Analysis of UCP1 expression in *Ch25h* WT and KO mice at 4 °C. A protein expression of UCP1 in BAT; **B** mRNA expression of *Ucp1* in WATi (left) and WATg (right); **C** UCP1 DAB staining of BAT (left), WATi (middle) and WATg (right) from *Ch25h* WT (up) and KO (down) mice. Scale bar: 100 µm; qPCR: n = 5 for WT mice, n = 6 for KO mice; Western Blot: n = 3 for WT and KO. Student's t-test; mean ± s.e.m.

3.4.3 Analysis of *Ch25h* deficiency in diet induced obesity

To study the effect of *Ch25h* in diet induced obesity, 8 weeks old *Ch25h* WT and KO mice were either fed with a ND (10% fat) or HFD (60% fat) for 12 weeks. Final analyses were performed at the age of 20 weeks.

3.4.3.1 Body weight development and Glucose Tolerance Test

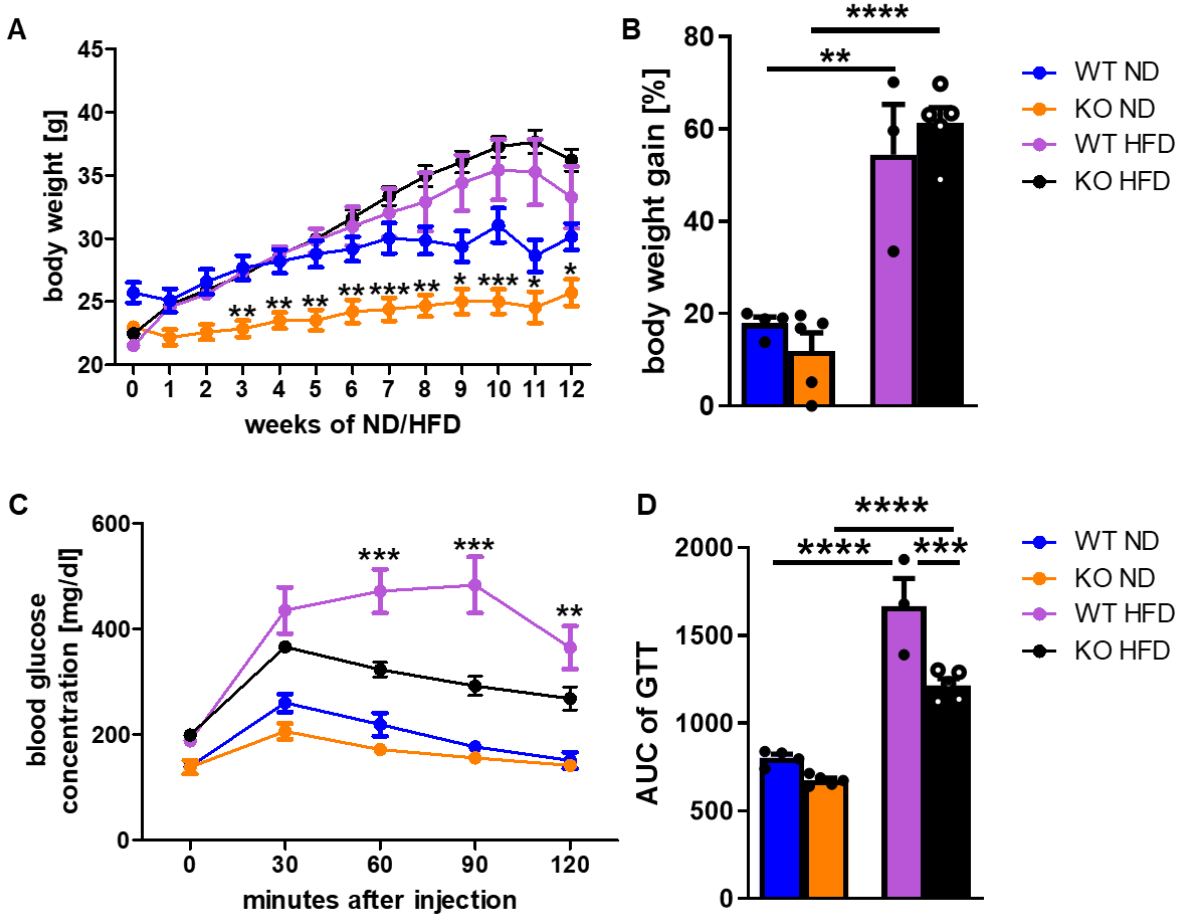

Fig. 23: Body weight development and Glucose Tolerance Test of *Ch25h* WT and KO mice after 12 weeks on either ND or HFD. A Body weight development of *Ch25h* WT/KO mice during 12 weeks of ND/HFD. Two-way ANOVA: time effect, genotype effect, interaction p < 0,0001; Bonferroni post hoc tests: WT ND vs. KO ND *p < 0.05, **p < 0.01, ***p < 0.001; **B** Relative body weight gain of *Ch25h* WT/KO mice during 12 weeks of ND/HFD. One-way ANOVA with Bonferroni´s multiple comparisons tests; **p < 0.01, ****p < 0.0001; mean ± s.e.m. **C** Intraperitoneal GTT in *Ch25h* WT/KO mice after 11 weeks of ND/HFD. Two-way ANOVA: time effect, genotype effect, interaction p < 0,0001; Bonferroni post hoc tests: WT HFD vs. KO HFD **p < 0.01, ***p < 0.001; **D** AUC of GGT, One-way ANOVA with Bonferroni´s multiple comparisons tests; ***p < 0.001, ****p < 0.0001; mean ± s.e.m. n = 3 for WT mice on HFD, n = 4 for WT mice on ND, n = 5 for KO mice on ND and HFD

As expected, mice of all four experimental conditions continuously gained weight during the course of the study. A drop in body weight during the last week of ND/HFD was observed, most likely due to changed environmental conditions in the TSE phenomaster system. However, beginning from week 6, KO mice gained more weight than WT mice on HFD, albeit not significantly. Although mice were assigned randomly to experimental groups, WT mice on ND had a higher body weight compared to WT mice on HFD during the first weeks. Related to that initial difference, WT mice on ND were also significantly heavier throughout the experiment in comparison to the ND KO group (Fig. 23A). However, there was no significant difference in relative body weight gain between *Ch25h* WT and KO mice in both experimental groups (Fig. 23B).

Nonetheless, both ND groups had the same fasting blood glucose level in GTT. KO mice showed a slightly flattened increase in blood glucose concentration after intraperitoneal glucose injection compared to WT mice. More importantly, KO mice on HFD showed a significantly faster normalisation of blood glucose concentration in comparison to WT mice (Fig. 23C). Also, in the comparison of AUC of GTT, KO mice showed a significantly faster glucose clearance in contrast to WT especially on HFD (Fig. 24D).

In conclusion, KO mice showed a healthier glucose homeostasis than WT mice even in the HFD condition.

3.4.3.2 Indirect calorimetry of *Ch25h* WT and KO mice in diet-induced obesity

During the final week of the diet induced obesity study, indirect calorimetry was measured in a TSE Phenomaster system. O_2 consumption, CO_2 production and locomotion were recorded for 24 h.

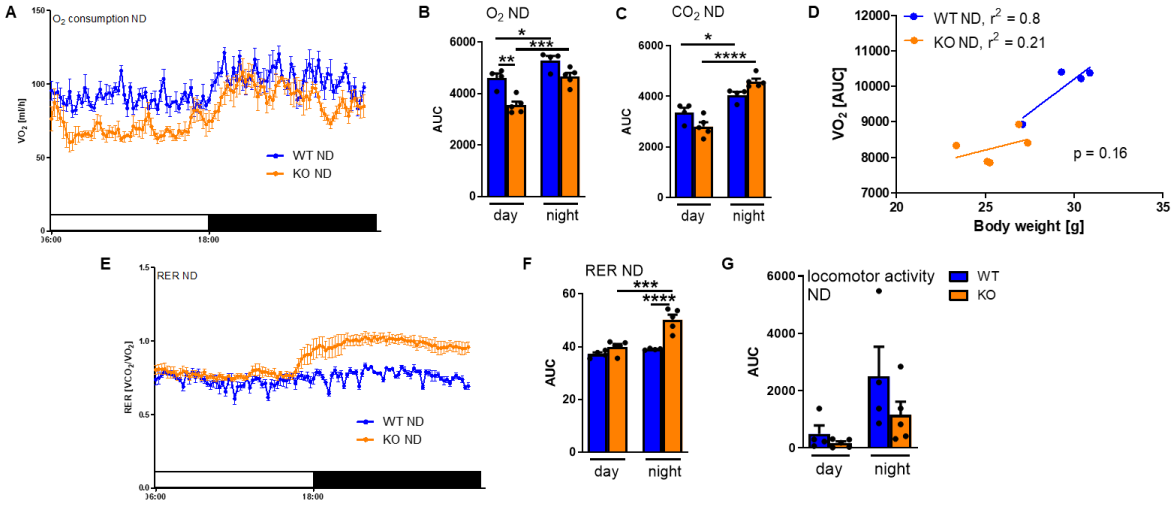

Fig. 24: Indirect calorimetry of *Ch25h* WT and KO mice after 12 weeks on ND. Profile of **(A)** O_2 consumption and **(E)** RER during day and night; Area under the curve (AUC) for **(B)** O_2 consumption, **(C)** CO_2 production, **(F)** RER and **(G)** locomotor activity divided in day and night; **D** ANCOVA analysis of VO_2 (AUC) over 24 h in relation to body weight; n = 4 for WT mice on ND, n = 5 for KO mice on ND; AUC and One-way ANOVA with Bonferroni´s multiple comparisons tests; *p < 0.05, **p < 0.01, ***p < 0.001, ****p < 0.0001; mean ± s.e.m.

Under ND conditions, *Ch25h* KO mice showed a significantly lower EE compared to WT mice especially during the day (Fig. 24A/B). There was no significant difference in CO_2 production between WT and KO mice on ND (Fig. 24C). Importantly, the correlation of O_2 consumption to body weight showed that the lower EE in ND KO mice was due to lower body weight (Fig. 24D).

The calculated RER (Fig. 24E/F) was significantly higher for ND KO mice during the night compared to ND WT mice indicating that ND KO mice had a rather carbohydrate-driven whole-body metabolism whereas ND WT used a mixed energy source of both fat and carbohydrates.

Locomotor activity was generally higher during the night, whereas WT mice showed the tendency of higher locomotor activity in ND condition (Fig. 24G)

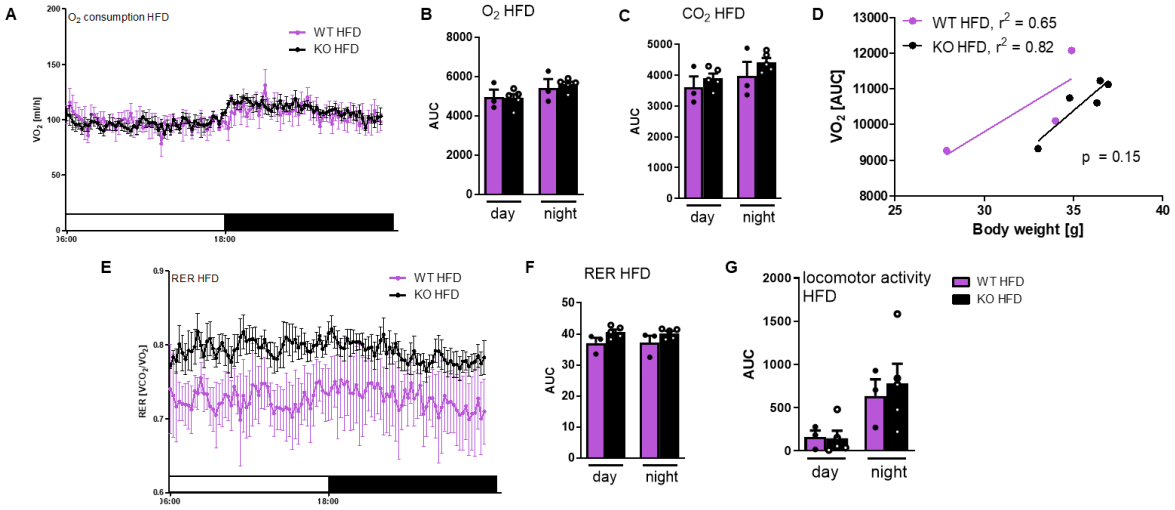

Fig. 25: Indirect calorimetry of *Ch25h* WT and KO mice after 12 weeks on HFD. Profile of **(A)** O_2 consumption and **(E)** RER during day and night; Area under the curve (AUC) for **(B)** O_2 consumption, **(C)** CO_2 production, **(F)** RER and **(G)** locomotor activity divided in day and night; **D** ANCOVA analysis of VO_2 (AUC) over 24 h in relation to body weight; n = 3 for WT mice on HFD, n = 5 for KO mice on HFD; AUC and One-way ANOVA with Bonferroni´s multiple comparisons tests; mean ± s.e.m.

No difference in O_2 consumption and CO_2 production was observed between WT and KO mice on HFD (Fig. 25A-C). There was also no significant difference in EE after correlation of O_2 consumption to body weight (Fig. 25D).

KO mice on HFD showed a tendency of increased RER compared to WT mice, albeit not significantly (Fig. 25E/F).

No difference was detectable for locomotor activity between WT and KO mice in HFD condition (Fig. 25G).

3.4.3.3 Analysis of body and tissue composition of *Ch25h* WT and KO mice in diet-induced obesity

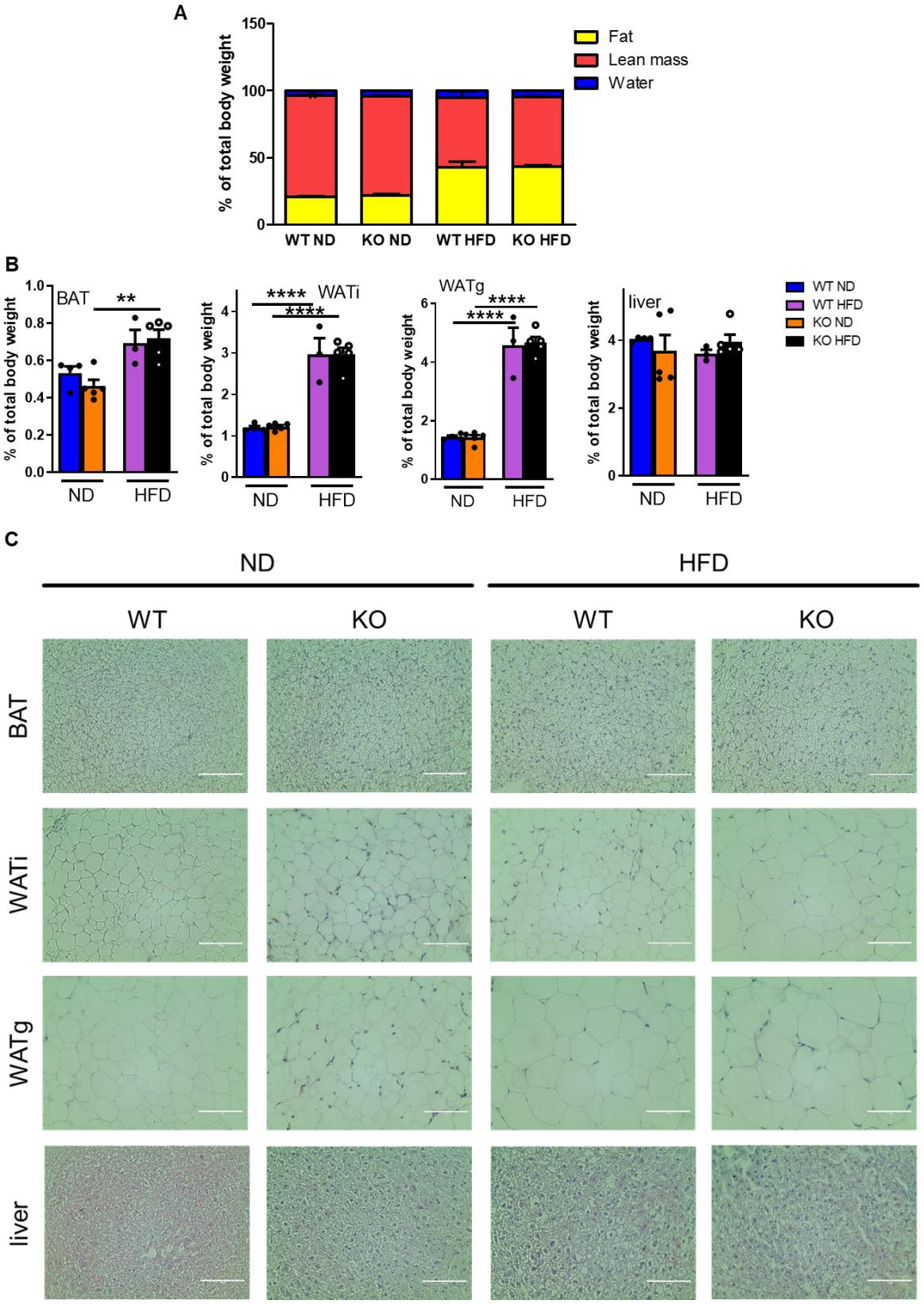

Fig. 26 (page 73): Analysis of body and tissue composition of *Ch25h* WT/KO mice on ND/HFD. A body composition (fat, water and lean mass) of WT/KO mice on ND and HFD as proportion of total body weight; **B** tissue weights of BAT, WATi, WATg and liver of WT/KO mice as proportion of total body weight; **C** HE staining of BAT (up), WATi and WATg (middle) and liver (down) from *Ch25h* WT and KO mice on ND (left) and HFD (right). Scale bar: 100 µm; n = 3 for WT mice on HFD, n = 4 for WT mice on ND, n = 5 for KO mice on ND and HFD; One-way ANOVA with Bonferroni´s multiple comparisons tests; **p < 0.01, ****p < 0.0001; mean ± s.e.m.

After indirect calorimetry, body composition was analysed using NMR minispec analyser. No difference was observed in the body composition of WT and KO mice in both ND and HFD condition (Fig. 26A).

Next, mice were sacrificed and organ weights were recorded. In agreement with the NMR data, no difference was observed in BAT, WATi, WATg and liver mass between genotypes (Fig. 26B).

Next, histological analysis was performed to study AT morphology in detail. HE stainings revealed no differences between WT and KO in BAT when mice were fed a ND or HFD. In HFD condition, adipocytes of KO mice in WATi were increased in size. Interestingly, in WATi and WATg of KO mice, more crown-like structures as morphologic correlate of browning could be observed independent of ND or HFD. In addition, more hepatic lipid accumulation was detected in HFD condition compared to ND condition indicating the development of hepatic steatosis in HFD (Fig. 26C).

3.4.3.4 Analysis of UCP1 expression of *Ch25h* WT and KO mice in diet-induced obesity

Finally, *Ucp1* expression was analysed in BAT via RT-qPCR. *Ucp1* tended to be higher in KO mice compared to WT mice especially in ND condition, albeit not significantly (Fig. 27A). Histologically, the higher amount of UCP1 in ND KO mice was detectable in UCP1 DAB staining. Especially in WATi, DAB colouring was more intense in ND KO compared to ND WT condition. In HFD, no difference in DAB intensity was observed between WT and KO mice (Fig. 27B).

Taken together, these data show that the higher EE in KO mice is due to higher UCP1 expression BAT and a browning process in WAT.

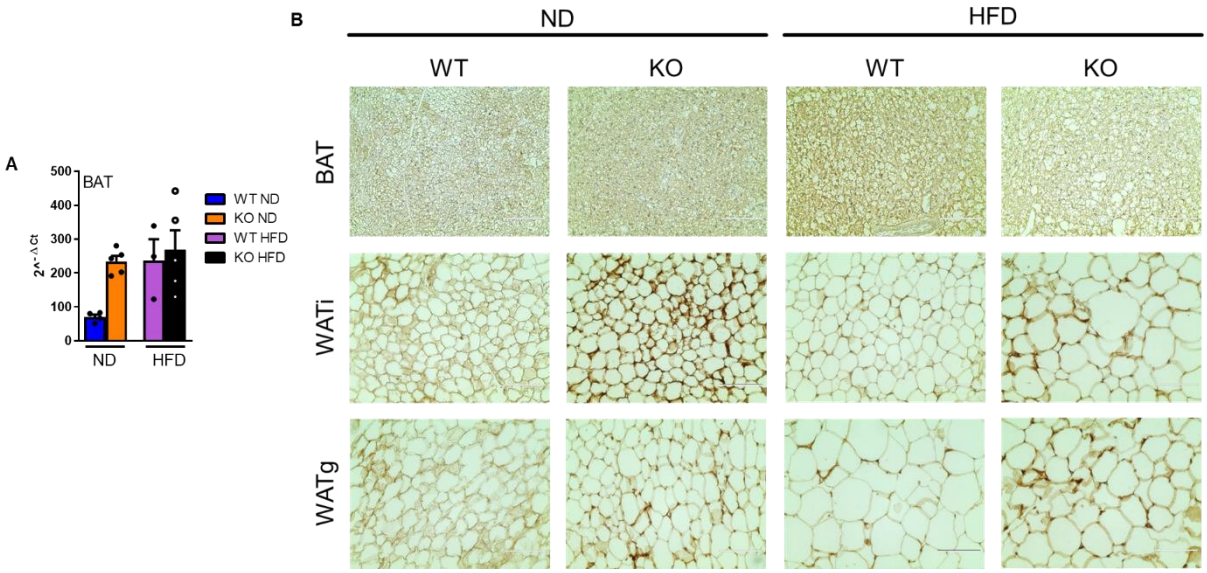

Fig. 27: Analysis of UCP1 expression in *Ch25h* WT and KO mice after 12 weeks on ND/HFD. A *Ucp1* mRNA expression in BAT of WT/KO mice on ND/HFD; **B** UCP1 DAB staining of BAT (up), WATi (middle) and WATg (down) from *Ch25h* WT and KO mice on ND (left) and HFD (right). Scale bar: 100 µm; n = 3 for WT mice on HFD, n = 4 for WT mice on ND, n = 5 for KO mice on ND and HFD; One-way ANOVA with Bonferroni´s multiple comparisons tests; mean ± s.e.m.

4. Discussion

4.1 Which cells produce 7α,25-OHC in adipose tissue?

Oxysterols are known to be involved in an abundance of physiological processes stretching from bile acid synthesis to oncogenesis and immunity (Griffiths et al., 2016). In this work I focussed on the oxysterol 7α,25-OHC which is known to play a crucial role e.g. in the positioning of B cells (Gatto et al., 2009; Pereira et al., 2009) and signals via the G_i-coupled GPCR EBI2 (Hannedouche et al., 2011; Liu et al., 2011). The previous work of our institute showed that 7α,25-OHC was also present in AT and regulated lipolytic activity in AT via EBI2 (Copperi et al., 2022). However, the cellular source of 7α,25-OHC in AT has not been detected yet and was further investigated with RT-qPCR analyses of AT fractions and co-cultivation studies.

RT-qPCR analyses of adipocytes and SVF revealed that *Ch25h*, *Cyp7b1* and *Ebi2* were higher expressed in the SVF in all AT compared to the adipocyte fraction (Fig. 11) indicating that 7α,25-OHC might be predominantly produced by non-adipocyte cells. Indeed, several studies identified various cell types capable of 7α,25-OHC production. Resident cells such as lymphoid stromal cells in spleen (Yi et al., 2012), astrocytes (Rutkowska et al., 2016), endothelial cells (Li et al., 2017) and colonic fibroblastic stromal cells (Emgård et al., 2018; Raselli et al., 2019) were shown to be responsible for local 7α,25-OHC production. In addition, hematopoietic cells, i.e. macrophages, were found to be an important 7α,25-OHC source especially upon activation of the immune system as LPS stimulation induced *Ch25h* and *Cyp7b1* expression and resulted in increased 7α,25-OHC levels (Bauman et al., 2009; Diczfalusy et al., 2009; Preuss et al., 2014). In this context, adipose tissue macrophages (ATM) are of special interest due to their role in AT inflammation in states of obesity (Weisberg et al., 2003). In support of this hypothesis, Russo et al. (2020) reported significantly higher levels of *Ch25h* in the SVF of human omental fat. Based on immunohistochemical stainings and flow cytometry analysis, the group identified resident ATM in murine WAT to be the main source of CH25H and therefore also of 25-OHC and 7α,25-OHC.

Levels of the 7α,25-OHC degrading enzyme HSD3B7 tended to be higher in the adipocyte fraction compared to the SVF (Fig. 11) indicating that 7α,25-OHC might be produced in the SVF and then gets degraded by adipocytes. The involvement of multiple cell types within a tissue (i.e. SVF and adipocytes) in the production and degradation of 7α,25-OHC was already shown in other tissues: indeed, Emgård et al. (2018) demonstrated that different types of colonic stromal cells are responsible for synthesis and degradation of 7α,25-OHC.

In BAT, a tendency towards higher *Ch25h* and *Cyp7b1* expression was observed in the SVF (Fig 11A). To study the potential influence of specific cell types in SVF on brown adipocytes, co-cultivation studies were performed. BMDM, NIH-3T3 fibroblasts and T17b endothelial cell progenitor cells were chosen for co-cultivation studies as they comprise the main cell types of the SVF fraction. Since *Ch25h* expression was already documented in these cells (Li et al., 2017; Emgård et al., 2018; Raselli et al., 2019), a potential role in 7α,25-OHC production in AT could be hypothesised. The experiments showed higher lipolytic rates of BA after co-cultivation with M_{LPS} (Fig. 12), whereas lipolysis was decreased after co-cultivation with endothelial cells and fibroblasts (Fig. 13). Further experiments e.g. with *Ch25h* KO BA or a specific EBI2-inhibitor need to reveal whether this effect is accountable to the 7α,25-OHC/EBI2 axis.

In conclusion, in conjunction with the RT-qPCR data and the findings of Russo et al. (2020), it is most favourable to assume an ATM-centred 7α,25-OHC production in WAT, whereas the identification of the 7α,25-OHC producing cells in BAT requires further studies. In this context it also needs to be considered, that macrophages are enriched in obese BAT, but to a lesser extent than in obese WAT (Fitzgibbons et al., 2011).

4.2 Are more enzymes involved in 7α,25-OHC synthesis in adipose tissue?

Oxysterol concentrations were measured in *Ch25h* KO mice to assess the effect of *Ch25h* deficiency on oxysterol metabolism and especially on 7α,25-OHC levels. Unexpectedly, no difference was observed in 7α,25-OHC levels between *Ch25h* WT and KO mice (Fig. 14/15). Either this may be attributable to an incorrect measurement or compensatory synthesising pathways might be involved.

It is known from previous studies that *Ch25h* KO resulted in significantly decreased levels of 7α,25-OHC in lymphatic (Yi et al., 2012) and gastrointestinal (Wyss et al., 2019) tissues but did not cause complete inhibition of 7α,25-OHC synthesis. In bone marrow chimera experiments, Yi et al. (2012) demonstrated that *Ch25h* KO mice reconstituted with WT bone marrow produced ~80 % less 7α,25-OHC in spleen in comparison to littermate control mice indicating that 7α,25-OHC production was clearly reduced, but not completely inhibited. Similar results could be obtained by Hannedouche et al. (2011). The authors, however, hypothesised that other enzymes than CH25H can contribute to 7α,25-OHC synthesis, even though to a lesser extent.

To date, only one further study investigated the effect of *Ch25h* deficiency on 7α,25-OHC levels in AT. Using LC-MS method, Russo et al. (2020) measured 7α,25-OHC and 25-OHC levels in WAT of ND and HFD *Ch25h* KO mice. Despite the difference in age (21 weeks old ND-fed mice in Russo`s studies vs. 8 weeks old mice in my experiments) Russo et al. made similar observations of substantially lower 25-OHC levels and unchanged 7α,25-OHC levels in WAT of ND *Ch25h* KO mice. In addition, Russo et al. (2020) measured significantly lower levels of 7α,25-OHC in HFD KO mice compared to WT mice.

Taking everything into account, it is most favourable to hypothesise a compensatory mechanism for 7α,25-OHC synthesis in *Ch25h* KO mice in AT. Possibly, those compensatory mechanisms are well established in AT, thus leading to unchanged 7α,25-OHC levels. In support of this hypothesis, further enzymes are known to be involved in 7α,25-OHC synthesis including CYP3A, CYP7A1 and especially CYP27A1 (Honda et al., 2011; Lund et al., 1993). Interestingly, the CYP27A1 substrates 7-OHC and 7-ketocholesterol showed a tendency towards lower levels in AT of *Ch25h* KO mice whereas the CYP27A1 product 27-OHC was significantly higher in BAT of *Ch25h* KO mice (Fig. 15), possibly indicating a higher turnover by CYP27A1. Consistently, transgenic CYP27A1-overexpressing mice were shown to have significantly higher levels of 25-OHC in brain compared to WT mice, an observation that was attributed to the 25-hydroxylation activity of CYP27A1 (Ali et al., 2013). However, in this study the 7α,25-OHC level was not measured. Conversely, another study using *Cyp27a1* KO mice observed significantly lower 7α,25-OHC plasma levels in *Cyp27a1* KO mice compared to WT mice (Griffiths et al., 2019). For

further studies, it would therefore be of great interest to examine the expression of those enzymes in BAT.

Furthermore, non-enzymatic synthesis via autoxidation by ROS (Bergstrom et al., 1941; Iuliano, 2011) is unlikely to play a role in compensatory 7α,25-OHC synthesis, as the mainly ROS-dependent synthesised oxysterols 5α,6α-epoxycholesterol and 5β,6β-epoxycholesterol (Schroepfer, 2000) were unchanged or lower in *Ch25h* KO mice compared to WT mice (Fig. 15). Vice versa, our group could show that 7α,25-OHC does not increase ROS-production but is able to increase NE-induced ROS-production (Copperi et al., 2022).

Apart from compensatory upregulation of other oxysterol synthesising enzymes, the 7α,25-OHC degrading enzyme HSD3B7 might be downregulated to keep 7α,25-OHC levels unchanged. Indeed, 7α-OHCnone is known to be a HSD3B7 mediated degradation product of 7-OHC (Russell, 2000) and showed similarly to its precursor significantly decreased levels in *Ch25h* KO mice. This might indicate a lower turnover by HSD3B7 resulting in unchanged levels of 7α,25-OHC.

Taken together, 7α,25-OHC synthesis in AT seems to depict a delicately regulated system of various involved enzymes.

4.3 Which effect has *Ch25h* deficiency *in vivo*?

The effect of *Ch25h* deficiency *in vivo* was initially investigated in standard housing conditions, i.e. 23 °C and *ad libitum* chow diet. *Ch25h* KO mice showed a tendency towards less O_2 consumption compared to WT mice indicating lower EE (Fig. 16). EE consists of several components including basal metabolism, the thermic effect of food, energy spent on thermoregulation and physical activity (Speakman, 2013).

Taken all these involved factors into account, less locomotor activity might partly explain the tendency towards lower EE in *Ch25h* KO mice. No substantial differences could be observed for the other factors: ANCOVA analysis and RER identified the same energy source for basal whole-body metabolism independent of body weight (Fig. 16) and unchanged UCP1 content in *Ch25h* KO mice (Fig. 18) indicates similar thermoregulatory mechanisms.

Next, *ex vivo* lipolysis was performed to compare lipolytic capacities of 8 weeks old *Ch25h* WT and KO mice. Lipolytic capacity tended to be higher in KO tissue compared to WT mice (Fig. 19). This observation was most distinctive in BAT and diminished in WATg indicating that CH25H and 7α,25-OHC play a particular role in AT with browning capacity. In correspondence with these findings, the treatment of AT explants with 7α,25-OHC resulted in significantly reduced NE-stimulated lipolysis especially in BAT and WATi, whereas no significant effect was observed in WATg (Copperi et al., 2022). As G_i-coupled receptors are known to influence lipolysis in an inhibitory manner (Moreno et al., 1983) *Ch25h* deficient mice might perform more lipolysis because the EBI2-mediated inhibitory effect of 7α,25-OHC was missing. The possible underlying molecular mechanisms resulting in that phenotype were already investigated by Copperi et al. (2022), as the inhibitory effect of 7α,25-OHC on energy expenditure was most evident under simultaneous administration of NE indicating an NE-mediated effect. However, Nielsen et al. (2014) described an abundance of molecules and signalling pathways involved in the regulation of lipolysis, e.g. β-adrenergic receptors, PKA, cAMP, HSL and UCP1 in BAT. Whether other signalling pathways apart from NE-mediated lipolysis are affected in *Ch25h* KO mice needs to be further investigated in subsequent studies.

Unexpectedly, the oxysterol measurements in 8 weeks old *Ch25h* WT and KO mice on 23 °C revealed that 7α,25-OHC levels were unaffected in KO mice (Fig. 15). Therefore, it needs to be further elucidated whether the effects in both indirect calorimetry and *ex vivo* lipolysis can really be attributed to the lack of 7α,25-OHC. Either the effects were not mediated via the 7α,25-OHC/EBI2 axis or the effects were caused by the up- or downregulation of another oxysterol. Currently, no other studies about the effect of *Ch25h* deficiency on EE and lipolysis are available, thus rendering the analysis of underlying mechanisms imperative.

4.4 Is CH25H a brake in cold-induced NST?

Prolonged cold exposure is known to induce WATi browning, a process by which white adipocytes gain a BA-like character due to an increased number of mitochondria and UCP1 (Lo et al., 2013). To study the effect of *Ch25h* deficiency on WATi browning and EE, *Ch25h* WT and KO mice were exposed to 4 °C for 1 week.

Ch25h KO mice had a significantly higher EE especially during the night. ANCOVA analysis and similar RER identified the same energy source for basal whole-body metabolism independent of body weight. On top, there was no difference in locomotor activity (Fig. 20).

Regarding possible differences in thermoregulatory mechanisms, UCP1 expression tended to be higher in all AT depots in *Ch25h* KO mice compared to WT mice (Fig. 22). In addition, KO mice had significantly more BAT mass and showed the same tendency in WAT depots (Fig. 21). It is known from previous studies that cold exposure exerts a trophic effect especially on BAT. Increased noradrenergic signalling during cold exposure promotes BA proliferation and differentiation by increased mitotic rates of endothelial cells, AT interstitial cells and preadipocytes as well as mitochondriogenesis. This results in increased BAT mass (Bukowiecki et al., 1982; Géloën et al., 1988; Néchad et al., 1987). This process strongly associates with cAMP-mediated upregulation of UCP1 resulting in higher thermogenic capacities (Cannon et al., 2004). Therefore, the tendency towards higher UCP1 levels in *Ch25h* KO mice together with the significantly higher BAT mass point to more NE-mediated NST in KO mice. Accordingly, WAT depots might show the tendency towards higher masses and more UCP1 content due to a stronger NE-mediated browning effect in *Ch25h* KO mice which was also shown to associate with higher UCP1 levels and thermogenic capacities (Peres Valgas da Silva et al., 2019). However, it needs to be considered that beige AT depots reach only about 10% of EE of classical brown AT (Nedergaard et al., 2013). In this context, one could hypothesise that *Ch25h* KO mice are able to perform lipolysis and NST better than WT mice because 7α,25-OHC misses as an inhibitor of lipolysis and the NE/cAMP signalling pathway is influenced in a stimulating manner. Taken together, this experiment established the evidence that *Ch25h* deficient mice can undergo WATi browning and endure chronic cold exposure better than WT mice.

4.5 Does CH25H promote the development of diabetes?

Ongoing studies in normal-weighted and obese humans promoted our understanding of oxysterol metabolism in pathophysiological conditions and especially in MetS, a symptom complex that is mainly characterised by abdominal obesity, arterial hypertension, hyperlipidemia and insulin resistance. 7-ketocholesterol, 25-OHC, 27-OHC and 7β-OHC were the most increased oxysterols whereas 4β-OHC decreased in MetS (Guillemot-Legris et al., 2016b; Murakami et al., 2000; Tremblay-Franco et al., 2015). In this way these oxysterols might promote inflammatory processes and leukocyte migration leading to MetS related morbidities such as cardiovascular disease and atherosclerosis. Indeed, 25-OHC and 27-OHC were found to be increased in atherosclerotic plaques and lesions (Virginio et al., 2015). Therefore, investigating the role of the 7α,25-OHC/EBI2 axis in obesity might depict a new promising approach in the therapy of MetS and obesity-related diseases.

First, the expression analysis of enzymes involved in 7α,25-OHC metabolism in ND and HFD revealed an upregulation of 7α,25-OHC producing enzymes in HFD, whereas HSD3B7 as degrading enzyme did not show any change or even decreased in expression (Fig. 9). Accordingly, the absolute level of 7α,25-OHC increased. On top, mRNA expression of *Ebi2* as receptor of 7α,25-OHC was also upregulated (Fig. 9), thus suggesting an EBI2 mediated role of 7α,25-OHC in diet induced obesity. In fact, Russo et al. (2020) also found significantly higher *Ch25h* expression and significantly increased 7α,25-OHC levels in HFD WAT compared to ND WAT.

The crucial role of 7α,25-OHC/EBI2 in obesity was then better characterised in experiments with *Ch25h* KO mice on HFD. Interestingly, *Ch25h* KO mice were healthier in terms of glucose metabolism and insulin signalling especially on HFD as GTT showed better glucose homeostasis in contrast to *Ch25h* WT mice (Fig. 23). This was particularly remarkable because *Ch25h* KO mice on HFD were even heavier and more obese than WT mice in the control group (Fig. 23). Russo et al. (2020) performed the same HFD and GTT experiments with *Ch25h* KO mice and observed the same effects. Additionally, the group also performed insulin tolerance test which revealed significantly lower blood glucose levels after insulin injection in HFD fed *Ch25h* KO mice indicating higher insulin sensitivity. This was confirmed by significantly lower basal insulin levels in HFD fed *Ch25h* KO mice. Based on the analysis of inflammatory markers in obese *Ch25h* WT and KO mice they

argued that CH25H contributes to AT inflammation in a proinflammatory manner and therefore promotes insulin resistance and the development T2DM. My observation of more obese but metabolically healthier *Ch25h* KO mice can possibly be explained in coherence with Russo et al's hypothesis, namely that *Ch25h* KO mice could store more triglycerides in AT as AT function was not or less impaired by inflammation and metaflammation. Indeed, Russo et al. (2020) noticed significantly heavier WATg depots in HFD fed *Ch25h* KO mice though I did not observe any differences in organ weights.

Although no common definition for metabolically healthy obesity is available, this term was coined due to the observation that certain obese individuals do not display obesity-related comorbidities as hypertension, T2DM and cardiometabolic diseases. The mechanisms leading to the distinction between metabolically healthy and unhealthy obesity are still unclear but lifestyle factors, AT biology, genetic predisposition, the gut microbiome and inflammatory processes are discussed to be involved in a multifactorial genesis (Smith et al., 2019). In this context, CH25H impairs metabolic health in obese conditions as *Ch25h* KO was demonstrated to improve insulin sensitivity (Russo et al., 2020; own data). In the analysis of *Ch25h* expression in diabetic and non-diabetic obese male humans, diabetic subjects had significantly higher levels compared to non-diabetic subjects, whereas *Ch25h* levels were similar between non-diabetic obese and lean individuals (Russo et al., 2020). However, CH25H dependent products as 25-OHC and 7α,25-OHC were only slightly higher in diabetic obese individuals.

Apart from the improved insulin sensitivity, *Ch25h* KO mice on HFD did not have any significant differences in EE, RER, UCP1 content and tissue morphology compared to WT mice (Fig. 25/26/27). In contrast, *Ch25h* KO mice on ND had a lower EE (Fig. 24) which can be explained by a significantly lower body weight, but they also had a higher RER and increased UCP1 content in BAT and WAT compared to WT control mice (Fig. 27). Differences in tissue morphology could be detected in terms of more crown-like structures in KO tissues usually indicating more local inflammation (Fig. 26).
The higher the RER, the higher the amount of carbohydrates used as energy source in whole body metabolism. More biomolecular investigations are needed to further elucidate that phenotype, but one possible explanation involves adrenergic signalling. On the one

hand, cAMP, which on its part increases upon noradrenergic stimulation, is a potent activator of UCP1 expression (Chen et al., 2013). On the other hand, epinephrine and NE are known to increase blood glucose level, foster glucose uptake in adipocytes and elevate the basal metabolic rate by increasing carbohydrate oxidation (Leboeuf et al., 1959; Ratheiser et al., 1998; Sherwin et al., 1980). It will be interesting to determine whether *Ch25h* KO mice on ND have altered catecholamine levels or adrenergic signalling and how the observed phenotype is related to *Ch25h* deficiency and the tissue morphology.

On top, it is interesting to compare the different results of *Ch25h* WT and KO mice under standard housing conditions (Fig. 16) and after 12 weeks of ND (Fig. 24). The mice of both experimental groups differ in the obtained food (standard vs. ND food) and the age (8 vs. 20 weeks) when analyses were performed. Therefore, the altered metabolic profile of *Ch25h* KO mice on ND could also be related to a long-term effect of a special diet and the age-related changes of whole-body metabolism. This enhances the need to further analyse the underlying molecular mechanisms leading to that phenotype.

4.6 CH25H as a potential drug target?

To date, several specific EBI2-targeting molecules have already been developed: NIBR189 (developed by Gessier et al., 2014) is the most used EBI2-antagonist to study pathophysiological process in autoimmune diseases, whereas GSK682753A (developed by Benned-Jensen et al., 2011) was designed as an inverse EBI2-agonist especially for *in vitro* receptor characterization studies. As Braden et al. (2020) showed that NIBR189 is unable to inhibit 7α,25-OHC-mediated calcium mobilisation, the group screened for further EBI2-specific antagonists and found the three molecules SAE-1, SAE-10 and SAE-14, which also reliably block calcium signalling. These molecules were already used *in vivo* to investigate the role of the 7α,25-OHC/EBI2-axis in neuropathic pain (Braden et al., 2020). However, all molecules were only used in animal experiments and no translation to human *in vivo* studies was forced yet. Also, currently there is no specific CH25H inhibitor available.

My investigations reinforce the need to search for CH25H inhibitors, as the data points to a crucial role of CH25H in physiological conditions and in the pathogenesis of AT-related

diseases. I could show that *Ch25h* deficient mice performed better during cold exposure and had better glucose homeostasis after HFD. It will be mandatory to elucidate whether the effects I observed are due to the lack of 7α,25-OHC or whether other oxysterols such as 25-OHC, which is the direct product of CH25H and the 7α,25-OHC precursor, or 27-OHC, which is upregulated in *Ch25h* KO mice, and their synthesising enzymes such as CYP27A1 need to be considered. Further analyses need to investigate levels of those oxysterols in diet induced obesity and cold-induced WAT browning. The data provided by this investigation suggest that CH25H plays an important role in regulating AT metabolism, stretching from obesity induced T2DM to cold induced EE, and thus point at CH25H and its products as possible targets in the treatment of metabolic disorders.

5. Summary

Obesity associates with comorbidities as hypertension, cardiovascular disease, metabolic syndrome and type 2 diabetes mellitus and therefore depicts an emerging health issue. On a molecular level, obesity is accompanied by a chronic inflammation of adipose tissue resulting from invading immune cells and local cytokine production leading to the mentioned systemic immunometabolic disorders.

7α,25-dihydroxycholesterol is a bioactive oxysterol mainly synthesised enzymatically via the enzymes CH25H and CYP7B1, is degraded by the enzyme HSD3B7 and is a potent activator of EBI2 – an inhibitory G-protein-coupled receptor predominantly involved in immune regulation. Our preliminary findings showed that 7α,25-dihydroxychoelsterol can be produced in adipose tissue and influences adipose tissue metabolism, but its source in adipose tissue is unclear.

Based on Polymerase Chain Reaction data from CH25H, CYP7B1 and HSD3B7 in adipose tissue fractions and co-cultivation experiments of brown adipocytes with macrophages, endothelial cells and fibroblasts, I propose in conjunction with findings of other groups that 7α,25-dihydroxycholesterol is mainly produced by macrophages in adipose tissues.

The functional role of CH25H was studied in a genetic *Ch25h* knock out mouse model. Initially, oxysterol levels were measured spectrometrically in serum, liver and adipose tissues of *Ch25h* wild type and knock out mice. There was no difference in 7α,25-dihydroxycholesterol levels between wild type and knock out mice but due to an altered expression pattern of other oxysterols there might be a compensatory mechanism for 7α,25-dihydroxycholesterol production in adipose tissue.

Functionally, *Ch25h* knock out mice in standard housing conditions had higher lipolytic capacities especially in brown adipose tissue in *ex vivo* lipolysis. Furthermore, after one week of chronic cold exposure at 4 °C, *Ch25h* knock out mice had higher energy expenditure and significantly more brown adipose tissue mass compared to wild type mice. Based on these findings I hypothesise that *Ch25h* knock out mice are enabled to perform lipolysis and non-shivering thermogenesis better than wild type mice because 7α,25-dihydroxycholesterol as an inhibitor of lipolysis is missing.

To study the effect of *Ch25h* deficiency in obesity, *Ch25h* wild type and knock out mice were fed with normal diet and high fat diet for 12 weeks. I could demonstrate that *Ch25h* knock out mice have higher energy expenditure with more expression of Uncoupling Protein 1 in normal diet and significantly better glucose homeostasis in Glucose Tolerance Test indicating that lack of CH25H ameliorates obesity-related comorbidities.

The data provided by this thesis suggest that CH25H plays an important role in the metabolic regulation of adipose tissue in physiological as well as in pathophysiological conditions, thus rendering CH25H and its products an interesting target in the treatment of metabolic disorders.

6. List of figures

7. List of tables

8. References

Aherne W, Hull D. Brown adipose tissue and heat production in the new born infant. J Pathol Bacteriol 1966; 91: 223-234

Ahima RS. Adipose tissue as an endocrine organ. Obesity (Silver Spring) 2006; 5: 242-249

Alasbahi RH, Melzig MF. Forskolin and derivatives as tools for studying the role of cAMP. Pharmazie 2012; 67: 5-13

Ali Z, Heverin M, Olin M, Acimovic J, Lövgren-Sandblom A, Shafaati M, Båvner A, Meiner V, Leitersdorf E, Björkhem I. On the regulatory role of side-chain hydroxylated oxysterols in the brain. Lessons from CYP27A1 transgenic and Cyp27a1$^{-/-}$ mice. J Lipid Res 2013; 54: 1033-1043

Barbatelli G, Murano I, Madsen L, Hao Q, Jimenez M, Kristiansen K, Giacobino JP, De Matteis R, Cinti S. The emergence of cold-induced brown adipocytes in mouse white fat depots is determined predominantly by white to brown adipocyte transdifferentiation. Am J Physiol Endocrinol Metab 2010; 298: 1244-1253

Barbe P, Millet L, Galitzky J, Lafontan M, Berlan M. In situ assessment of the role of the beta 1-, beta 2- and beta 3-adrenoceptors in the control of lipolysis and nutritive blood flow in human subcutaneous adipose tissue. Br J Pharmacol 1996; 117: 907-913

Bartness TJ, Bamshad M. Innervation of mammalian white adipose tissue: implications for the regulation of total body fat. Am J Physiol 1998; 275: 1399-1411

Bauman DR, Bitmansour AD, McDonald JG, Thompson BM, Liang G, Russell DW. 25-Hydroxycholesterol secreted by macrophages in response to Toll-like receptor activation suppresses immunoglobulin A production. Proc Natl Acad Sci U S A 2009; 106: 16794-16799

Benned-Jensen T, Smethurst C, Holst PJ, Page KR, Sauls H, Sivertsen B, Schwartz TW, Blanchard A, Jepras R, Rosenkilde MM. Ligand modulation of the Epstein-Barr virus-induced seven-transmembrane receptor EBI2: identification of a potent and efficacious inverse agonist. J Biol Chem 2011; 286: 29292-29302

Bergstrom S, Wintersteiner O. Autoxidation of sterols in colloidal aqueous solution: The nature of the products formed from cholesterol. J Biol Chem 1941; 141: 597-610

Bertholet AM, Chouchani ET, Kazak L, Angelin A, Fedorenko A, Long JZ, Vidoni S, Garrity R, Cho J, Terada N, Wallace DC, Spiegelman BM, Kirichok Y. H+ transport is an integral function of the mitochondrial ADP/ATP carrier. Nature 2019 571: 515-520

Birkenbach M, Josefsen K, Yalamanchili R, Lenoir G, Kieff E. Epstein-Barr virus-induced genes: first lymphocyte-specific G protein-coupled peptide receptors. J Virol 1993; 67: 2209-2220

Blanc M, Hsieh WY, Robertson KA, Kropp KA, Forster T, Shui G, Lacaze P, Watterson S, Griffiths SJ, Spann NJ, Meljon A, Talbot S, Krishnan K, Covey DF, Wenk MR, Craigon M, Ruzsics Z, Haas J, Angulo A, Griffiths WJ, Glass CK, Wang Y, Ghazal P. The transcription factor STAT-1 couples macrophage synthesis of 25-hydroxycholesterol to the interferon antiviral response. Immunity 2013; 38: 106-118

Blondin DP, Nielsen S, Kuipers EN, Severinsen MC, Jensen VH, Miard S, Jespersen NZ, Kooijman S, Boon MR, Fortin M, Phoenix S, Frisch F, Guérin B, Turcotte ÉE, Haman F, Richard D, Picard F, Rensen PCN, Scheele C, Carpentier AC. Human Brown Adipocyte Thermogenesis Is Driven by β_2-AR Stimulation. Cell Metab 2020; 32: 287-300

Braden K, Giancotti LA, Chen Z, DeLeon C, Latzo N, Boehn T, D'Cunha N, Thompson BM, Doyle TM, McDonald JG, Walker JK, Kolar GR, Arnatt CK, Salvemini D. GPR183-Oxysterol Axis in Spinal Cord Contributes to Neuropathic Pain. J Pharmacol Exp Ther 2020; 375: 367-375

Briscoe J, Thérond PP. The mechanisms of Hedgehog signalling and its roles in development and disease. Nat Rev Mol Cell Biol 2013; 14: 416-429

Bukowiecki L, Collet AJ, Follea N, Guay G, Jahjah L. Brown adipose tissue hyperplasia: a fundamental mechanism of adaptation to cold and hyperphagia. Am J Physiol 1982; 242: 353-359

Cannon B, Nedergaard J. Brown adipose tissue: function and physiological significance. Physiol Rev 2004; 84: 277-359

Cero C, Lea HJ, Zhu KY, Shamsi F, Tseng YH, Cypess AM. β_3-Adrenergic receptors regulate human brown/beige adipocyte lipolysis and thermogenesis. JCI Insight 2021; 6: 139160

Chen HY, Liu Q, Salter AM, Lomax MA. Synergism between cAMP and PPARγ Signalling in the Initiation of UCP1 Gene Expression in HIB1B Brown Adipocytes. PPAR Res 2013; 2013: 476049

Choi WS, Lee G, Song WH, Koh JT, Yang J, Kwak JS, Kim HE, Kim SK, Son YO, Nam H, Jin I, Park ZY, Kim J, Park IY, Hong JI, Kim HA, Chun CH, Ryu JH, Chun JS. The CH25H-CYP7B1-RORα axis of cholesterol metabolism regulates osteoarthritis. Nature 2019; 566: 254-258

Chusyd DE, Wang D, Huffman DM, Nagy TR. Relationships between Rodent White Adipose Fat Pads and Human White Adipose Fat Depots. Front Nutr 2016; 3:10

Cinti S. The adipose organ at a glance. Dis Model Mech 2012; 5: 588-594

Copperi F, Schleis I, Roumain M, Muccioli GG, Casola S, Klingenspor M, Pfeifer A, Gnad T. EBI2 is a negative modulator of brown adipose tissue energy expenditure in mice and human brown adipocytes. Commun Biol 2022; 29; 5:280

Cypess AM, Lehman S, Williams G, Tal I, Rodman D, Goldfine AB, Kuo FC, Palmer EL, Tseng YH, Kolodny GM, Kahn CR. Identification and importance of brown adipose tissue in adult humans. N Engl J Med 2009; 360: 1509-1517

Cypess AM, Chen YC, Sze C, Wang K, English J, Chan O, Holman AR, Tal I, Palmer MR, Kolodny GM, Kahn CR. Cold but not sympathomimetics activates human brown adipose tissue in vivo. Proc Natl Acad Sci U S A 2012; 109: 10001-10005

Cypess AM, Weiner LS, Roberts-Toler C, Franquet Elía E, Kessler SH, Kahn PA, English J, Chatman K, Trauger SA, Doria A, Kolodny GM. Activation of human brown adipose tissue by a β3-adrenergic receptor agonist. Cell Metab 2015; 21: 33-38

Dawkins MJR, Scopes JW. Non-shivering thermogenesis and brown adipose tissue in the human new-born infant. Nature 1965; 206: 201-202

Dehghan M, Akthar-Danesh N, Merchant AT. Childhood obesity, prevalence and prevention. Nutr J 2005; 4:24

Diczfalusy U, Olofsson KE, Carlsson AM, Gong M, Golenbock DT, Rooyackers O, Fläring U, Björkbacka H. Marked upregulation of cholesterol 25-hydroxylase expression by lipopolysaccharide. J Lipid Res 2009; 50: 2258-2264

Duc D, Vigne S, Pot C. Oxysterols in Autoimmunity. Int J Mol Sci 2019; 20: 4522

Dulos J, Verbraak E, Bagchus WM, Boots AM, Kaptein A. Severity of murine collagen-induced arthritis correlates with increased CYP7B activity: enhancement of dehydroepiandrosterone metabolism by interleukin-1beta. Arthritis Rheum 2004; 50: 3346-3353

Drubach LA, Palmer EL 3rd, Connolly LP, Baker A, Zurakowski D, Cypess AM. Pediatric brown adipose tissue: detection, epidemiology, and differences from adults. J Pediatr 2011; 159: 939-944

Duncan RE, Ahmadian M, Jaworski K, Sarkadi-Nagy E, Sul HS. Regulation of lipolysis in adipocytes. Annu Rev Nutr 2007; 27: 79-101

Dzeletovic S, Breuer O, Lund E, Diczfalusy U. Determination of cholesterol oxidation products in human plasma by isotope dilution-mass spectrometry. Anal Biochem 1995; 225: 73-80

Emgård J, Kammoun H, García-Cassani B, Chesné J, Parigi SM, Jacob JM, Cheng HW, Evren E, Das S, Czarnewski P, Sleiers N, Melo-Gonzalez F, Kvedaraite E, Svensson M, Scandella E, Hepworth MR, Huber S, Ludewig B, Peduto L, Villablanca EJ, Veiga-Fernandes H, Pereira JP, Flavell RA, Willinger T. Oxysterol Sensing through the Receptor GPR183 Promotes the Lymphoid-Tissue-Inducing Function of Innate Lymphoid Cells and Colonic Inflammation. Immunity 2018; 48: 120-132

Engin AB. What Is Lipotoxicity? Adv Exp Med Biol 2017; 960: 197-220

Fedorenko A, Lishko PV, Kirichok Y. Mechanism of fatty-acid-dependent UCP1 uncoupling in brown fat mitochondria. Cell 2012; 151: 400-413

Fitzgibbons TP, Kogan S, Aouadi M, Hendricks GM, Straubhaar J, Czech MP. Similarity of mouse perivascular and brown adipose tissues and their resistance to diet-induced inflammation. Am J Physiol Heart Circ Physiol. 2011; 301: 1425-1437

Frayn KN. Adipose tissue as a buffer for daily lipid flux. Diabetologia 2002; 45: 1201-1210

Gatto D, Paus D, Basten A, Mackay CR, Brink R. Guidance of B cells by the orphan G protein-coupled receptor EBI2 shapes humoral immune responses. Immunity 2009; 31: 259-269

Géloën A, Collet AJ, Guay G, Bukowiecki LJ. Beta-adrenergic stimulation of brown adipocyte proliferation. Am J Physiol 1988; 254: 175-182

Gessier F, Preuss I, Yin H, Rosenkilde MM, Laurent S, Endres R, Chen YA, Marsilje TH, Seuwen K, Nguyen DG, Sailer AW. Identification and characterization of small molecule modulators of the Epstein-Barr virus-induced gene 2 (EBI2) receptor. J Med Chem 2014; 57: 3358-3368

Gimbrone MA Jr, García-Cardeña G. Endothelial Cell Dysfunction and the Pathobiology of Atherosclerosis. Circ Res 2016; 118: 620-636

Gold ES, Diercks AH, Podolsky I, Podyminogin RL, Askovich PS, Treuting PM, Aderem A. 25-Hydroxycholesterol acts as an amplifier of inflammatory signaling. Proc Natl Acad Sci U S A 2014; 111: 10666-10671

Griffiths WJ, Wang Y. An update on oxysterol biochemistry: New discoveries in lipidomics. Biochem Biophys Res Commun 2018; 504: 617-622

Griffiths WJ, Wang Y. Oxysterol research: a brief review. Biochem Soc Trans 2019; 47: 517-526

Griffiths WJ, Abdel-Khalik J, Hearn T, Yutuc E, Morgan AH, Wang Y. Current trends in oxysterol research. Biochem Soc Trans 2016; 44: 652-658

Griffiths WJ, Crick PJ, Meljon A, Theofilopoulos S, Abdel-Khalik J, Yutuc E, Parker JE, Kelly DE, Kelly SL, Arenas E, Wang Y. Additional pathways of sterol metabolism: Evidence from analysis of Cyp27a1-/- mouse brain and plasma. Biochim Biophys Acta Mol Cell Biol Lipids 2019; 1864: 191-211

Guillemot-Legris O, Mutemberezi V, Cani PD, Muccioli GG. Obesity is associated with changes in oxysterol metabolism and levels in mice liver, hypothalamus, adipose tissue and plasma. Sci Rep 2016a; 6:19694

Guillemot-Legris O, Mutemberezi V, Muccioli GG. Oxysterols in Metabolic Syndrome: From Bystander Molecules to Bioactive Lipids. Trends Mol Med 2016b; 22: 594-614

Han S, Sun HM, Hwang KC, Kim SW. Adipose-Derived Stromal Vascular Fraction Cells: Update on Clinical Utility and Efficacy. Crit Rev Eukaryot Gene Expr 2015; 25: 145-152

Hannedouche S, Zhang J, Yi T, Shen W, Nguyen D, Pereira JP, Guerini D, Baumgarten BU, Roggo S, Wen B, Knochenmuss R, Noël S, Gessier F, Kelly LM, Vanek M, Laurent S, Preuss I, Miault C, Christen I, Karuna R, Li W, Koo DI, Suply T, Schmedt C, Peters EC, Falchetto R, Katopodis A, Spanka C, Roy MO, Detheux M, Chen YA, Schultz PG, Cho CY, Seuwen K, Cyster JG, Sailer AW. Oxysterols direct immune cell migration via EBI2. Nature 2011; 475: 524-527

Hardy OT, Czech MP, Corvera S. What causes the insulin resistance underlying obesity? Curr Opin Endocrinol Diabetes Obes 2012; 19: 81-87

Hatzopoulos AK, Folkman J, Vasile E, Eiselen GK, Rosenberg RD. Isolation and characterization of endothelial progenitor cells from mouse embryos. Development 1998; 125: 1457-1468

Honda A, Miyazaki T, Ikegami T, Iwamoto J, Maeda T, Hirayama T, Saito Y, Teramoto T, Matsuzaki Y. Cholesterol 25-hydroxylation activity of CYP3A. J Lipid Res 2011; 52: 1509-1516

Hotamisligil GS. Inflammation and metabolic disorders. Nature 2006; 444: 860-867

Hotamisligil GS. Inflammation, metaflammation and immunometabolic disorders. Nature 2017; 542: 177-185

Huh JY, Park YJ, Ham M, Kim JB. Crosstalk between adipocytes and immune cells in adipose tissue inflammation and metabolic dysregulation in obesity. Mol Cells 2014; 37: 365-371

Hulse KE, Norton JE, Suh L, Zhong Q, Mahdavinia M, Simon P, Kern RC, Conley DB, Chandra RK, Tan BK, Peters AT, Grammer LC 3rd, Harris KE, Carter RG, Kato A, Schleimer RP. Chronic rhinosinusitis with nasal polyps is characterized by B-cell inflammation and EBV-induced protein 2 expression. J Allergy Clin Immunol 2013; 131: 1075-1083

Iuliano L. Pathways of cholesterol oxidation via non-enzymatic mechanisms. Chem Phys Lipids 2011; 164: 457-468

Jordana M, Särnstrand B, Sime PJ, Ramis I. Immune-inflammatory functions of fibroblasts. Eur Respir J 1994; 7: 2212-2222

Kandutsch AA, Chen HW. Inhibition of sterol synthesis in cultured mouse cells by 7alpha-hydroxycholesterol, 7beta-hydroxycholesterol, and 7-ketocholesterol. J Biol Chem 1973; 248: 8408-8417

Kazak L, Chouchani ET, Jedrychowski MP, Erickson BK, Shinoda K, Cohen P, Vetrivelan R, Lu GZ, Laznik-Bogoslavski D, Hasenfuss SC, Kajimura S, Gygi SP, Spiegelman BM. A creatine-driven substrate cycle enhances energy expenditure and thermogenesis in beige fat. Cell 2015; 163: 643-655.

Leboeuf B, Flinn RB, Cahill GF Jr. Effect of epinephrine on glucose uptake and glycerol release by adipose tissue in vitro. Proc Soc Exp Biol Med 1959: 102:527-529

Li J, Daly E, Campioli E, Wabitsch M, Papadopoulos V. De novo synthesis of steroids and oxysterols in adipocytes. J Biol Chem 2014; 289: 747-764

Li Z, Martin M, Zhang J, Huang HY, Bai L, Zhang J, Kang J, He M, Li J, Maurya MR, Gupta S, Zhou G, Sangwung P, Xu YJ, Lei T, Huang HD, Jain M, Jain MK, Subramaniam S, Shyy JY. Krüppel-Like Factor 4 Regulation of Cholesterol-25-Hydroxylase and Liver X Receptor Mitigates Atherosclerosis Susceptibility. Circulation 2017; 136: 1315-1330

Liu C, Yang XV, Wu J, Kuei C, Mani NS, Zhang L, Yu J, Sutton SW, Qin N, Banie H, Karlsson L, Sun S, Lovenberg TW. Oxysterols direct B-cell migration through EBI2. Nature 2011; 475: 519-523

Lo KA, Sun L. Turning WAT into BAT: a review on regulators controlling the browning of white adipocytes. Biosci Rep 2013; 33: 00065

Lumeng CN, Bodzin JL, Saltiel AR. Obesity induces a phenotypic switch in adipose tissue macrophage polarization. J Clin Invest 2007; 117: 175-184

Lund E, Björkhem I, Furster C, Wikvall K. 24-, 25- and 27-hydroxylation of cholesterol by a purified preparation of 27-hydroxylase from pig liver. Biochim Biophys Acta 1993; 1166: 177-182

Luu-The V. Assessment of steroidogenesis and steroidogenic enzyme functions. J Steroid Biochem Mol Biol 2013; 137: 176-182

McDonald JG, Smith DD, Stiles AR, Russell DW. A comprehensive method for extraction and quantitative analysis of sterols and secosteroids from human plasma. J Lipid Res 2012; 53: 1399-1409

McDonald ME, Li C, Bian H, Smith BD, Layne MD, Farmer SR. Myocardin-related transcription factor A regulates conversion of progenitors to beige adipocytes. Cell 2015; 160: 105-118

Meffre D, Shackleford D, Hichor M, Gorgievski V, Tzavara ET, Trousson A, Ghoumari AM, Deboux C, Nait Oumesmar B, Liere P, Schumacher M, Baulieu EE, Charbonnier F, Grenier J, Massaad C. Liver X receptors alpha and beta promote myelination and remyelination in the cerebellum. Proc Natl Acad Sci U S A 2015; 112: 7587-7592

Mills EL, Pierce KA, Jedrychowski MP, Garrity R, Winther S, Vidoni S, Yoneshiro T, Spinelli JB, Lu GZ, Kazak L, Banks AS, Haigis MC, Kajimura S, Murphy MP, Gygi SP, Clish CB, Chouchani ET. Accumulation of succinate controls activation of adipose tissue thermogenesis. Nature 2018; 560: 102-106

Morello F, Saglio E, Noghero A, Schiavone D, Williams TA, Verhovez A, Bussolino F, Veglio F, Mulatero P. LXR-activating oxysterols induce the expression of inflammatory

markers in endothelial cells through LXR-independent mechanisms. Atherosclerosis 2009; 207: 38-44

Moreno FJ, Mills I, García-Sáinz JA, Fain JN. Effects of pertussis toxin treatment on the metabolism of rat adipocytes. J Biol Chem 1983; 258: 10938-10943

Murakami H, Tamasawa N, Matsui J, Yasujima M, Suda T. Plasma oxysterols and tocopherol in patients with diabetes mellitus and hyperlipidemia. Lipids 2000; 35: 333-338

Mutemberezi V, Masquelier J, Guillemot-Legris O, Muccioli GG. Development and validation of an HPLC-MS method for the simultaneous quantification of key oxysterols, endocannabinoids, and ceramides: variations in metabolic syndrome. Anal Bioanal Chem 2016a; 408: 733-745

Mutemberezi V, Guillemot-Legris O, Muccioli GG. Oxysterols: From cholesterol metabolites to key mediators. Prog Lipid Res 2016b; 64: 152-169

Myers BR, Sever N, Chong YC, Kim J, Belani JD, Rychnovsky S, Bazan JF, Beachy PA. Hedgehog pathway modulation by multiple lipid binding sites on the smoothened effector of signal response. Dev Cell 2013; 26: 346-357

NCD Risk Factor Collaboration (NCD-RisC). Worldwide trends in body-mass index, underweight, overweight, and obesity from 1975 to 2016: a pooled analysis of 2416 population-based measurement studies in 128·9 million children, adolescents, and adults. Lancet 2017; 390: 2627-2642

Néchad M. Structure and development of brown adipose tissue. In: Trayhurn P, Nicholls DG, eds., Brown Adipose Tissue. London: Edward Arnold, 1986: 1-30

Néchad M, Nedergaard J, Cannon B. Noradrenergic stimulation of mitochondriogenesis in brown adipocytes differentiating in culture. Am J Physiol 1987; 253: 889-894

Nedergaard J, Bengtsson T, Cannon B. Unexpected evidence for active brown adipose tissue in adult humans. Am J Physiol Endocrinol Metab 2007; 293: 444-452

Nedergaard J, Cannon B. UCP1 mRNA does not produce heat. Biochim Biophys Acta 2013; 1831: 943-949

Nelson ER, Wardell SE, McDonnell DP. The molecular mechanisms underlying the pharmacological actions of estrogens, SERMs and oxysterols: implications for the treatment and prevention of osteoporosis. Bone 2013; 53: 42-50

Nicholls DG, Locke RM. Thermogenic mechanisms in brown fat. Physiol Rev 1984; 64: 1-64

Nielsen TS, Jessen N, Jørgensen JO, Møller N, Lund S. Dissecting adipose tissue lipolysis: molecular regulation and implications for metabolic disease. J Mol Endocrinol 2014; 52: 199-222

Nishimura S, Manabe I, Nagasaki M, Eto K, Yamashita H, Ohsugi M, Otsu M, Hara K, Ueki K, Sugiura S, Yoshimura K, Kadowaki T, Nagai R. CD8+ effector T cells contribute to macrophage recruitment and adipose tissue inflammation in obesity. Nat Med 2009; 15: 914-920

Pereira JP, Kelly LM, Xu Y, Cyster JG. EBI2 mediates B cell segregation between the outer and centre follicle. Nature 2009; 460: 1122-1126

Peres Valgas da Silva C, Hernández-Saavedra D, White JD, Stanford KI. Cold and Exercise: Therapeutic Tools to Activate Brown Adipose Tissue and Combat Obesity. Biology (Basel) 2019; 8: 9

Pfeifer A, Hoffmann LS. Brown, beige, and white: the new color code of fat and Its pharmacological implications. Annu Rev Pharmacol Toxicol 2015; 55: 207–227

Preuss I, Ludwig MG, Baumgarten B, Bassilana F, Gessier F, Seuwen K, Sailer AW. Transcriptional regulation and functional characterization of the oxysterol/EBI2 system in primary human macrophages. Biochem Biophys Res Commun 2014; 446: 663-668

Raselli T, Wyss A, Gonzalez Alvarado MN, Weder B, Mamie C, Spalinger MR, Van Haaften WT, Dijkstra G, Sailer AW, Imenez Silva PH, Wagner CA, Tosevski V, Leibl S, Scharl M, Rogler G, Hausmann M, Misselwitz B. The Oxysterol Synthesising Enzyme CH25H Contributes to the Development of Intestinal Fibrosis. J Crohns Colitis 2019; 13: 1186-1200

Ratheiser KM, Brillon DJ, Campbell RG, Matthews DE. Epinephrine produces a prolonged elevation in metabolic rate in humans. Am J Clin Nutr 1998; 68: 1046-1052

Reboldi A, Dang EV, McDonald JG, Liang G, Russell DW, Cyster JG. Inflammation. 25-Hydroxycholesterol suppresses interleukin-1-driven inflammation downstream of type I interferon. Science 2014; 345: 679-684

Roh HC, Tsai LTY, Shao M, Tenen D, Shen Y, Kumari M, Lyubetskaya A, Jacobs C, Dawes B, Gupta RK, Rosen ED. Warming Induces Significant Reprogramming of Beige, but Not Brown, Adipocyte Cellular Identity. Cell Metab 2018; 27: 1121-1137

Ronti T, Lupattelli G, Mannarino E. The endocrine function of adipose tissue: an update. Clin Endocrinol 2006; 64: 355-365

Rosenkilde MM, Benned-Jensen T, Andersen H, Holst PJ, Kledal TN, Lüttichau HR, Larsen JK, Christensen JP, Schwartz TW. Molecular pharmacological phenotyping of EBI2. An orphan seven-transmembrane receptor with constitutive activity. J Biol Chem 2006; 281: 13199-13208

Russell DW. Oxysterol biosynthetic enzymes. Biochim Biophys Acta 2000; 1529: 126-135

Russo L, Muir L, Geletka L, Delproposto J, Baker N, Flesher C, O'Rourke R, Lumeng CN. Cholesterol 25-hydroxylase (CH25H) as a promoter of adipose tissue inflammation in obesity and diabetes. Mol Metab 2020; 39: 100983

Rutkowska A, O'Sullivan SA, Christen I, Zhang J, Sailer AW, Dev KK. The EBI2 signalling pathway plays a role in cellular crosstalk between astrocytes and macrophages. Sci Rep 2016; 6:25520

Saladin R, De Vos P, Guerre-Millo M, Leturque A, Girard J, Staels B, Auwerx J. Transient increase in obese gene expression after food intake or insulin administration. Nature 1995; 377: 527-529

Saponaro C, Gaggini M, Carli F, Gastaldelli A. The Subtle Balance between Lipolysis and Lipogenesis: A Critical Point in Metabolic Homeostasis. Nutrients 2015; 7: 9453-9474

Schroepfer GJ Jr. Oxysterols: modulators of cholesterol metabolism and other processes. Physiol Rev 2000; 80: 361-554

Schweizer S, Oeckl J, Klingenspor M, Fromme T. Substrate fluxes in brown adipocytes upon adrenergic stimulation and uncoupling protein 1 ablation. Life Sci Alliance 2018; 1: 201800136

Shao M, Wang QA, Song A, Vishvanath L, Busbuso NC, Scherer PE, Gupta RK. Cellular Origins of Beige Fat Cells Revisited. Diabetes 2019; 68: 1874-1885

Sherwin RS, Shamoon H, Hendler R, Saccà L, Eigler N, Walesky M. Epinephrine and the regulation of glucose metabolism: effect of diabetes and hormonal interactions. Metabolism 1980; 29: 1146-1154

Sidossis L, Kajimura S. Brown and beige fat in humans: thermogenic adipocytes that control energy and glucose homeostasis. J Clin Invest 2015; 125: 478-486

Smith GI, Mittendorfer B, Klein S. Metabolically healthy obesity: facts and fantasies. J Clin Invest 2019; 129: 3978-3989

Soroosh P, Wu J, Xue X, Song J, Sutton SW, Sablad M, Yu J, Nelen MI, Liu X, Castro G, Luna R, Crawford S, Banie H, Dandridge RA, Deng X, Bittner A, Kuei C, Tootoonchi M, Rozenkrants N, Herman K, Gao J, Yang XV, Sachen K, Ngo K, Fung-Leung WP, Nguyen S, de Leon-Tabaldo A, Blevitt J, Zhang Y, Cummings MD, Rao T, Mani NS, Liu C, McKinnon M, Milla ME, Fourie AM, Sun S. Oxysterols are agonist ligands of RORγt and drive Th17 cell differentiation. Proc Natl Acad Sci U S A 2014; 111: 12163-12168

Speakman JR. Measuring energy metabolism in the mouse - theoretical, practical, and analytical considerations. Front Physiol 2013; 4:34

Steppan CM, Bailey ST, Bhat S, Banerjee RR, Wright CM, Patel HR, Ahima RS, Lazar MA. The hormone resistin links obesity to diabetes. Nature 2001; 409: 307-312

Straat ME, Hoekx CA, van Velden FHP, Pereira Arias-Bouda LM, Dumont L, Blondin DP, Boon MR, Martinez-Pellez B, Rensen PCN. Stimulation of the beta-2-adrenergic receptor with salbutamol activates human brown adipose tissue. Cell Rep Med 2023; 4: 100942

Sun K, Kusminski CM, Scherer PM. Adipose tissue remodeling and obesity. J Clin Invest 2011; 121: 2094-2101

Sun S, Liu C. 7α,25-dihydroxycholesterol-mediated activation of EBI2 in immune regulation and diseases. Front Pharmacol 2015; 6:60

Tavernier G, Barbe P, Galitzky J, Berlan M, Caput D, Lafontan M, Langin D. Expression of beta3-adrenoceptors with low lipolytic action in human subcutaneous white adipocytes. J Lipid Res 1996; 37: 87-97

Theofilopoulos S, Wang Y, Kitambi SS, Sacchetti P, Sousa KM, Bodin K, Kirk J, Saltó C, Gustafsson M, Toledo EM, Karu K, Gustafsson JÅ, Steffensen KR, Ernfors P, Sjövall J, Griffiths WJ, Arenas E. Brain endogenous liver X receptor ligands selectively promote midbrain neurogenesis. Nat Chem Biol 2013; 9: 126-133

Todaro GJ, Green H. Quantitative studies of the growth of mouse embryo cells in culture and their development into established lines. J Cell Biol 1963; 17: 299-313

Tremblay-Franco M, Zerbinati C, Pacelli A, Palmaccio G, Lubrano C, Ducheix S, Guillou H, Iuliano L. Effect of obesity and metabolic syndrome on plasma oxysterols and fatty acids in human. Steroids 2015; 99: 287-292

Uhlén M, Fagerberg L, Hallström BM, Lindskog C, Oksvold P, Mardinoglu A, Sivertsson Å, Kampf C, Sjöstedt E, Asplund A, Olsson I, Edlund K, Lundberg E, Navani S, Szigyarto CA, Odeberg J, Djureinovic D, Takanen JO, Hober S, Alm T, Edqvist PH, Berling H, Tegel H, Mulder J, Rockberg J, Nilsson P, Schwenk JM, Hamsten M, von Feilitzen K, Forsberg M, Persson L, Johansson F, Zwahlen M, von Heijne G, Nielsen J, Pontén F. Proteomics. Tissue-based map of the human proteome. Science 2015, 347):1260419, Human Protein Atlas proteinatlas.org, for *Ch25h*: https://www.proteinatlas.org/ENSG00000138135-CH25H/tissue, for *Cyp7b1*: https://www.proteinatlas.org/ENSG00000172817-CYP7B1/tissue, for *Hsd3b7*: https://www.proteinatlas.org/ENSG00000099377-HSD3B7/tissue (last visited 26.10.2023)

Ukropec J, Anunciado RP, Ravussin Y, Hulver MW, Kozak LP. UCP1-independent thermogenesis in white adipose tissue of cold-acclimated Ucp1-/- mice. J Biol Chem 2006; 281: 31894-31908

van Marken Lichtenbelt WD, Vanhommerig JW, Smulders NM, Drossaerts JM, Kemerink GJ, Bouvy ND, Schrauwen P, Teule GJ. Cold-activated brown adipose tissue in healthy men. N Engl J Med 2009; 360: 1500-1508

Virginio VW, Nunes VS, Moura FA, Menezes FH, Andreollo NA, Rogerio F, Scherrer DZ, Quintão EC, Nakandakare E, Petrucci O, Nadruz-Junior W, de Faria EC, Sposito AC. Arterial tissue and plasma concentration of enzymatic-driven oxysterols are associated with severe peripheral atherosclerotic disease and systemic inflammatory activity. Free Radic Res 2015; 49:199-203

Virtanen KA, Lidell ME, Orava J, Heglind M, Westergren R, Niemi T, Taittonen M, Laine J, Savisto NJ, Enerbäck S, Nuutila P. Functional brown adipose tissue in healthy adults. N Engl J Med 2009; 360: 1518-1525. Erratum in: N Engl J Med; 361:1123

Virtue S, Vidal-Puig A. Adipose tissue expandability, lipotoxicity and the Metabolic Syndrome--an allostatic perspective. Biochim Biophys Acta 2010; 1801: 338-349

Wang W, Kissig M, Rajakumari S, Huang L, Lim HW, Won KJ, Seale P. Ebf2 is a selective marker of brown and beige adipogenic precursor cells. Proc Natl Acad Sci U S A 2014; 111: 14466-14471

Weisberg SP, McCann D, Desai M, Rosenbaum M, Leibel RL, Ferrante AW Jr. Obesity is associated with macrophage accumulation in adipose tissue. J Clin Invest 2003; 112: 1796-1808

Winer S, Chan Y, Paltser G, Truong D, Tsui H, Bahrami J, Dorfman R, Wang Y, Zielenski J, Mastronardi F, Maezawa Y, Drucker DJ, Engleman E, Winer D, Dosch HM. Normalization of obesity-associated insulin resistance through immunotherapy. Nat Med 2009; 15: 921-929

Wooten JS, Wu H, Raya J, Perrard XD, Gaubatz J, Hoogeveen RC. The Influence of an Obesogenic Diet on Oxysterol Metabolism in C57BL/6J Mice. Cholesterol 2014: 843468

World Health Organization, 2023: Fact sheet Obesity and overweight. https://www.who.int/en/news-room/fact-sheets/detail/obesity-and-overweight (last visited 26.10.2023)

Wu J, Boström P, Sparks LM, Ye L, Choi JH, Giang AH, Khandekar M, Virtanen KA, Nuutila P, Schaart G, Huang K, Tu H, van Marken Lichtenbelt WD, Hoeks J, Enerbäck S, Schrauwen P, Spiegelman BM. Beige adipocytes are a distinct type of thermogenic fat cell in mouse and human. Cell 2012; 150: 366-376

Wu J, Cohen P, Spiegelman BM. Adaptive thermogenesis in adipocytes: is beige the new brown? Genes Dev 2013; 27: 234-250

Wu Q, Ishikawa T, Sirianni R, Tang H, McDonald JG, Yuhanna IS, Thompson B, Girard L, Mineo C, Brekken RA, Umetani M, Euhus DM, Xie Y, Shaul PW. 27-Hydroxycholesterol promotes cell-autonomous, ER-positive breast cancer growth. Cell Rep 2013; 5: 637-645

Wyss A, Raselli T, Perkins N, Ruiz F, Schmelczer G, Klinke G, Moncsek A, Roth R, Spalinger MR, Hering L, Atrott K, Lang S, Frey-Wagner I, Mertens JC, Scharl M, Sailer AW, Pabst O, Hersberger M, Pot C, Rogler G, Misselwitz B. The EBI2-oxysterol axis promotes the development of intestinal lymphoid structures and colitis. Mucosal Immunol 2019; 12: 733-745

Xu H, Barnes GT, Yang Q, Tan G, Yang D, Chou CJ, Sole J, Nichols A, Ross JS, Tartaglia LA, Chen H. Chronic inflammation in fat plays a crucial role in the development of obesity-related insulin resistance. J Clin Invest 2003; 112: 1821-1830

Yi T, Wang X, Kelly LM, An J, Xu Y, Sailer AW, Gustafsson JA, Russel DW, Cyster JG. Oxysterol gradient generation by lymphoid stromal cells guides activated B cell movement during humoral responses. Immunity 2012; 37:535-548

Zeng W, Pirzgalska RM, Pereira MM, Kubasova M, Barateiro A, Seixas E, Lu YH, Kozlova A, Voss H, Martins GG, Friedman JM, Domingos AI. Sympathetic neuro-adipose connections mediate leptin-driven lipolysis. Cell 2015; 163: 84-94

Zhao J, Chen J, Li M, Chen M, Sun C. Multifaceted Functions of CH25H and 25HC to Modulate the Lipid Metabolism, Immune Responses, and Broadly Antiviral Activities. Viruses 2020; 12: 727

Zhang Y, Proenca R, Maffei M, Barone M, Leopold L, Friedman JM. Positional cloning of the mouse obese gene and its human homologue. Nature 1994; 372: 425-432

9. Acknowledgements

First, I want to express my gratitude to Prof. Alexander Pfeifer for assigning me this interesting topic as my doctoral thesis and for the support throughout the whole project. My time in the lab was very instructive not only for my future professional career but also for my personal development.

Next, I would like to thank Dr. Francesca Copperi, my lab supervisor who taught me all practical and theoretical skills starting from pipetting and protein isolation and ending with mice preparations which I could finally carry out independently. Thank you for your time and patience that you took for explanations or for correcting my reports. However, above all, thank you for your joy and enthusiasm that you have for your work and that inspired all of us.

Moreover, I want to express my special thanks to Dr. Thorsten Gnad for providing me with some valuable advice and for correcting the manuscript. A big thank you also to Stefan Juhas und Birte Niemann who helped me with the cultivation of T17b and NIH-3T3 cells.

This thesis would not have been possible without the great work and support of our IPT colleagues. Thank you to Patricia Zehner who taught me everything about histology and to Elena Weidner who kindly repeated my UCP1 and HE stainings of the HFD experiment.

I want to thank all colleagues at the IPT and especially my office mates Martin Schwind and Katrin Rosanski for your attitude of solidarity and friendship. You were all a great support for someone like me who started to work in a completely new universe called science. Thank you for your critical discussions when I had to face obstacles, thank you for your cheerful company during our lunchbreaks or our IPT trips and thank you for all the emotions we shared.

Finally, I want to thank my family: my parents Elena and Jürgen, my sisters Anastasia and Xenia and my grandmother Erna. You supported me throughout that journey with all its ups and downs. Without you, your prayers and God’s help I wouldn’t have made it this far. Thank you!